University of New Mexico
UNM Digital Repository

Mechanical Engineering ETDs | Engineering ETDs

1-28-2015

Characterization of Mechanical Properties at the Micro/Nano Scale: Stiction Failure of MEMS, High-Frequency Michelson Interferometry and Carbon NanoFibers

Arash Kheyraddini Mousavi

Follow this and additional works at: https://digitalrepository.unm.edu/me_etds

Recommended Citation
Kheyraddini Mousavi, Arash. "Characterization of Mechanical Properties at the Micro/Nano Scale: Stiction Failure of MEMS, High-Frequency Michelson Interferometry and Carbon NanoFibers." (2015). https://digitalrepository.unm.edu/me_etds/22

This Dissertation is brought to you for free and open access by the Engineering ETDs at UNM Digital Repository. It has been accepted for inclusion in Mechanical Engineering ETDs by an authorized administrator of UNM Digital Repository. For more information, please contact disc@unm.edu.

Arash Kheyraddini Mousavi

Candidate

Mechanical Engineering

Department

This dissertation is approved, and it is acceptable in quality and form for publication: *Approved by the Dissertation Committee:*

Dr. Zayd Chal Leseman, Chair

Prof. Yu-Lin Shen, Member

Dr. Francesco Sorrentino, Member

Dr. Mani Hossein-Zadeh, Member

Characterization of Mechanical Properties at the Micro/Nano Scale: Stiction Failure of MEMS, High-Frequency Michelson Interferometry and Carbon NanoFibers

by

Arash Kheyraddini Mousavi

B.S., Mechanical Engineering, Tabriz University, 2005
M.S., Mechanical Engineering, Amirkabir University of Technology, 2008

DISSERTATION

Submitted in Partial Fulfillment of the
Requirements for the Degree of

Doctor of Philosophy
Engineering

The University of New Mexico

Albuquerque, New Mexico

November 6th, 2014

©2014, Arash Kheyraddini Mousavi

Dedication

To my parents, Behrouz and Mahin and my brother Behnam, for their endless love and support.

I would like to bring a Persian poem from Hafez here. I referred to him when thinking about attending graduate school and among tens of thousands of classical Persian poems I got the only one that has the word engineer in it, which I underlined below. During those stressful days we took that as a sign that I am in the right track and I will succeed in it.

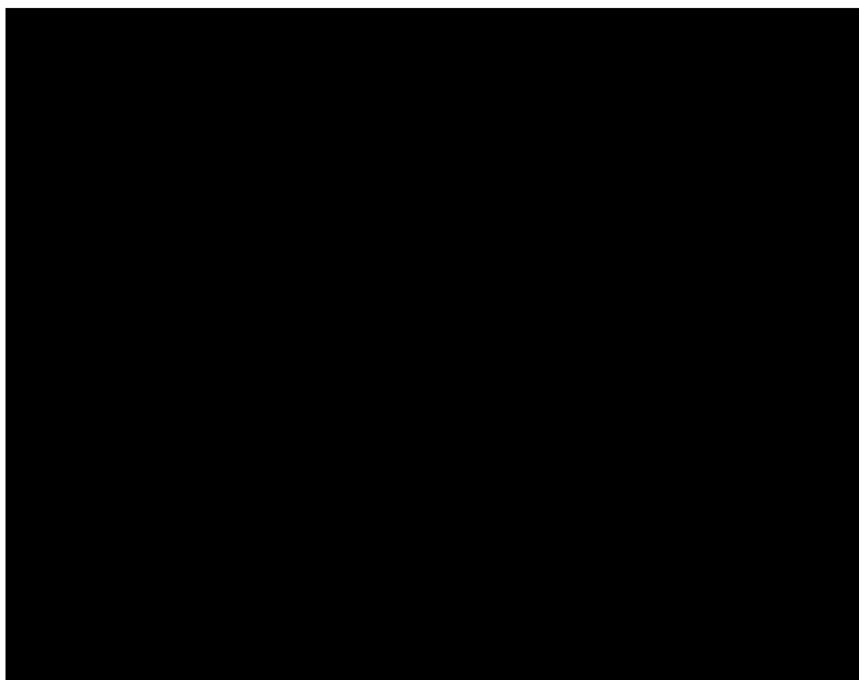

Acknowledgments

I would like to take this opportunity to first thank my advisor, Zayd Leseman, for inspiring me to work on my project and for guiding me through the last five years and half with his encouragement and support. I also thank Mani Hossein-Zadeh for his help and knowledge during the long process of making my Michelson interferometer microscope. I extend my gratitude to my other committee members, Yu-Lin Shen and Francesco Sorrentino who contributed ideas, knowledge, and support to my research. Besides my committee, many others have assisted with ideas, experiments, valuable discussions, and general encouragement and support. I thank Behnam Kheyraddini Mousavi for helping me patiently during endless nights of setting up my setup and experiments. Mohammad Jalalpour helped considerably with insightful discussions and mechanical characterization of carbon nanofiber networks. Mohammadhosein Ghasemi Baboly helped me with setting up my setup. Seyedhamidreza Alaie helped with ideas and discussions. Maheshwar Kashamolla contributed in peel test experiments and last but not least Drew Goettler helped with SEM and FIB.

Financial support that made this work possible came from a variety of sources including National Science Foundation (NSF) 1056077 (for building the interferometer for imaging phononic crystals) and 0826580 (for stiction failure of MEMS). Graduate and Professional Student Association of the University of New Mexico, Department of Mechanical Engineering Scholarships.

Characterization of Mechanical Properties at the Micro/Nano Scale: Stiction Failure of MEMS, High-Frequency Michelson Interferometry and Carbon NanoFibers

by

Arash Kheyraddini Mousavi

B.S., Mechanical Engineering, Tabriz University, 2005

M.S., Mechanical Engineering, Amirkabir University of Technology, 2008

PhD., Engineering, University of New Mexico, 2014

Abstract

Different forces scale differently with decreasing length scales. Van der Waals and surface tension are generally ignored at the macro scale, but can become dominant at the micro and nano scales. This fact, combined with the considerable compliance and large surface areas of micro and nano devices, can leads to adhesion in Micro-ElectroMechanical Systems (MEMS) and NanoElectroMechanical Systems (NEMS) - a.k.a. stiction-failure. The adhesive forces between MEMS devices leading to stiction failure are characterized in this dissertation analytically and experimentally. Specifically, the adhesion energy of poly-Si μcantilevers are determined experimentally through Mode II and mixed Mode I&II crack propagation experiments. Furthermore, the description of a high-frequency Michelson Interferometer is discussed for

imaging of crack propagation of the μcantilevers with their substrate at the nano-scale and harmonic imaging of MEMS/NEMS. Van der Waals forces are also responsible for the adhesion in nonwoven carbon nanofiber networks. Experimental and modeling results are presented for the mechanical and electrical properties of nonwoven (random entanglements) of carbon nanofibers under relatively low and high-loads, both in tensions and compression. It was also observed that the structural integrity of these networks is controlled by mechanical entanglement and flexural rigidity of individual fibers as well as Hertzian forces at the fiber/fiber interface.

Contents

List of Figures **xiv**

List of Tables **xxiv**

1 Introduction **1**

1.1 What to expect 1

1.2 Definition 2

1.3 Overview 3

1.4 Energy, Forces and Motion In MEMS 5

1.5 Comb Capacitors 9

1.6 Flexural Components in MEMS 13

1.7 Analysis of a Folded-Beam Flexure 13

1.8 Motion Quantification 16

1.9 Fabrication Methods 18

1.10 Summary 23

2 Mixed Mode I&II Crack Propagation In Poly-Si μcantilevers 26

2.1 Overview 26

2.2 Experimental Setup 29

2.3 Experimental Procedure 32

2.4 Nonlinear Beam Theory 35

2.5 Strain Energy Release Rate Formulation 40

2.6 Calculating Strain Energy and its Contributions 41

2.6.1 Results for the Strain Energy Release Rates 43

2.7 Discussion 44

2.7.1 Modeling Discussion 46

2.7.2 Experimental Discussion 48

2.7.3 Practical Considerations 49

2.8 Conclusion 51

2.9 Acknowledgments 52

3 Mode II Crack Propagation In Poly-Si μcantilevers 53

3.1 Overview 53

3.2 Experimental setup and procedure 54

3.2.1 The μcantilever beam 55

3.2.2 The MEMS force measurement unit 56

3.2.3 Independent substrate 57

3.2.4 Experimental setup assembly 57
3.3 Experimental procedure 59
3.4 Experimental results 61
3.5 Force 62
3.6 Elastic stored energy 64
3.7 Adhesion energy and Mode II critical strain energy release rate 65
3.8 Discussions 66
3.8.1 Static friction force 66
3.8.2 Surface Roughness 68
3.8.3 Critical strain energy release rate 69
3.9 Conclusions 71

4 Dynamic 3-D Microscopy Using A Michelson Interferometer 73

4.1 Introduction 73
4.2 Effect of Light Used in Interferometry 76
4.2.1 Wavelength of Light 76
4.2.2 Coherence Versus Natural Light 76
4.2.3 Polarization 78
4.2.4 Light Source Used 78
4.3 Hardware Setup 79
4.3.1 Collimation Arm 82

4.3.2 Sample Arm 83
4.3.3 Reference Arm 83
4.3.4 Camera Arm 83
4.3.5 Ghost Image Elimination 84
4.3.6 Controllers 85
4.4 Modes of operation 86
4.5 Capturing Complete Vibration Profile and Mode Shapes 88
4.6 Developed Software Packages 89
4.6.1 LabVIEW Code 90
4.6.2 MATLAB Code 91
4.7 Synchronization 94
4.8 Theory of Fringe Formation in Michelson Interferometry 94
4.9 Fringe Analysis 95
4.10 Phase Analysis Using Fourier Transforms 96
4.11 Phase Unwrapping 101
4.12 Conclusion 104

5 Synthesis & Characterization of A Nonwoven Carbon Nanofiber Structure 105

5.1 Overview 105
5.2 Introduction 106

5.3 Experimental 107

5.4 Results 108

5.5 Discussion 111

5.5.1 Processing 112

5.6 Mechanical properties 114

5.7 Electrical properties 117

5.8 Conclusions 119

6 Characterization of A Nonwoven Carbon Nanofiber Structure (Large Loads) 121

6.1 Overview 121

6.2 Keywords 122

6.3 Introduction 122

6.4 Experimental Section 124

6.4.1 Carbon Nanofiber Synthesis 124

6.4.2 Mechanical and Electrical Characterization Setups 124

6.5 Mechanical Properties 126

6.5.1 Tensile Tests 126

6.6 Compression Tests 128

6.7 Conclusions 131

References 133

List of Figures

1.1 An example of a basic MEMS that utilizes comb capacitors to generate force, a fixed-fixed flexure to guide the motion of the applied force, and a vernier to measure displacement 6

1.2 An array of capacitors are formed between each of the μcantilveres and the pad underneath them. The attractive forces generated can pull the μcantilveres slightly downwards in static mode and cause them to vibrate at dynamic mode. 10

1.3 Arrays of comb capacitors arranged symmetrically about the midline of a MEMS actuator (left). Fixed Side Closer view of a set of comb capacitors displaying the comb nature of the structure (right) 11

1.4 A single unit of a comb drive actuator 11

1.5 Electric field of a comb capacitor 12

1.6 Typical configurations for springs in MEMS actuators: (a) fixed-fixed or fixed-guided beam configuration and (b) folded-beam flexure configuration. (c) shows the flexualt system of (a) used in a MEMS. 14

1.7 Force versus displacement response for a folded-beam flexure that compares the linear and nonlinear models developed. Experimental data is given as found using the method described in [2] 15

1.8 SEM micrographs of a vernier for the measurement of displacement of a Basic MEMS Actuator 17

1.9 Schematic of a vernier for measuring the displacement of a Basic MEMS Actuator 17

1.10 Schematic of scale system, depicting a deflection of $12.0\mu m$ 18

1.11 Surface micromachining of a freestanding μcantilever: (a) deposition of a sacrificial SiO_2 layer on Si followed by photolithographic patterning, (b) removal of photo resist after etching, (c) poly-Si deposition, (d) photolithographic patterning and etching of Si to expose the sacrificial oxide layer, (e) μcantilever before release, and (f) etching the sacrificial oxide layer thus releasing the μcantilever 19

1.12 Processing steps for the SOI surface micromachining process: (a) SOI wafer anatomy, (b) photolithographic patterning of device layer, (c) deep reactive ion etching of device layer, and (d) release of device by oxide etch 21

1.13 The SCREAM process: (a) Deposition of SiO_2 on a silicon wafer followed by photolithographic patterning, (b) deep reactive ion etching (DRIE) of Si, (c) conformal deposition of SiO_2, (d) etching of SiO_2 to expose the floors adjacent to the structure to be released, (e) isotropic etching of Si to release the freestanding structure, and (f) metallization 22

1.14 Example of a Basic MEMS Actuator fabricated using the SCREAM process with comb capacitors and fixed-fixed beams. Note the scalloped floor beneath the actuators. This is indicative of isotropic Si etch in step e) in Figure 1.13 23

2.1 Experimental setup designed and fabricated to facilitate alignment and manipulation of μcantilevers and their substrate under the microscope lenes. Group B is the bottom-right stack of stages. Piezo-stage with the T-bar comprise group A.(Inset) Schematic representation of the Cantilever Beam Array (CBA) peel test experiment. The right stage is kept stationary while the left one is lifted vertically in a stepwise fashion. As the left stage is moved higher the crack length, s, continues to increase until the beam becomes completely detached from the substrate. 31

2.2 The physical layout of SUMMiT V^{TM} MEMS Technology. The five poly-Si layers are the main layers used for MEMS devices. Between each two layers of poly-Si there is a layer of oxide. The oxide layers are typically used as sacrificial layers only. 32

2.3 An example of the plots produced after analyzing the interferometry data. The beams have failed with an "s-shape" failure mode[31]. For this specific experiment the first 200μm of the beams is failed and stuck to the substrate. The plot shows the deflection of 1000μm long beams. Similar plots have been obtained for 500μm and 200μm long beams. 34

2.4 The variation of crack length(s) as a function of beam's height. . . . 35

2.5 At each increment of h, the polyslicon beams studied here can be modeled as fix-fix beams. The free body diagram of the beam includes a bending moment at each end as well as a horizontal and a vertical force. The beam is statically indeterminate. 38

2.6 Comparison between the linear and nonlinear spring models of a $500\mu m$ long hyperstatic fixed guided beam. h shows the height defence between the two ends of the beam. 39

2.7 The μcantilevers used here behave nonlinearly for crack heights bigger than $622nm$. Here the nonlinear model of the μcantilever and the experimental data for a crack height of $3.96\mu m$ are shown in the same plot. Although $3.96\mu m$ crack height falls well into nonlinear domain, the model matches the experimental data with an error less than $1.23nm$. 39

2.8 The total work done on the μcantilever can be obtained by integrating the infenitesimal work during its deformation from initial straight configuration to the final configuration. 42

2.9 The deformation of the μcantilever from its free configuration can be considered as a result of three subsequent displacements. First lifting up to the final height, h, then imposing the zero slope condition by applying the bending moment, M_0 and then making sure that the net horizontal displacement is zero by applting F_x. 43

2.10 The contributions of different external forces and moments in the total work done on a μ cantilever under large deflections are compared. The plot shows the increasing effect of longitudinal stress is the crack height(deflection) gets larger. 44

2.11 Longitudinal stresses that develop in the μcantilevers are plotted as a function of crack heights. The tensile stress develops because of the nature of the experiment which prevents any horizontal displacement of the anchor point. 44

2.12 The strain energy release rates ar calculated using a single set of data analyzed in two different ways. "$\Diamond$" and "O" represent the results of linear and nonilnear analysis respectively. The results of previous reports are also included for camparision. 45

3.1 An example of μcantilever array. The μcantilevers here are $200\mu m$ long, $2\mu m$ wide and $2\mu m$ thick. 55

3.2 Schematic representation of Mode II experimental setup. The force measurement MEMS device is shown, in red, on the left representing the rigid shuttle, four flexural arms and the vernier. The μcantilever specimen is welded on the left end of the shuttle and is stiction failed on the substrate fixed on the piezo stage on the right. 56

3.3 SEM image of a Mode II experimental device with a μcantilever beam welded to the shuttle of the MEMS Actuator. Note that the μcantilever extends beyond the edge of the image for almost another 700m. Inset: This close up shows how the μcantilever is welded to the shuttle using platinum spot welds. 58

3.4 Schematic illustration of the custom made stage and the experimental setup. The MEMS device is fixed on the piezo stage with $1nm$ accuracy in $x, y\&z$ directions. The Poly-Si substrate is fixed on the stacked set of manual stages including $x\&y$ micro positioners with $1\mu m$ and two goniometers with 8^{sec} resolution 59

3.5 As long as the stiction failed μcantilever does not slip, the deflection of the flexural arms will be equal to the total displacement of the piezo stage. Once the μcantilever starts to slip the magnitude of slip will be equal to the difference of the piezo stage displacement and deflection of the flexural springs. 61

3.6 The force-diffflection relationship of a Si fixed-fixed beam with the specifications used here, obtained using Frisch-Fay model. A third order polynomial of the form $F = k_1x + k_3x^3$ can be used to estimate this specific relationship with considerable accuracy. 62

3.7 The total longitudinal force acting on the stiction failed μcantilever as a function of the piezo stage displacement. 63

3.8 Schematic representation of the fixed-fixed spring system deflection . 65

3.9 The critical strain energy release rate values for Mode II crack propagation in poly-Si - poly-Si interface. 67

3.10 Schematic showing the various regions that are characterized 69

3.11 Schematic showing the various regions that are characterized 70

3.12 An example of two rough surfaces in contact, (a) Larger contact area brought on by capillary forces (b) An image where broken particles acting as ball bearings between the two rough surfaces (c) An image where the broken particles sit in the valley of top rough surface . . . 71

4.1 Basic light path diagram of a Michelson interferometer. 75

4.2 Comparison of two interferograms. (a) A more common quality picture obtained by interferometry [131] (b) The interferograms obtained by the fabricated microscope in this project. The image is before any enhancement. 75

4.3 Image of a μcantilever array obtained with no fringes. In order to eliminate fringes the light from reference mirror is prevented to interfer with the light from sample. 77

4.4 The finished interferometer microscope. Light generation unit is located in bottom left and is composed of laser source a temperature controller and a current controllers which feed the light into the yellow optical cable. The main body of the microscope is displayed in the center. The piezo controller in the lower left combined with the signal generation PCI board composes the actuation unit. The figure also shows the custom made stage made for proper positioning and aligning of samples. 82

4.5 Comparison of the ghost images resulted from different beam-splitters. The percentage values are with respect to the source beam intensity. (a) Schematic of a prismatic beam-splitter composed of two aligned prisms with a short distance between them. (b) Schematic of the light path in a pellicle beam splitter. (c) The resultant fringe patterns from a prismatic beam splitter shows the secondary fringes superimposed on the original horizontal fringes. The secondary fringes are the interference result of the two ghost image beams. (d) The fringe pattern obtained by a pellicle beam splitter is very smooth and free of any secondary fringes. 85

4.6 Different signals used in spectroscopy. In this example of spectrosopy camera is set to capture images at $1Hz$ and the MEMS sample is vibrating harmonically at $5Hz$. The laser illuminates the sample at the same frequency as its vibration but only for a very short time during every oscilation. This figure also shows that there is 90° phase difference between the laser and the MEMS. 88

4.7 In case of hardware limititions when it comes to continuous phase control, relative frequency difference can be used to create phase difference in consequtive frames. This figure shows how to image the full vibration mode using only 5 frames. The accruacy of this method increases as the number of frames used to cover the full vibration mode increases. The low number of frames used here is for illustration purposes only. 90

4.8 The user interface of LabVIEW code used to generate the actuation signal for the phononic crystal (MEMS Waveform Settings), Laser Source control (LED Waveform Settings) and triggering the camera (CamTrig Waveform Settings). 91

4.9 The user interface of the MATLAB code developed for image acquisition and post-processing of data. 93

4.10 A sample interferogram with considerable number of fringes. 98

4.11 Fast Fourier transform of an interferogram 99

4.12 Phase data for the interferogram of Figure 4.10 using the Fourier method. (a) shows the phase when the initial phase is considering to be equal to zero. (b) shows the phase when the initial phase is considering to be equal to π. The two phase plots belong to the same interfrogram but using different initial phases two different looking wrapped phases can be obtained. At places when part (a) reaches π or π, (b) has a value around zero and is continuous. Obtaining two phase plots for the same interferogram in this fashion makes phase unwrapping possible. 100

4.13 Unwrapped phase of Figure 4.10. 102

4.14 3-D shape of the μcantilever array of Figure 4.10. 103

5.1 Fibrous carbon foam structure viewed (a) optically (scale in inches), (b) SEM micrograph of exterior edge boxed in (a), (c) secondary electron image after FIB sectioning, and (d) magnified view of sectioned fibers in (c). 109

5.2 (a) FCF under flexing. (b) Schematic of experimental setup for measuring mechanical (dashed lines) and electrical (solid lines) properties. Cyclic compression results are shown for (c) $0.12g/cc$ and (d) $0.40g/cc$ foams. 112

5.3 Variation in (a) energy dissipation and (b) elastic moduli with cyclic loading and (c) tabulated properties of the carbon foams. 116

5.4 Plot of the resistance versus strain for the loading (a) and unloading (b) cycle 2 of the $0.12g/cc$ sample FCF (data points) and the model from Eq. (5.1) (line). The model shows qualitative agreement and demonstrates the validity of modeling the resistance change as a network of resistors. 117

5.5 Resistance (Ω) versus volume fraction of fibers (unitless) for (a) $0.12g/cc$ (initial) density sample and (b) $0.40g/cc$ (initial) density samples. Circles represent actual data points and the lines are a fit from Eq. (5.2). 119

6.1 Carbon Nanofiber Network at increasing magnification, boxes indicate section in next image (a) 1×; (b) 1000×; (c) 10,000×; (d) 20,000×. 125

6.2 Tensile behavior of carbon nanofiber network under tension, accompanied by resistance measurements as a function of strain (mm/mm). (a) Low density network; (b) High density network. 126

6.3 Five compression cycles (continuous loading and unloading) of a $0.40g/cc$ carbon nanofiber tangle sample. Data is displayed as pressure vs. percent fiber volume fraction (μ). 130

6.4 Loading portions of the curves in Figure 3 with fits to the van Wyk model. 131

List of Tables

1.1 Sensitivity of physical quantities to length scale 7

6.1 Mechanical Properties of entangled network of carbon nanofibers. . . 127

Chapter 1

Introduction

1.1 What to expect

This dissertation is focused on characterization of mechanical forces and mechanical properties of materials at micro and nano scale. It starts with an introduction to MEMS and nanotechnology, how the nature of dominant forces and their magnitude changes as size decreases, mechanisms of actuation and motion as well as fabrication methods. It then continues with detailed discussions on interferometry, stiction failure and characterization of forces leading to this permanent failure mode of MEMS, then an effort to repair stiction failed devices and concludes with a study of mechanical properties of networks of carbon nano fibers and how mechanics at nano scale effect macroscale properties. The material of Chapter 1 is published in [90].

As will be seen int this Chapter, the secondary forces prove to be highly important at micro and nano scale. These forces cause MEMS to adhere to each other, resulting in a permanent failure mode known as stiction failure.

MEMS are highly planar structures with high aspect ratios. Water can condense

in the small gaps between these planar structures as well as the tight corners formed. The large negative pressures inside the condensed liquid, deform and pull these surfaces toward each other. This negative pressure grows exponentially in size as the gaps close, literally pressing the surfaces together with an immense force. Once the surfaces are close enough the secondary forces, which also increase considerably by decreasing distances, kick in too, making sure that the surfaces will indeed stay together. Characterization of stiction failure and adhesion energy in different modes is the focus of Chapters 3 and 2. Chapter 2 is published in [86] and has also lead into multiple conference publications [56, 55, 89], talks and posters.

The work of Chapters 3 and 2 would not be possible with out the accurate and sensitive interferometer system explained in Chapter 4. This interferometer microscope is capable of measuring the 3-D shape of MEMS vibrating as fast a a couple of MHz.

The mechanical and electrical properties of nonwoven network of carbon nano fibers under small and larger forces are studied in Chapters 5 and 6 respectively. These two chapters show how nano scale mechanics control macro-scale properties of materials. Chapters 5 and 6 are published in [12, 87] respectively.

1.2 Definition

Micr-Electro-Mechanical Systems (MEMS) originally introduced in 1986 [132], are micro scale devices mainly in form of transducers, actuators or sensors. They are systems that integrate mechanical and electrical components with dimensions on the order of micrometers. Therefore, the typical motions achieved by MEMS actuators are on the order of nanometers to micrometers as well. Nanotechnology is the technology of fabrication, synthesis and characterization of devices, systems and components which at least on of their dimensions are at the order of nm. Nanotechnology

is relatively young and still considerable work is required to study nano systems and properties of materials at nano scale. The bridge between microtechnology (mainly MEMS) and nanotechnology is the nature of forces involved.

1.3 Overview

Micro and Nanotechnology are outcomes of man's desire for building very small machines. Richard Feynman in his famous 1959 lecture, There's Plenty of Room at the Bottom [39], gave this imagination of mankind an eternal life. The path to miniaturization has lead to fascinating results both in science and engineering but there is still a long way to go.

MEMS are systems that integrate mechanical and electrical components with dimensions on the order of micrometers. Though the concept of MEMS has existed since the 1960s, due to the advent of microfabrication techniques for miniaturizing electronic components, the term MEMS was not coined until 1986. Professors Jacobsen and Wood from the University of Utah devised this terminology in the course of writing a proposal to the Defense Advanced Research Projects Agency (DARPA) [132]. The term was then disseminated via a National Science Foundation (NSF) report, the Utah-held IEEE MEMS workshop in 1989, the IEEE/ASME Journal of MEMS, and subsequent DARPA MEMS funding solicitations. Since its inception, this term has gained wide acceptance as a catchall for microdevices in general.

The mechanisms by which energy is converted into motion, in MEMS, are typically physical or chemical. The produced motion can be used for positioning, opening and closing valves, switching, characterization of energy conversion processes, material characterization and studying the nature and magnitudes of dominant forces at the micro/nanoscale. A commercial application for MEMS is that of Texas Instruments Digital Micromirror Device (DMD), wherein micromirrors are positioned (ro-

tated) in order to direct light to create images in projectors for display applications. Opening and closing of (micro) valves is important for microfluidics and lab-on-a-chip applications. MEMS actuators can be configured to be energy storage devices or to detect quantities pertaining to energy conversion. Radio Frequency (RF) MEMS make use of MEMS actuators to create resonators for use in filters, reference oscillators, switches, switched capacitors, and varactors. Finally, MEMS actuators are commonly used to study material responses at the micro and nanoscales. They are used to apply mechanical forces to materials in order to characterize their material properties mechanically. Deliberate stiction failure of MEMS has been widely used to study surface forces at micro and nano scale as well as adhesion energy of Si μcantilevers [55, 56, 89, 86, 31, 71].

Fabrication of MEMS actuators typically occurs via top-down fabrication methods (such as XeF_2 dry etching systems [88]). These methods begin with a larger piece of material, typically Si, and then shape the Si into the form of a MEMS. Most MEMS actuators are extrusions of a 2-D pattern that are transferred into the Si via a photolithographic process. Three common methods by which MEMS actuators are fabricated are: Surface Micromachining[18], Silicon on Insulator (SOI) Surface Micromachining, and Single Crystal Reactive Etching and Metallization (SCREAM). Other processes exist, but many are a hybrid processes based in one of the prior mentioned processes.

Synthesis, a bottom-up method is more common than top-down methods for nanostructures and nano-systems. In this method nano structures are synthesized from simpler chemical components through highly controlled chemical reactions. The initial precursors in this methods can be in gaseous, dissolved in a liquid or nano power form. Also catalysts in the form of nano powders are commonly used as seeds to grow nanotubes, nano-fibers[12, 87] and nano-rods[54, 115].

This discussion of Basic MEMS Actuators will be broken into four parts. First,

there will be a description of energy conversion mechanisms that generate forces; a specific discussion follows on comb capacitors and how they convert (electrical) energy into a force. Second, a discussion will ensue on how MEMS actuators convert the force into motion via a compliant structure. Third, methods for quantification of the motion will be discussed with specific emphasis on an integrated method for measurement of displacements. Finally, a brief description of the three main processes for fabrication of MEMS actuators will be given.

The MEMS depicted in Figure 1.1 shows the main components present in most MEMS. It uses arrays of capacitors also known as comb-drives to generate the force required to generate motion. The moving parts of the device are suspended using two sets of fixed-fixed beam flexures on top and on the bottom. These flexural elements are also used to return the device to its initial configuration. Displacements of this actuator are measured using a vernier. All components mentioned will be discussed in detail here.

1.4 Energy, Forces and Motion In MEMS

MEMS convert different forms of energy into force and motion and vise versa. For example, two electrically isolated parallel plates with an applied potential difference will develop an electrostatic force between the plates. If those plates are on flexible springs then they will move toward one another. This type of energy conversion into motion is termed electrostatic actuation. Other types of actuators also use electrostatic actuation such as the nanotractor or inchworm actuator [33], scratch drive actuators [5], and the shuffle motor [109]. Beyond electrostatic actuators, many other actuators have been developed that use fluidic forces [112], magnetic forces [21], radiation pressure [119], piezoelectrics [59], shape-memory alloys [43], and thermal expansion [98].

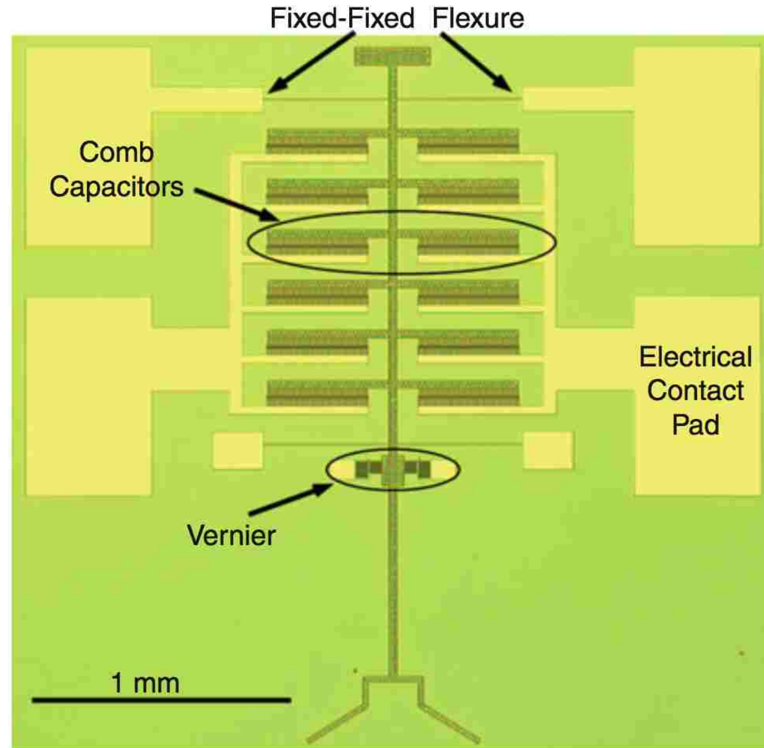

Figure 1.1: An example of a basic MEMS that utilizes comb capacitors to generate force, a fixed-fixed flexure to guide the motion of the applied force, and a vernier to measure displacement

Of particular importance for MEMS is the way with which these forces scale with length; they scale differently due to the different physics involved. Table 1.1 displays a list of common forces and quantities that are of interest for MEMS actuators and gives how they scale with length.

Table 1.1 displays the way with which each force scales with length. Variables containing a geometric length pertinent to the physical system are in parentheses and moved to the right-hand-side of the equation. It is these quantities that are used to determine a quantities sensitivity to length scale. Note each entry in Table 1.1 is highly dependent on the configuration of the system. In addition to common forces generated in MEMS actuators, this table also includes gravity, van der Waals forces,

inertia, and the mass moment of inertia for reference.

Interpretation of Table 1.1 is accomplished by comparing the exponents of the fourth column. These exponents are used to compare the importance of a given energy conversion process at different length scales. l^0 indicates that the force generating mechanism is invariant with length scale. l raised to a positive power means that the property grows with increasing scale, while a negative power implies that the property grows with decreasing scale.

As seen in Table 1.1, different forces scale differently with size (also referred to as size effect). The most important forces at macro scale such as inertia and weight (l^3), drag forces (l^2) and magnetic forces ($l^2 - l^4$) are ignorable at micro and nano scale while other forces such as van der Waals (l^{-1}), viscus forces ($l^{-1} - l^1$), electrostatic forces (l^0) and surface tension forces (l^1), which are often ignored at macro scale, either increase, stay the same or decrease slightly as the size decreases. This makes the nature of forces that one needs to consider when dealing with MEMS and nano-devices very different that what we are used to. It worth mentioning that most of these forces are nonlinear in nature which makes design, fabrication and characterization of MEMS and nano-systems more challenging. Stiction failure of MEMS (see Chapters 2 and 3) and NEMS to each other and nearby surfaces, due to condensation and surface forces, is an example of the issues caused by these forces. Carbon nano fibers agglomerate and are not easily dispersible due to secondary forces keeping them together. An interesting example of now the forces of nano world can effect macro scale properties is the nonlinear mechanical behavior of entangled networks of carbon nano fibers (see Chapters 5, and 6).

Different scaling of forces with size can be a good news when it comes to actuation however. Energy conversion mechanisms with negative exponents will behave more favorably at smaller length scales. Of the mechanisms listed, the easiest to employ and control are thermal (l^2) and the electrostatic force generated by comb capacitors

Table 1.1: Sensitivity of physical quantities to length scale

Physical quantities	Examples	Governing equation	Sensitivity to length scale
van der Waals $\breve{A}$:= *Hamaker constant* A := *Area* d := *Distance between objects* r := *Radius* r_i := *Radius of object "i"* l = *Facing lengths of two objects*	*Case 1:* Two spheres	$F=\frac{\breve{A}}{6}\left(\frac{r_1r_2}{r_1+r_2}\frac{1}{d^2}\right)$	l^{-1}
	Case 2: A sphere and a surface	$F=\frac{A}{6}\left(\frac{r}{d^2}\right)$	l^{-1}
	Case 3: Two cylinders	$F=-\frac{A}{8\sqrt{2}}\left(\sqrt{\frac{r_1r_2}{r_1+r_2}}\frac{l}{\sqrt{d^5}}\right)$	l^{-1}
	Case 4: Two crossed cylinders	$F=\frac{A}{6}\left(\frac{\sqrt{r_1r_2}}{d^2}\right)$	l^{-1}
	Case 5: Two Surfaces	$F=\frac{A}{6\pi}\left(\frac{1}{d^3}\right)$	l^{-3}
Viscous forces μ := *Dynamic viscosity* V_0 := *Relative velocity*	*Case 1:* Two infinite plates	$F=\mu V_0\left(\frac{1}{d}\right)$	l^{-1}
	Case 2: Two finite plates	$F=\mu V_0\left(\frac{A}{d}\right)$	l^{1}
Electrostatic force $\in_r$:= *Relative static permittivity* $\in_0$:= *Vacuum permittivity* V_e := *Electrical potential* h := *out of plane thickness*	*Case 1:* Finite parallel plates at distance d	$F=\frac{\in_0\in_r V_e^2}{2}\left(\frac{A}{d^2}\right)$	l^{0}
	Case 2: Comb drive	$F=\frac{\in_0\in_r V_e^2}{2}\left(\frac{h}{d}\right)$	l^{0}
Thermal expansion E_y := *Young modulus of elasticity* α_T := *Therma expansion coefficient* ΔT := *Temperature change*	*Case 1:* Constrained column	$F=E_y\alpha_T\Delta TA$	l^{2}
Magnetic forces μ_0 := *Vacuum permeability* d := *Distance between wires* l := *Length along wire* I_i := *Current in wire "i"* A_0 := *Cross sectional area* A_S := *Surface area* $\dot{Q}_S$:= *Surface heat flow rate* I_e := *Electrical current*	*Case 1:* Constant current density with the boundary condition $\frac{I_e}{A_0}$ = cons.	$F=\frac{\mu_0}{2\pi}\frac{l}{d}I_1I_2$	l^{4}
	Case 2: Constant heat flow through the surface of the wire with the boundary condition $\frac{\dot{Q}_S}{A_S}$ = cons.	$F=\frac{\mu_0}{2\pi}\frac{l}{d}I_1I_2$	l^{3}
	Case 3: Constant temperature rise of wire with the boundary condition ΔT = cons.	$F=\frac{\mu_0}{2\pi}\frac{l}{d}I_1I_2$	l^{2}
Piezoelectric force $\in$:= *Mechanical strain* E_e := *Electrical field* e_p := *Piezoelectric constant* $\frac{\text{Charge density}}{\text{Applied strain}}$ E_y^E :=*Young modulus at constant* E_e	*Case 1:* 1-D unconstrained actuation	$F=-e_pV_e\left(\frac{A_0}{d}\right)+E_y^E\in(A_0)$	l^0&l^2
Drag force ρ := *Density* C_d := *Drag coefficient* A_p := *Projected are normal to flow*	*Case 1:* Infinite cylinder (C_d = .47) *Case 2:* Flat plate perpendicular to flow (C_d = 1.28)	$F=\frac{1}{2}\rho V_0^2C_d(A_p)$	l^{2}
Surface tension force γ := *Surface tension* p := *Perimeter*		$F=\gamma(p)$	l^{1}
Inertia and weight g := *Gravity* α := *Acceleration* $\forall$:= Volume	*Case 1:* Weight	$F=\rho g(\forall)$	l^{3}
	Case 2: Inertia force	$F=\rho a(\forall)$	l^{3}
Mass moment of inertia ρ_l := *Mass per unit length* ρ_A := *Mass per unit area* ρ_V := *Mass per unit volume* r := *Radius*	*Case 1:* Sphere	$\bar{I}=\frac{8\pi}{15}\rho_V(r^5)$	l^{5}
	Case 2: Thin circular disk	$\bar{I}=\frac{\pi}{2}\rho_A(r^4)$	l^{4}
	Case 3: Slender bar	$\bar{I}=\frac{1}{12}\rho_l(l^3)$	l^{3}

(l^0). Comb versus parallel plate capacitors are explained in more detail in Sec 1.5.

When compared to how inertia scales (l^3), both thermal and electrostatic actuation schemes behave more favorably at smaller length scales. The mass moment of inertia is also displayed in Table 1.1. The exponent of five (sphere) implies that it diminishes at shorter length scales more rapidly than any of the other forces. Because inertial force and mass moment of inertia are relatively small, compared to common forces used in MEMS actuators, their dynamic responses are much faster than their macroscopic counterparts.

Electrostatic and thermal actuators scale favorably with decreasing length scales and are more easily implemented than most other methods. This makes them considerably more popular than other energy conversion methods. Capacitive actuation pads designed under μcantilevers can be used to induce mechanical vibrations required for studying dynamic behavior of stiction failed MEMS. The following section focuses on electro static force generation in MEM, specially capacitance due to comb capacitors.

1.5 Comb Capacitors

In order to generate the force applied to the MEMS actuator, one of the more common methods is to use capacitors. The common methods are parallel plate capacitors and comb capacitors. A parallel plate capacitor has a capacitance equal to:

$$C_{pp} = \frac{\epsilon_0 A}{d} \tag{1.1}$$

where ϵ_0 is the permittivity of the material between the plates (usually air or vacuum), A is the area of parallel plate capacitor, and d is the gap between the parallel plates. The electrostatic energy is $\frac{1}{2}C_{pp}V^2$, where V is the voltage between the parallel plate capacitors. Taking its derivative with respective to the gap, the force is

calculated to be

$$F_{pp} = \frac{\epsilon_0 A V^2}{2d^2} \tag{1.2}$$

Note that F_{pp} is always attractive and is nonlinear in not only the voltage, but also in the gap between the parallel plates. Figure 1.2 shows the capacitors formed between an array of μcantilevers and a Si pad underneath them.

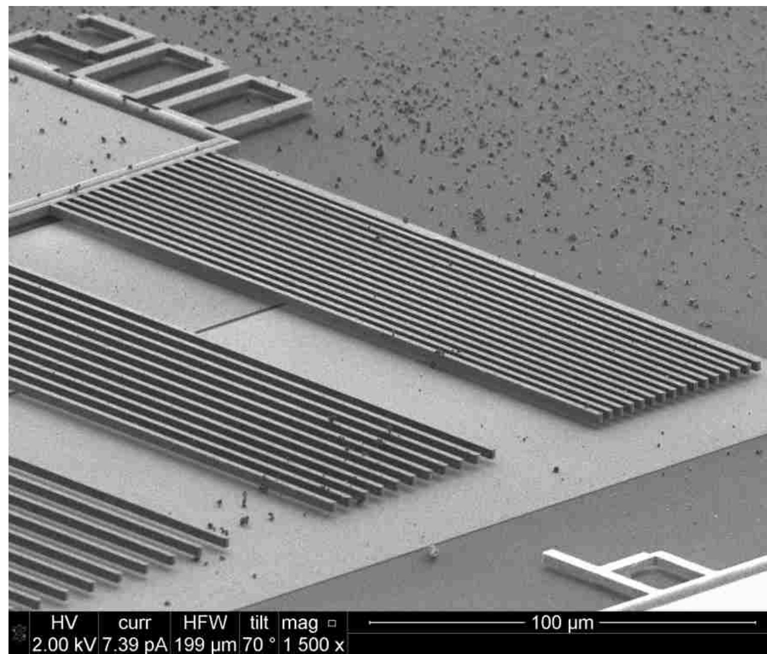

Figure 1.2: An array of capacitors are formed between each of the μcantilveres and the pad underneath them. The attractive forces generated can pull the μcantilveres slightly downwards in static mode and cause them to vibrate at dynamic mode.

The geometric nonlinearity of (1.2) makes control of capacitive actuators difficult and led to the development of comb capacitors [121]. SEM images of a comb drive array are shown in Figure 1.3. Comb capacitors are arrays of interdigitated fingers. One side of the array is rigidly attached to the substrate while the other is allowed to move via a flexure structure which will be discussed in the next section.

Comb capacitor drives typically have hundreds to thousands of combs to generate

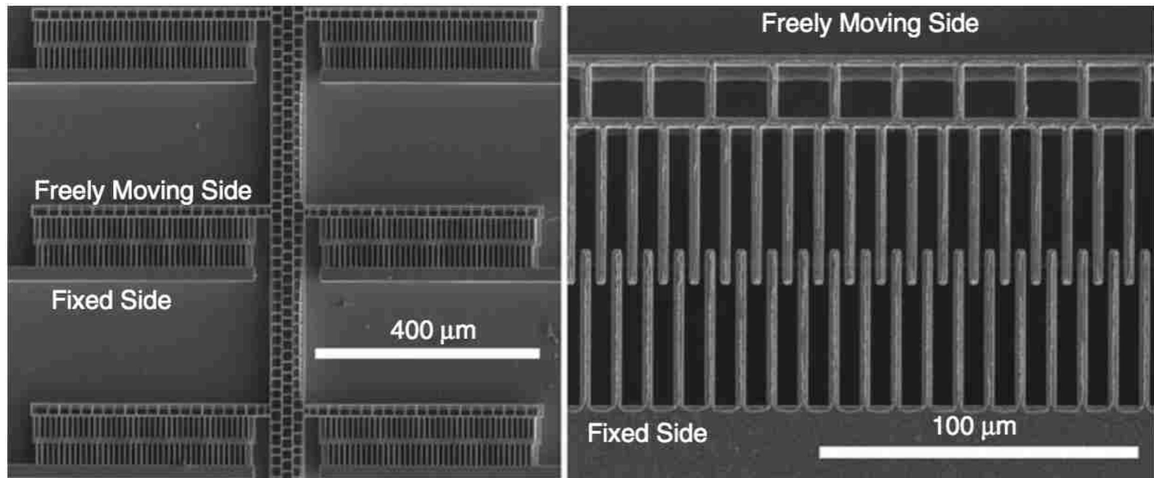

Figure 1.3: Arrays of comb capacitors arranged symmetrically about the midline of a MEMS actuator (left). Fixed Side Closer view of a set of comb capacitors displaying the comb nature of the structure (right)

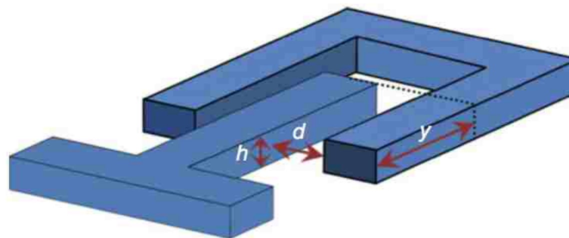

Figure 1.4: A single unit of a comb drive actuator

a desired force. For analysis purposes, Figure 1.4 shows one unit of a comb drive. When connected to an external source, opposite charges gather on the surfaces of the comb fingers which generate an electric field; see Figure 1.5. Note that along the vertical line of symmetry of Figure 1.5 that the horizontal components to the right and left are equal and opposite. Thus the net force due to the horizontal components is zero. The vertical components of the fringing field at the tip of the comb finger, however, are not balanced and a net attractive force results. The capacitance of an

array of comb capacitors is found to be:

$$C_{cc} = 2n\frac{\epsilon_0 hy}{d} \tag{1.3}$$

where n is the number of combs in the array, h is the depth of the comb, y is the overlap between the moving and fixed comb, and d is the gap between the moving and fixed comb. The attractive force generated by the comb capacitors when a voltage is applied is:

$$F_{cc} = \frac{n\epsilon_0 h}{d}V^2 \tag{1.4}$$

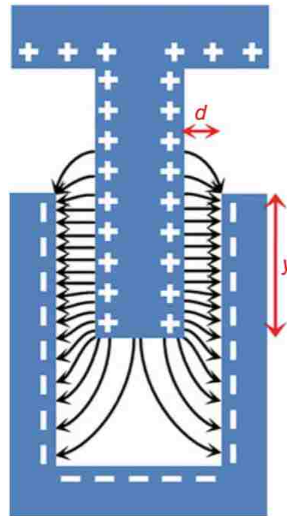

Figure 1.5: Electric field of a comb capacitor

The parameters in (1.4) are constant with the exception of the voltage. This type of relationship is more desirable than the relationship in (1.2), especially for dynamic excitation. Equations (1.3) and (1.4) are valid when the initial engagement of the comb is $> 4d$ until the tip of the moving comb is within a distance $4d$ of the fixed side of the comb drive.

1.6 Flexural Components in MEMS

The force created by the conversion of energy is transmitted to a compliant structure (spring) via a stiff structure that traditionally comprises a majority of the mass the proof mass. Though many different configurations have been used for the compliant structure, the two most common structures used are shown in Figure 1.6. Figure 1.6a is a fixed-fixed (clamped-clamped) beam configuration while Figure 1.6b is referred to as the folded-beam flexure. Figure 1.6c shows an SEM of the first configuration being used in a MEMS device. Note that Figure 1.6a is also referred to as a fixed-guided configuration. 'F' in each of the figures represents the applied force onto the structure by a means of energy conversion, as was described in the previous section.

One-dimensional motion is often desired. Therefore, one direction is designed to be considerably more compliant than the two orthogonal directions. This typically leads to beams that have slenderness ratios greater than 100 (see Figure 1.6c). Additionally, structures must be designed such that the guided motion is parallel to the force. This requires a configuration that is symmetric about the axis of motion. Thus only even numbers of beams can be connected to the proof mass. An additional concern is that asymmetric loading may cause the structure to rotate if there are only two connections. Therefore, many designs will have four or more connections at the extremities of the actuator to avoid rotations. The force/deflection behavior of folded-flexure configuration is studied in Section 1.7. A through study of mechanical response of fixed-fixed configuration is postponed to Chapters 3 and 2.

1.7 Analysis of a Folded-Beam Flexure

The folded-beam flexure, Figure 1.6b, is a variation of the fixed-guided beam configuration. Because the beams are folded, this structure experiences less axial stretch

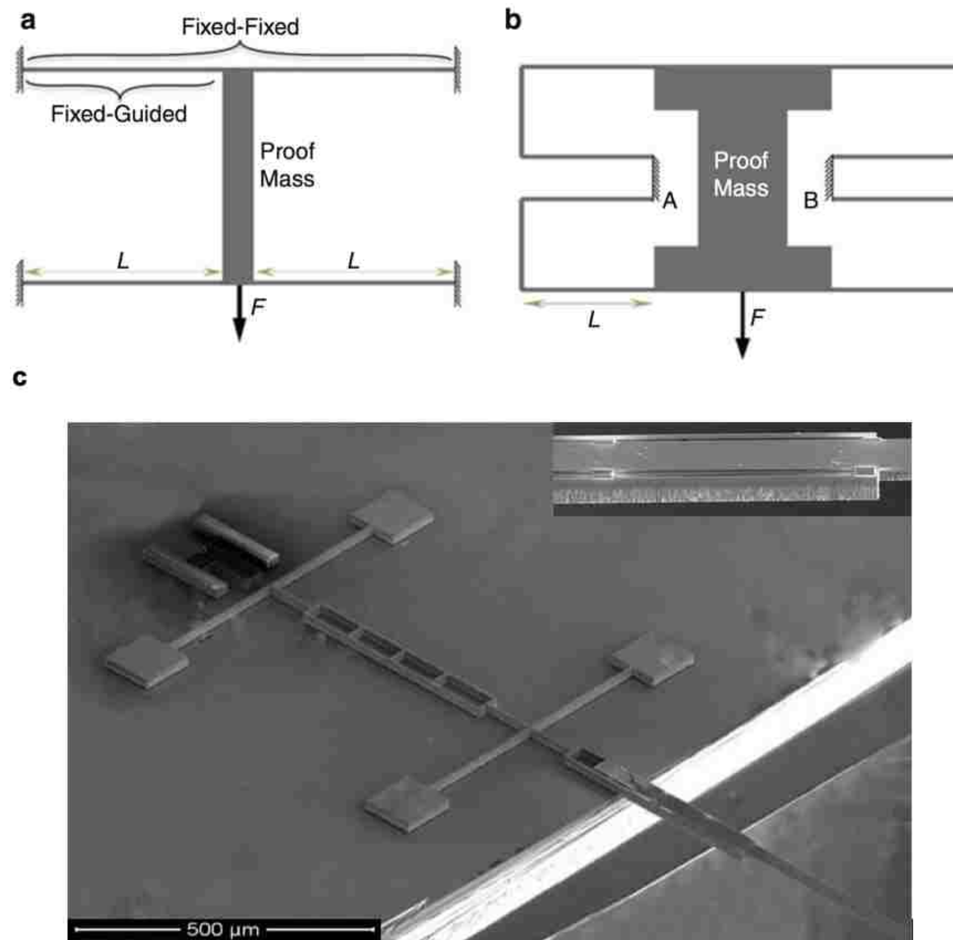

Figure 1.6: Typical configurations for springs in MEMS actuators: (a) fixed-fixed or fixed-guided beam configuration and (b) folded-beam flexure configuration. (c) shows the flexualt system of (a) used in a MEMS.

than the fixed-guided structure of Figure 1.6a. Because there is less axial stretching in the folded-beam flexure, the linear range is much larger for folded-beam flexures than for fixed-guided beam flexures. In order to find the solution for folded-beam flexure as in Figure 1.6b, springs constants are added in series and parallel, as appropriate. For example, for the structure shown in Figure 1.6b the spring constant would be $24EI/L^3$.

For even larger deflections, elastica theory must be applied. Along the y-direction,

the displacement and force are [65]:

$$\frac{L}{2}\sqrt{\frac{F_y}{EI}} = \int_{\phi_1}^{\frac{\pi}{2}} \frac{d\phi}{\sqrt{1 - p^2 \sin^2 \phi}} \tag{1.5}$$

$$\delta = \frac{EI}{F_y} \int_{\phi_1}^{\frac{\pi}{2}} \frac{2p^2 \sin^2 \phi - 1}{\sqrt{1 - p^2 \sin^2 \phi}} d\phi \tag{1.6}$$

where:

$$\phi_1 = \sin^{-1}\left(\frac{1}{\sqrt{2p^2}}\right) \tag{1.7}$$

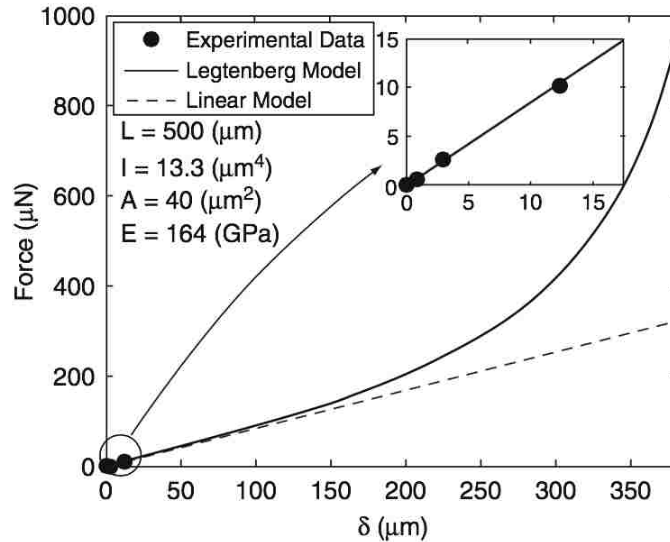

Figure 1.7: Force versus displacement response for a folded-beam flexure that compares the linear and nonlinear models developed. Experimental data is given as found using the method described in [2]

Figure 1.7 plots both the linear and nonlinear solution for the device shown in Figure 1.6c. In addition to the derived solutions experimental data is included on the plot. Data is taken by hanging calibrated weights from the device as is detailed in [2]. The width of the folded-beam flexures beams is $2\mu m$. Note that the nonlinear model diverges at almost 55 times the beams thickness!

1.8 Motion Quantification

Many different schemes have been proposed for the quantification of the displacement of the MEMS actuators. The most common types include measuring capacitance, resistance, or interpreting an optical signal. Capacitance measurements are especially common when the method of actuation is by capacitors as well. By utilizing a high frequency voltage on the capacitors, one can measure the impedance. Equation (1.1) is for the capacitance due to parallel plate capacitors and (1.3) is for comb capacitors. Both equations contain a term that relates the displacement to the capacitance of the MEMS actuator. Piezoresistance is also a common method because of the ease of measurement. Limitations of either capacitance or piezoresistance measurements include the sensitivity of the instrument and the ability to isolate the actuator from noise. Optical measurements can be broken into two main categories, interferometric and vernier. Interferometry can make very sensitive measurements of displacement and (depending on the technique) may be limited only by thermal vibrations. This method is discussed in details in Chapter 4. A vernier is a simple method and can be co-fabricated into the device; see Figure 1.8.

In order to measure the displacements of the springs, two sets of scales are incorporated in the design of the MEMS actuator. These are a fixed main scale that is attached to the substrate, and a moving vernier scale that is integrated into the MEMS actuator, Figure 1.8 and Figure 1.9.

The vernier is an auxiliary scale, whose graduations are of different spacing from those of the main scale, but that bear a simple relation to them. The vernier scale of Figure 1.9 has ten divisions that correspond in length to nine divisions on the main scale. Each vernier division is therefore shorter than a main-scale division by 1/10 of a main-scale division. Main-scale divisions are $5\mu m$ apart. The Least Count (LC), which is defined as the smallest value that can be read on the vernier scale, is

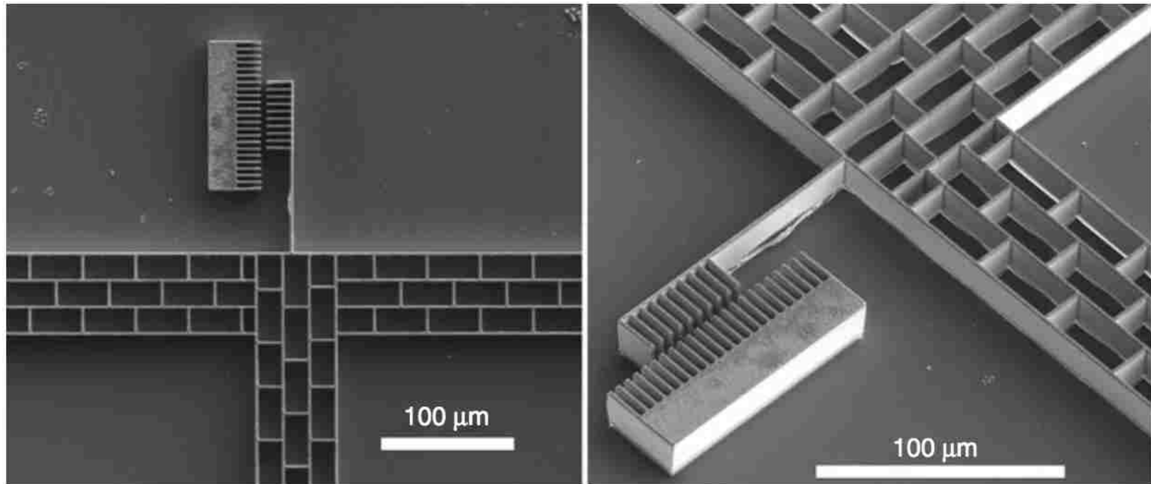

Figure 1.8: SEM micrographs of a vernier for the measurement of displacement of a Basic MEMS Actuator

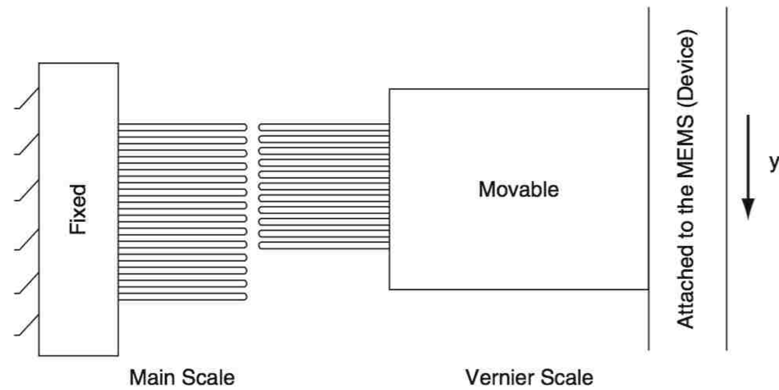

Figure 1.9: Schematic of a vernier for measuring the displacement of a Basic MEMS Actuator

therefore:

$$LC = 5 \times \frac{1}{10} = 0.5\mu m \tag{1.8}$$

For example, in Figure 1.10, the zero of the vernier scale is moved past two complete divisions of the main scale, and the fifth scale is aligned perfectly to the same fifth main-scale reading.

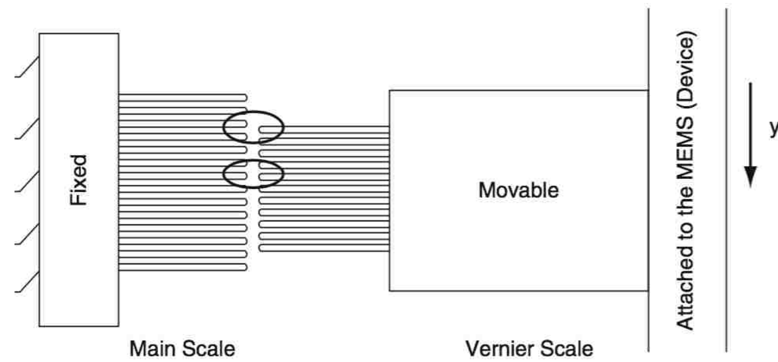

Figure 1.10: Schematic of scale system, depicting a deflection of $12.0\mu m$

Therefore reading from the above setting the would be:

Main scale divisions = 2

Main scale spacing = $5\mu m$

Total main scale reading $= 2 \times 5\mu m = 10\mu m$

Vernier scale division that coincides with main scale = 4

Least count of the vernier scale $=0.5\mu m$

Total vernier scale reading $= 4 \times 0.5\mu m = 2.0\mu m$

Total = main scale reading + vernier scale reading

Total $= 10 + 2.0\mu m = 12.0\mu m$

1.9 Fabrication Methods

As mentioned previously, there are three main methods for fabrication of MEMS actuators: Surface Micromachining, SOI, and SCREAM [77]. It is important to emphasize that many other processes exist and new processes are being developed

constantly. Modifications are typically introduced to accommodate for the actuators ultimate application or for the type of energy conversion method that the actuator will be utilizing.

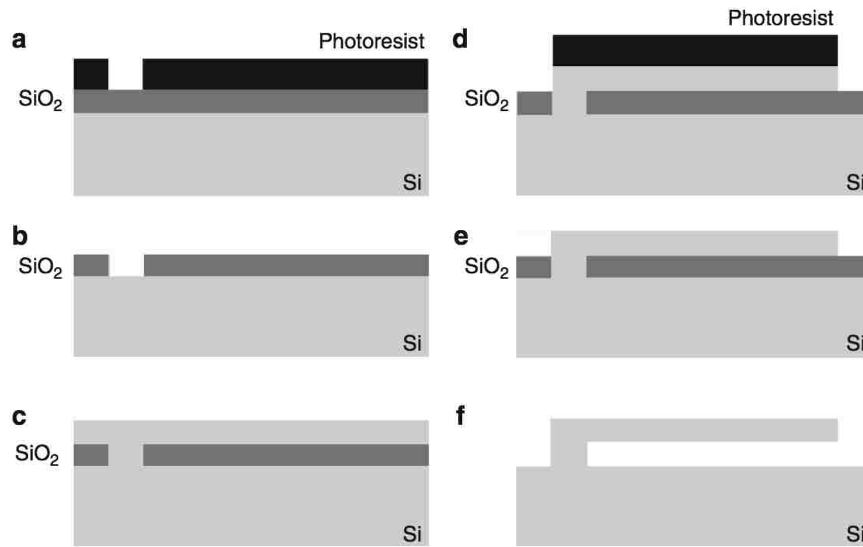

Figure 1.11: Surface micromachining of a freestanding μcantilever: (a) deposition of a sacrificial SiO_2 layer on Si followed by photolithographic patterning, (b) removal of photo resist after etching, (c) poly-Si deposition, (d) photolithographic patterning and etching of Si to expose the sacrificial oxide layer, (e) μcantilever before release, and (f) etching the sacrificial oxide layer thus releasing the μcantilever

Surface micromachining is a process built by alternating the deposition and patterning of sacrificial layers and structural layers of material. Typically, the sacrificial layers are a type of silicate glass (Phospho-Silicate-Glass (PSG) or SiO_2). This layer is commonly referred to as the sacrificial oxide (sac-ox). The structural layers are often made of polycrystalline Si (poly-Si). After the deposition of each layer, that layer is patterned using a photolithographic process to define either holes through the sacrificial layer or physical features of the device in the case of a structural layer.

Figure 1.11 details a simple surface micromachining process for a cantilever beam. Each step (a-f) is a cross-sectional view for the structure. This is a common method

of representing a microfabricated structures process flow. This method typically revolves around an important feature of the final structure. Note that due to the nature of this process, numerous alternating layers of sac-ox and structural layers can be built up to form devices with multiple layers of functionality. One of the more common processes used for surface-micromachined MEMS is the SUMMiT process [116]. At the writing of this entry, the current process is entitled SUMMiT^{TM} V, where 'V' stand for five structural layers of poly-Si. An example of a SUMMiT surface-micromachined device is shown in Figure 1.2.

SOI surface-micromachined devices are similar to the surface micromachining process previously described except that the process begins with an SOI wafer. SOI wafers are comprised of three layers: a handle layer, a buried oxide layer (BOX), and a device layer. The handle layer acts as a substrate for the BOX and device layer. BOX layers are the sacrificial layer to be removed by an oxide etch at the end of the process, whereas the device layer is the structural layer of Si for the actual MEMS. The device layer is a piece of single crystal Si, not poly-Si as in standard surface micromachining. Due to the nature of the SOI wafer, SOI surface micromachining is used to make single structural layer devices. The general process flow for an SOI surface-micromachined process is shown in Figure 1.12. The freestanding beam in the Figure 1.12d would be for any part of a MEMS actuator that is capable of movement. These freestanding beams however must be anchored to the substrate. This accomplished by having structures with larger cross sections that are not fully undercut by the HF etching process. The left and right side of the device layer in Figure 1.12d are a partial view of cross section where the SiO_2 has not been fully undercut, thereby allowing for a physical connection between the device layer and handle layer. Note that the connections of the device to ground can be isolated electrically from one another. This is an important feature for placing biases on comb structures such as the one shown in Figure 1.6. Although SOI surface micromachining and standard surface micromachining are similar, the device layer in the SOI process

can have a broader range of thickness varying from $100's$ of nm to several $10's$ of μm. This is important because (1) layer thickness increases the actuator force and (2) a thick layer can make the out-of-plane stiffness of folded-beam suspension much greater, thereby minimizing unintended displacements.

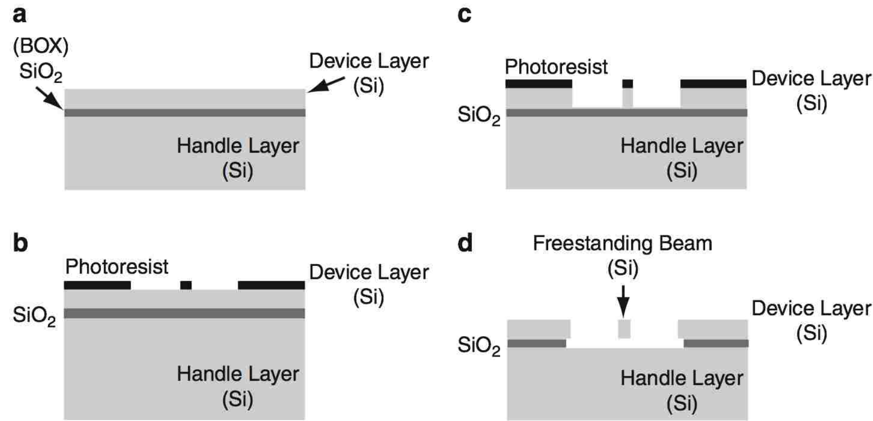

Figure 1.12: Processing steps for the SOI surface micromachining process: (a) SOI wafer anatomy, (b) photolithographic patterning of device layer, (c) deep reactive ion etching of device layer, and (d) release of device by oxide etch

The SCREAM process is a bulk processing method that utilizes a bulk piece of single crystal Si a Si wafer. Typically, this process utilizes one mask (one photolithography step) as does SOI surface micromachining. In order to create freestanding structures, SCREAM utilizes the selectivity of etchants to certain deposited films and isotropic versus anisotropic etching.

Figure 1.13 demonstrates the SCREAM process [114]. A Si wafer is the base substrate. SiO_2 is deposited on the surface of the Si. Photoresist is then patterned to define the 2D layout of the microactuator (Figure 1.13a).

Narrow features, approximately $1\mu m$, will be released (freed), while wider structures, approximately $100\mu m$ or larger, will remain fixed to the substrate during the release process. After patterning, the Si is etched anisotropically (vertically) typically via a deep reactive ion etch (DRIE) (Figure 1.13b). The photoresist is then

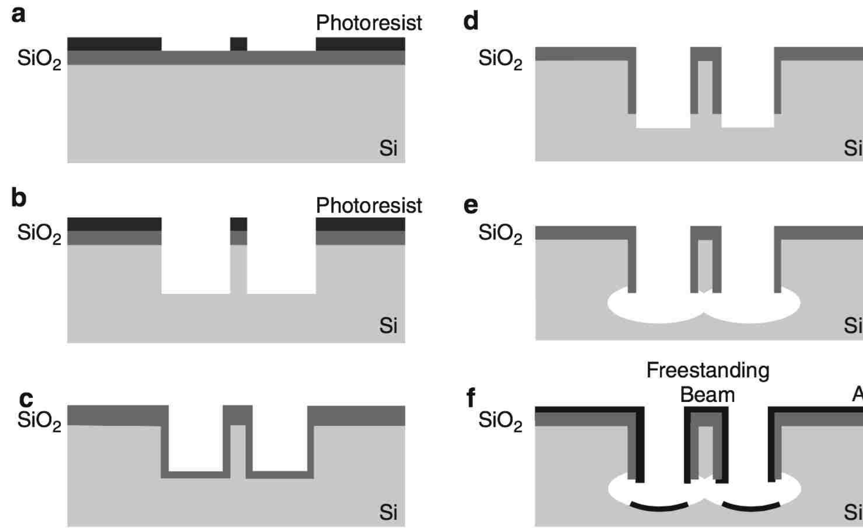

Figure 1.13: The SCREAM process: (a) Deposition of SiO_2 on a silicon wafer followed by photolithographic patterning, (b) deep reactive ion etching (DRIE) of Si, (c) conformal deposition of SiO_2, (d) etching of SiO_2 to expose the floors adjacent to the structure to be released, (e) isotropic etching of Si to release the freestanding structure, and (f) metallization

removed and a conformal layer of SiO_2 is deposited (Figure 1.13c). This step is important to the process in that it places an electrical insulator on the sidewalls of the structures. The SiO_2 on the floor of the wafer is then back etched to expose the Si. A subsequent Si etch then isotropically removes Si from the floor (Figure 1.13d). This etch is allowed to continue to the point where the two etch fronts from either side of the narrower structures are allowed to merge, thereby releasing the narrow structures (Figure 1.13e). The wider adjacent structures are also undercut, but not released. In the final step, a metal is deposited (Figure 1.13f). Metal is allowed to coat the top horizontal surface and vertical surfaces of the device. Depending on the layout of the device, the islands on the left and right of the freestanding beam can be electrically isolated from the beam and from one another, connect to one or the other, or connect to both. The isotropic etch of Si in step e) allowed for the SiO_2 layer to shield the metal (Al) from coming into contact with the Si. If the

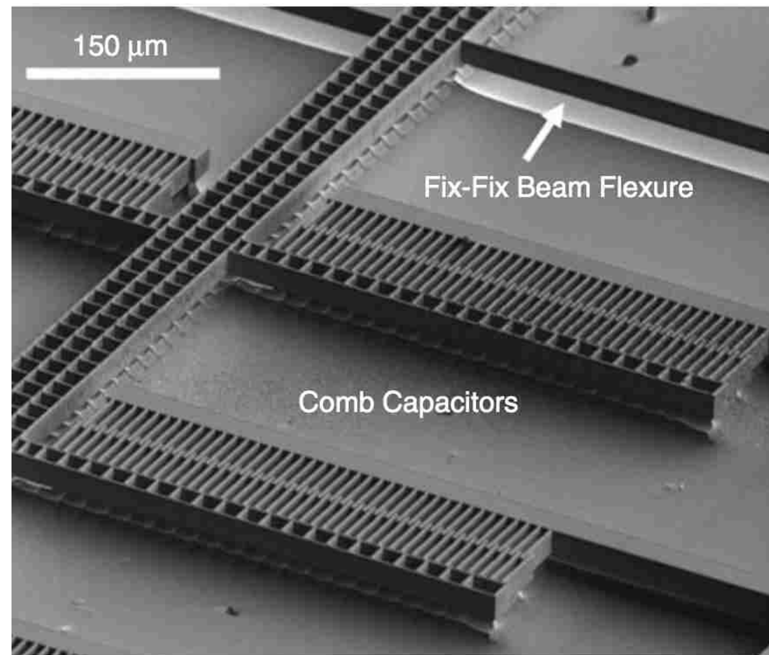

Figure 1.14: Example of a Basic MEMS Actuator fabricated using the SCREAM process with comb capacitors and fixed-fixed beams. Note the scalloped floor beneath the actuators. This is indicative of isotropic Si etch in step e) in Figure 1.13

metal of each structure had touched the Si then the entire device would be shorted and no potential could be set up for actuation of the device. Figure 1.14 is an SEM micrograph of a MEMS actuator fabricated with the SCREAM process.

1.10 Summary

This chapter covered the basics of MEMS and their actuation and fabrication mechanicsm. The discussion was broken into four parts covering: energy conversion mechanisms for generation of force, compliant structures, motion quantification, and fabrication techniques. The section covering energy conversion mechanisms discussed the common mechanisms used in MEMS actuators and went into detail on elec-

trostatic actuation. In particular, the salient features of parallel plate and comb capacitors were presented. Converted forces are used to move MEMS to perform a host of applications. This motion occurs in controlled manner via a compliant structure. Two of the more common compliant structures used for MEMS actuators are fixed-guided beams and the folded flexure structure. Both the linear and nonlinear force versus displacement relationships are given for both of these common structures. Motion of the actuator is quantified in many different ways. Use of a simple co-fabricated vernier is detailed in this entry. Finally, the three main processes for fabrication of MEMS actuators were detailed. These included: Surface Micromachining, SOI, and the SCREAM processes.

In the next chapter the adhesion of MEMS μcantilevers to a poly-Si (also knowns as stiction failure) and peel test experiments will be used to study the crack propagation in the interface between the μ cantilever and the substrate and determine the critical strain energy release rate. The peel tests are commonly knows as mode I crack propagation experiments but as will be seen in Chapter 2 there is a substantial contribution of Mode II crack propagation. This is noticed due to the considerable longitudinal stresses developed inside the μcantilevers. The considerable contribution of Mode II crack propagation determined us to study a pure mode II crack propagation to determine the mechanisms and magnitude of this mode. The results for mode II crack propagation are presented in Chapter 3. The experiments of Chapters 2 and 2 would not be possible with out an accurate Interferometer Michelson interferometer to determine the out of plane deformation of the μcantilever samples with high accuracy. A brief discussion on the Michelson Interferometer built as a part of this work is provided in Chapter 4.

Chapters 5 and 6 are devoted to study of mechanical properties at nano scale and how they effect the macro scale properties. The mechanical as well as electrical properties of samples made from entangled networks of carbon nano fibers are studied

under relatively small (Chapter 5) and large forces (Chapter 6) both in tension and under compression. It was also shown that a relatively old relationship proposed by Van Wyk [125], in 1946 can accurately predict the force displacement behavior of a modern material.

Chapter 2

Mixed Mode I&II Crack Propagation In Poly-Si μcantilevers

2.1 Overview

Stiction failure continues to be a hinderance to the viability of micro and nanodevices where moving parts and impacting/sliding surfaces are necessary for functionality [107]. This mode of failure occurs when two independent surfaces adhere to one another and the device's operation is compromised. As such, many researchers continue to develop methods to lower the surface energy of the devices and their neighboring surfaces, in order to avoid stiction failure. Other researchers engineer methods to repair stiction failed MEMS and NEMS. Common to either case is the necessity for measurement of the critical strain energy release rate (or adhesion energy) in order to properly engineer the surfaces or the method of repair.

Stiction failure typically occurs as a result of processing or during use. Accord-

ingly, researchers have attacked the problem of inhibiting stiction failure from those two perspectives. The most common method for avoiding stiction failure due to processing relies on super critical drying in a gaseous atmosphere such as CO_2 [91, 3]. Other methods include freeze sublimation and dry release methods such as vapor phase etching of sacrificial layers [8].

In order to mitigate in-use stiction failure, self assembled monolayers (SAM) are commonly employed to lower the surface energy of the device and surrounding surfaces. For example, in 1997 Man et al. [79] studied post release failure prevention using fluorocarbon coatings. Then in 1999 Maboudian et al.[76] used octadecyltrichlorosilane based SAMs to make the surfaces completely hydrophilic. The polar head of the molecules made strong contacts with silicon and resulted in good wear resistance of the monolayer. In 2003 Ashurst [8] used vapor phase coatings for the same purpose and achieved a much smoother surface with less particles, but with similar tribological properties to solution based methods. These coatings can reduce failure during manufacturing as well as in-service failure. However, none of these methods completely eliminate stiction failure [60].

Because no method guarantees that stiction failure will be completely mitigated, other researchers have worked on the repair of stiction failed devices. These efforts can be classified as in-service or ex-situ repair methods. The ex-situ repair methods generally involve a laser for either differential heating of the structures or creating a stress wave. Rogers et al. [106] developed a differential heating method wherein the MEMS structure was heated differentially with respect to its substrate. Forces attributed to the the thermal expansion of the MEMS structure caused the repair of the structure. Other researchers have used lasers to induce stress waves from under the MEMS structures to be repaired [71, 46]. A compressive stress wave transmits through the substrate and the stiction failed interface, reflecting off of the free interfaces of the MEMS structure. The reflected stress wave is tensile;

this tensile stress wave pulls apart the interface of the stiction failed device apart from the substrate thereby repairing the stiction failed device. In-service repair methods are few. One example of an in-service repair method is the use of structural vibrations induced by capacitive forces[110]. The structural vibrations cause the interface between the stiction failed device and substrate to undergo relative motion large enough to break the bonds between the surfaces thereby freeing the stiction failed device.

In either case of avoidance or repair of stiction failure, proper design of the method depends on knowledge of the critical strain energy release rate, "G". Mastrangelo et al. [80, 81, 82] laid the foundation for the commonly used Cantilever Beam Array (CBA) experiment which led the commonly accepted method of de Boer et al. [31]. Many other researchers have made measurements of G using these methods [71, 31, 69, 68, 70, 116, 30, 35, 34]. In most experiments the height of the μcantilevers' base above the substrate is held constant. However, in references [69, 68] the height of the μcantilevers above the substrate is variable and is termed a 'peel test.'

Much of the prior work relies on a linear relationship between the force and deflection of the μcantilever. Herein this method will be referred to as the 'linear' method. Using this linear description, G was found to be

$$G = \frac{3}{2}\frac{h^2 E t^3}{s^4} \tag{2.1}$$

where h is the height of the base of the cantilever above the substrate, E is the elastic modulus, t is the thickness of the beam, and s is the length of the beam which is not stiction failed onto the substrate. Eq. (2.1) is derived by making the assumptions that the slopes (and rotations) were small and that the deformations are due purely to bending. For stiction failed CBA experiments, in order for the rotations to be small and not to induce elongation in the structure (the cantilevers actually transform into fix-fix beams after failure), the deflection should be less than $\frac{1}{4}$ of the thickness of the structure [66, 40]. Additionally, when deflections are large,

the strain energy due to bending alone may not be sufficient to capture all of strain energy that is imparted onto the beam. Experimentally, it should be noted that the value for G is very sensitive to s and h. Inspecting (2.1), $G \propto \frac{h^2}{s^4}$. Thus it is imperative to measure s and h as accurately as possible.

In an effort to increase the accuracy of the measurement of G an improved model has been developed and utilized on the data obtained from peel test experiments. The model considers the large deflections of the beams and does not ignore stretching of the beams. Using the output of the nonlinear deflection model an energy method is employed that includes the effect of all forces in the system as well as the moments, leading to a more accurate value for G. In order to verify this new methodology, a set of peel test experiments were undertaken that determine s and h in an accurate manner by utilizing a vertical scanning interferometer.

2.2 Experimental Setup

The concept for these experiments is based on the peel test as developed for μcantilevers by Leseman et al. [69, 68]. At the core of the setup is a freestanding μcantilever beam that is stiction failed onto an independent substrate (see Fig. 2.1(Inset)). By moving the base of the stiction failed μcantilever in the y-direction, critical strain energy release rates can be determined. Because the μcantilevers and the substrate on which they are to be failed on are independent from one another, it is necessary to accurately orient the μcantilevers to the substrate. Thus multiple rotational and translational stages are necessary.

A total of 8 degrees of freedom (DOF) are necessary to accurately align a set of μcantilevers to the substrate on which they are to be stiction failed; 2 DOF's are rotational and 6 are translational. A picture of the final setup is shown in Fig. 2.1. The stages that facilitate the 8 DOF are grouped into two sets of stages, 'Group A'

and 'Group B'. Group A control the position and orientation of the μcantilevers while Group B control the position and orientation of the substrate. The handle in the rear of the Group A stages controls y-axis motion (Y_2 in Fig. 2.1). The large black stage is a piezoelectric stage with X_1, Y_1, and Z_1 motion capabilities. Connected to the black piezoelectric stage is a rigid macro-cantilever with a T-shaped cross section. This cantilever has the μcantilevers attached to it at its free end (see inset of Fig. 2.1). The substrate that lies under the μcantilevers is attached to translation stages that move in the x-z plane (X_3 and Z_3). Stacked on top of these translational stages, are two rotational stages that pivot around axes parallel to the x and z axes (θ_x and θ_z).

All 6 translational DOF's are orthogonal to one another with 3 being redundant. Though the direction of translation is redundant the resolution is not. All translational stages with handles have 1 μm resolution while the piezoelectric stages all have better than 1 nm of resolution. The rotational axes have 8 $sec \approx 0.0022^o$ of resolution.

The μcantilevered beams used for these experiments were fabricated at Sandia National Laboratories using the Sandia Ultra-planar, Multi-level MEMS Technology 5 (SUMMiT V^{TM}). This process uses a specific set of fabrication processes to make MEMS devices by surface micromachining using as many as fifteen masks [116]. A schematic of the lay-up of the films is shown in Fig. 2.2. The thicknesses of the deposited sacrificial oxides layers are shown on the left side of the figure. The right side dimensions are the thicknesses of the poly-Si layers. These dimensions are the nominal values and according to [33] they are prone to ±10% tolerance. The specific μcantilevers used in this process consist of the Poly-1 and Poly-2 layers without a layer of sacrificial oxide between them. μcantileveres used in this work were 1000μm long, 30μm wide and 2.3μm thick. SUMMiT μcantilevers were chosen due to the amount of work previously done in characterizing the critical strain energy

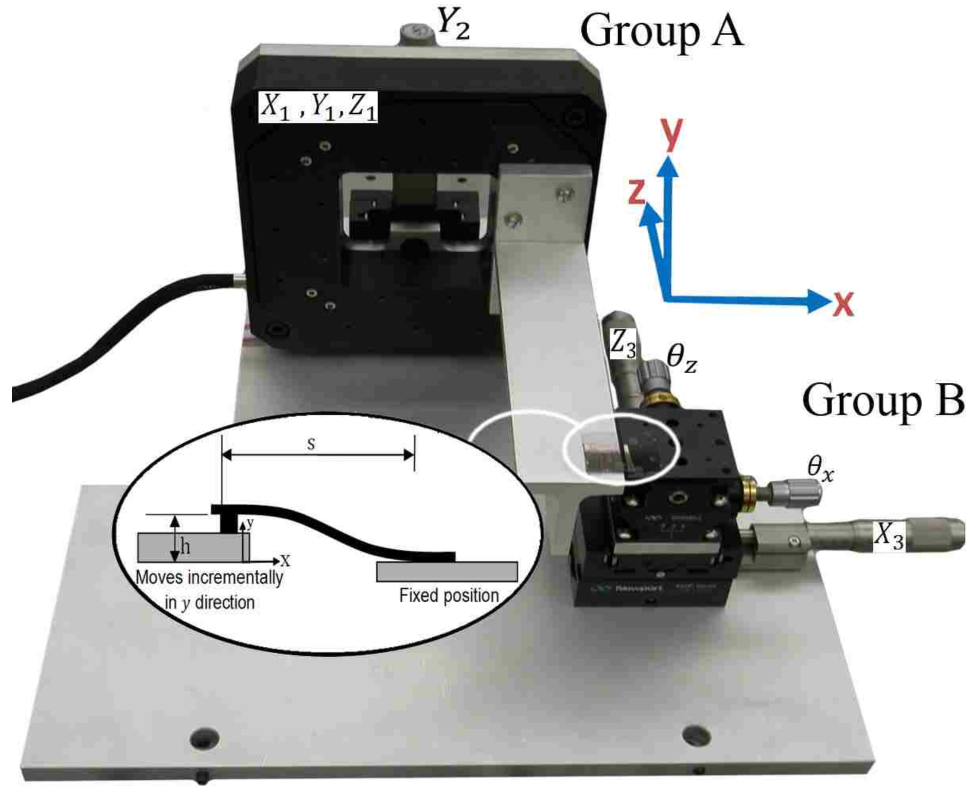

Figure 2.1: Experimental setup designed and fabricated to facilitate alignment and manipulation of μcantilevers and their substrate under the microscope lenes. Group B is the bottom-right stack of stages. Piezo-stage with the T-bar comprise group A.(Inset) Schematic representation of the Cantilever Beam Array (CBA) peel test experiment. The right stage is kept stationary while the left one is lifted vertically in a stepwise fashion. As the left stage is moved higher the crack length, s, continues to increase until the beam becomes completely detached from the substrate.

release rate of structures created with this process [70, 69, 68, 71, 31, 116, 30, 34, 50]. Previous results using μcantilevers and different characterization techniques are compared and contrasted in the Section 2.7.2.

Arrays of released μcantilevers were received from Sandia National Labs with substrates under the extents of the μcantilevers. In order to perform the peel tests the substrates were removed from under the free length of the μcantilevers. This was accomplished by scribing the substrate perpendicular to the length of the beam, near

their base, on opposing sides. Scribing, in this case, was performed using a Nd:YAG laser cutting system. The substrate is then fractured between the scribe mark leaving the μcantilevers with no substrate beneath them. The amount of substrate remaining under the free length of the beams was no more than 7 μm in length. This method produced no noticeable debris on or around the μcantilevers.

All experiments were conducted in a cleanroom environment. Experiments were conducted at an average temperature of 21.2 ^oC and relative humidity was controlled to 36% at an average pressure of 625 $Torr$.

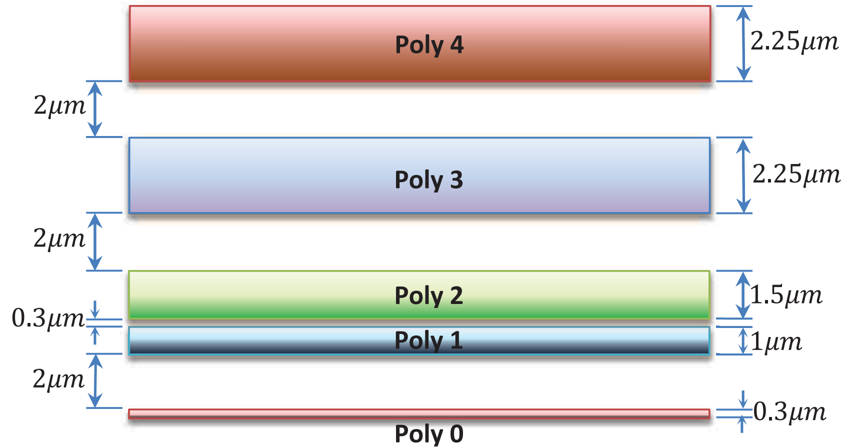

Figure 2.2: The physical layout of SUMMiT V^{TM} MEMS Technology. The five poly-Si layers are the main layers used for MEMS devices. Between each two layers of poly-Si there is a layer of oxide. The oxide layers are typically used as sacrificial layers only.

2.3 Experimental Procedure

The experimental procedure can be broken into three main steps. First the experimental apparatus (Fig. 2.1), is mounted on and aligned to the interferometer. Second, the μcantilevers are stiction failed onto the substrate. Third, the bases of

the μcantilevered beams are raised above the substrate, onto which they are stiction failed, and the μcantilevers' out-of-plane deformations are measured. Using the crack lengths, which are measured by postprocessing the μcantilevers' deformation data, the strain energy release rates can be determined.

Mounting and alignment of the experimental apparatus is multi-step process. For mounting, the baseplate shown in Fig. 2.1 is attached to the translational stage of the interferometer which is parallel to the x-z plane of the apparatus. Alignment of the μcantilevers and substrate to the interferometer is the next step. With the free ends of the μcantilevers positioned above the substrate onto which they will be failed, the head of the interferometer is adjusted using stages that rotate about the x and z axes. Once the μcantilevers are parallel to the interferometer, the substrate is brought into focus. In order to make the substrate parallel to the interferometer the goniometers from the Group B stages are adjusted. At this point the substrate is parallel to the interferometer and so are the μcantilevers. Therefore the substrate and μcantilevers are parallel to one another as well.

With the μcantilevers and substrate parallel to one another, the μcantilevers are stiction failed on the substrate. This is accomplished by lowering the μcantilevers using the Group A stages. The coarse stages are used for the initial approach and the piezo stages are used when the μcantilevers are within approximately 10 μm of the substrate. μcantilevers are positioned 2 - 3 μm above the substrate and then a drop of isopropyl alcohol (IPA) is placed on top of the μcantilever / substrate combination to induce stiction failure.

After the liquid used to stiction fail the μcantilevers has completely evaporated, the bases of the μcantilevers are raised in order to peel the stiction failed portion of the μcantilevers from the substrate. Using the y-axis of the piezo stage (Group A), the bases of the μcantilevers are indexed in the positive y-direction in 100 nm increments. At each increment an inteferometric image of the μcantilever beam array

is captured. These images contain the complete 3D information about the profile of each μcantilever. Postprocessing of these images can be used to reconstruct the 3D profile of these μcantilevers, e.g. see Fig. 2.3. Typically, more than 700 data points are captured for a single beam's deflection profile with an out-of-plane measurement accuracy of 3 nm. From these images the crack length, s, can be determined as a function of h, see Fig. 2.4. This data is later used to calculate the strain energy release rates of the beams as described in the subsequent sections. Note that the data reported herein is for a sample of four poly-Si μcantilevers failed on a poly-Si substrate. Data from all other experiments is consistent with this sample.

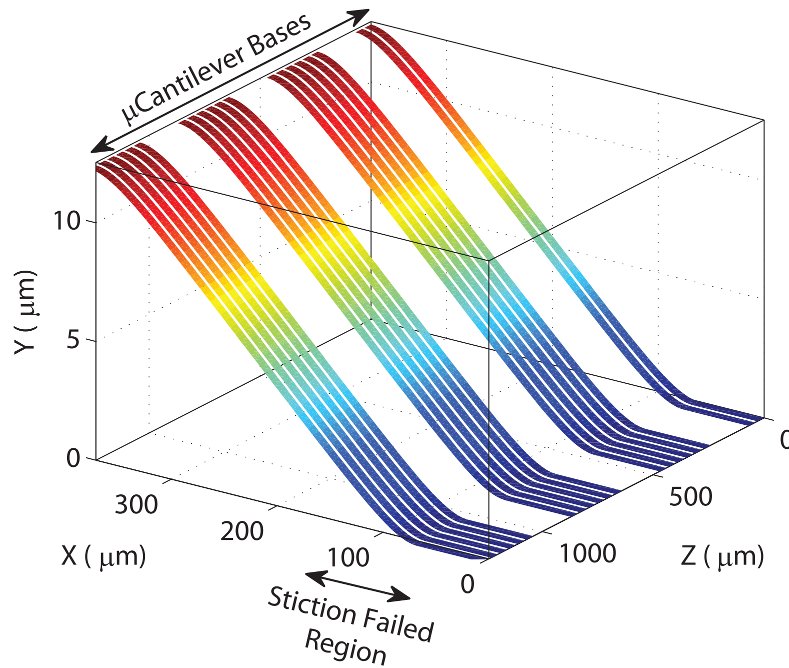

Figure 2.3: An example of the plots produced after analyzing the interferometry data. The beams have failed with an "s-shape" failure mode[31]. For this specific experiment the first $200\mu m$ of the beams is failed and stuck to the substrate. The plot shows the deflection of $1000\mu m$ long beams. Similar plots have been obtained for $500\mu m$ and $200\mu m$ long beams.

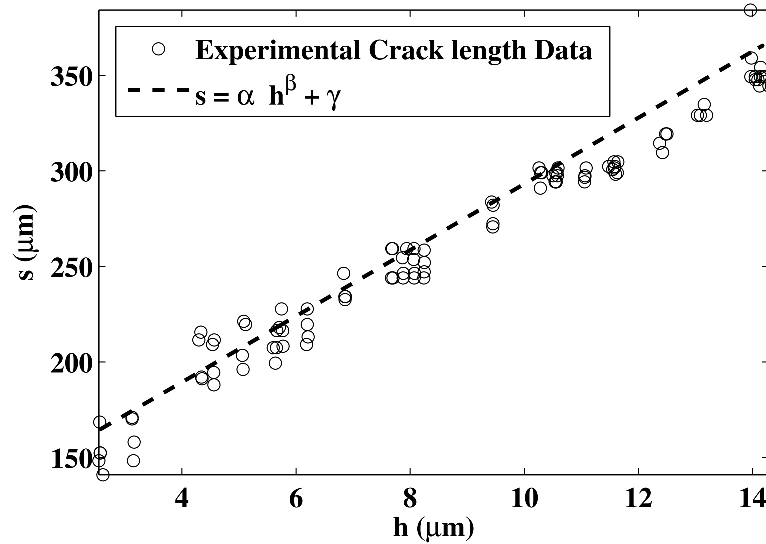

Figure 2.4: The variation of crack length(s) as a function of beam's height.

2.4 Nonlinear Beam Theory

In order to determine the critical strain energy release rate the total energy of the adhered beams needs to be determined. In absence of external forces acting on the μcantilevers, the total energy of the stiction failed μcantilevers consists of the energy stored due to the deformation of the μcantilevers (not just bending). Common approaches for determination of G assume small deformations, small rotations, free slip of the μcantilevers on the substrate, no residual stresses, and smooth surfaces. This leads to the conclusion that deformation of the beams is only due to bending. However, for cases where h exceeds $\frac{1}{4}$ of the thickness of the beam, a non-negligible amount of elastic energy is due to stretching of the beam [66, 40]. In absence of the free slip condition, herein a nonlinear model is developed for the deformation of a fix-fix beam that includes bending and stretching.

The shape of a homogeneous isotropic cantilever beam that has small deflections and rotations is governed by the differential equation of the deflection curve for a

beam, $M(x) = EIy''(x)$, in which, $M(x)$, is the bending moment, E, is Young's modulus of elasticity, I, is the second moment of inertia and, y, is the deflection at location x. Using the free body diagram of the beam (Fig. 2.5) the bending moment at a point (x, y) is found to be $M = M_0 + F_x y + F_y x$. In this equation M_0 is the bending moment and F_x and F_y are the normal and shear components of the forces at the anchor point, respectively. Substituting $M(x)$ into the curvature equation yields a second order nonhomogeneous linear differential equation that has a general solution in the form of:

$$y(x) = c_1 e^{\kappa x} + c_2 e^{-\kappa x} - \frac{M_0 + F_y x}{EI\kappa^2} \tag{2.2}$$

where κ is a dummy parameter defined as $\kappa = \sqrt{\frac{F_x}{EI}}$, c_1 and c_2 are constants that must be determined using the boundary conditions. Note that a similar solution is given by Frisch-Fay [40]. Boundary conditions for Fig. 2.5 are:

$$\begin{aligned} y(0) &= 0 \\ y(s) &= h \\ \theta(0) &= 0 \\ \theta(s) &= 0 \end{aligned}$$

As shown in (2.3) and (2.4), using the aforementioned boundary conditions, c_1 and c_2 can be determined as functions of κ.

$$c_1 = \frac{-h}{2 + s\kappa + e^{s\kappa}(s\kappa - 2)} \tag{2.3}$$

$$c_2 = \frac{e^{s\kappa} h}{2 + s\kappa + e^{s\kappa}(s\kappa - 2)} \tag{2.4}$$

In these experiments no horizontal displacement is allowed at the anchor points. This constraint makes the beam a first order hyperstatic system by introducing an unknown force F_x on the beam. In order to solve this system of equations additional

knowledge of the mechanical properties and geometry of the beam are employed. Poly-Si is a linear elastic material. As such, Hooke's Law, (2.5), is invoked in order to determine F_x. For this work Hooke's Law takes the form:

$$\frac{L - L_0}{L_0} = \frac{F_x}{AE} \tag{2.5}$$

where L is the deformed length of the beam, L_0 is the initial length (taken here as s), and A is the cross sectional area of the beam. All variables in (2.5) are known except L and F_x. The deformed shape of the beam is known to be a function of F_x which affects the length of the beam along its longitudinal axis. The total length of the beam can be calculated by determining the length of the curve defined by (2.2). Specifically, (2.6) is used for this purpose.

$$L = \int_0^s \left(\sqrt{1 + \left(\frac{\partial y(x)}{\partial x} \right)^2} \right) dx \tag{2.6}$$

(2.2) - (2.6) are solved numerically in order to obtain the results reported here. The general solution process begins by inputting values for s, h, and F_x. s and h are immediately available from the experimental data, while F_x requires an initial guess. Note that s and h can be left as free parameters with bounds from the experimental error in order to attain more accurate solutions. With these values (2.2) - (2.4) can be solved to determine $y(x)$. The deformed length is then found using (2.6). Finally, the left hand side of (2.5) is solved. This result is compared to the value of the right hand side of (2.5) with F_x from solving (2.2) - (2.4). If the two are not equal, then F_x is adjusted iteratively. When the two sides are equal the solutions are valid. Typically, the error between the two sides of (2.5) is less than 10^{-18}. For these calculations E was considered to be 170 GPa.

During peeling the anchor point is not allowed to have horizontal movement. Note that this constraint is typically for most MEMS structures that have moving parts. It has dramatic effects on transverse-force/deflection behavior of the beam. As seen

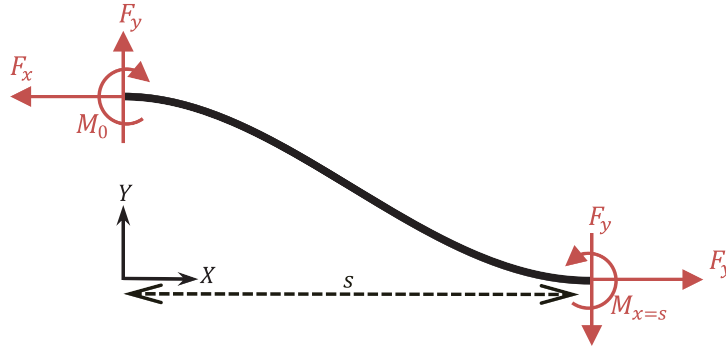

Figure 2.5: At each increment of h, the polyslicon beams studied here can be modeled as fix-fix beams. The free body diagram of the beam includes a bending moment at each end as well as a horizontal and a vertical force. The beam is statically indeterminate.

in Fig. 2.6 the beam displays nonlinear stiffness as its height increases. The plot also shows the linear force/deflection behavior of a fix-fix beam with a small deflection assumption. The linear model deviates by more than 5% for displacements greater than 27.07% $\approx \frac{1}{4}$ of the beam's thickness. For these experiments the beams were 2.3 μm thick. Thus for an $h > 622\ nm$ the deflection should be considered nonlinear. Furthermore, for the SUMMiT V^{TM} process of Fig. 2.2, any poly-Si layer which fails on the poly-0 layer must use the nonlinear model to minimize errors.

The data collected for this manuscript was analyzed using the method described previously. For all values of h, the nonlinear model fits the data better. Specifically, the rate of root mean square (RMS) error for the linear model increases at a rate more than double that of the nonlinear model. An example of the type of fit attained is shown in Fig. 2.7.

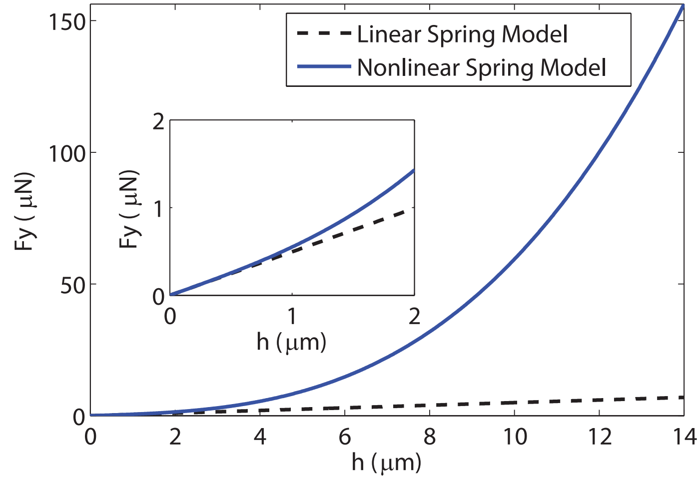

Figure 2.6: Comparison between the linear and nonlinear spring models of a $500\mu m$ long hyperstatic fixed guided beam. h shows the height defence between the two ends of the beam.

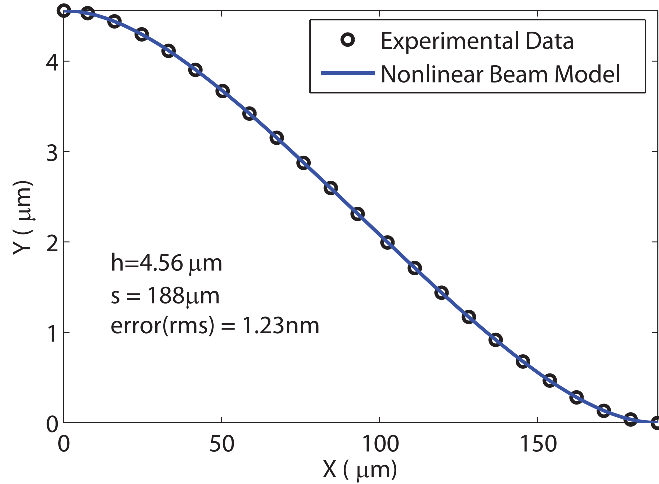

Figure 2.7: The μcantilevers used here behave nonlinearly for crack heights bigger than $622nm$. Here the nonlinear model of the μcantilever and the experimental data for a crack height of $3.96\mu m$ are shown in the same plot. Although $3.96\mu m$ crack height falls well into nonlinear domain, the model matches the experimental data with an error less than $1.23nm$.

2.5 Strain Energy Release Rate Formulation

Griffith's criterion predicts that a crack will propagate when the work done by the external forces exceeds the summation of elastic energy stored in the beam and the energy stored in the crack tip. In the case of displacement controlled crack development, since each arrest happens at a constant crack height, the external force does no work during each crack arrest. Thus the strain energy release rate is defined as:

$$G = -\frac{1}{w}\frac{\partial U}{\partial s} \tag{2.7}$$

In this equation, U and w represent the elastic energy stored in the μcantilever and width of the μcantilever, respectively. Note that due to the nature of these experiments the arrested crack value is reported. When h is smaller than one-fourth of its thickness, the beam's behavior can be approximated by a linear spring, but as h increases, a nonlinear model must be utilized (see Section 2.4). In the linear case, U can be readily found by using:

$$U = \int_0^s \frac{M^2}{2EI}\, dx \tag{2.8}$$

(2.8) considers that the beam's strain energy is only due to bending. Had its deformed shape and strain energy only been due to bending, it would have followed the linear model in Fig. 2.6. Clearly, for $h > 622nm$, the beams' behavior is not linear. Thus the nonlinear model developed in Sect. 2.4 models the deflection of the μcantilevers more accurately. In order to find the elastic strain energy associated with the nonlinear model, it is necessary to integrate the work done by each of the forces and moments acting on the beam during its entire deformation history.

The strain energy stored in the silicon beam is equal to the total mechanical work done on the beam while inducing the deformation. The work done on the system can be decomposed into three parts: the work done by shear forces, normal forces,

and bending moment. The total strain energy stored in the beam as well as different contributions due to each force and moment are calculated in Sect. 2.7.2. This section demonstrates that relatively large longitudinal stresses can develop during the experiments and that the magnitude of the induced longitudinal stress is dependent on the height of the anchor point h.

2.6 Calculating Strain Energy and its Contributions

Since poly-Si is a linear elastic material, despite the presence of geometric nonlinearities, the strain energy stored in a poly-Si μcantilevers is conserved. Any quantity with this property is mathematically defined as having a complete differential. Therefor the changes in the strain energy's value are path independent and a function of the initial and final configurations only.

The energy stored in a beam can be calculated by integrating the infinitesimal work done on the beam while it is being deformed from the free and straight initial configuration to its final configuration (Fig. 2.8). The total work done on the beam, in an arbitrary deformation, can then be represented as (2.9).

$$U = \int_0^h F_y \, dy + \int_0^{x_0} F_x \, dx + \int_0^{\theta_0} M_0 \, d\theta \tag{2.9}$$

One possible path to reach the final configuration is one in which the beam moves only vertically from $y = 0$ to $y = h$, while satisfying the zero slope and no horizontal motion constraints. During this process, the second and third term of (2.9) will be zero since there is no displacement in the direction of F_x and M_0. Simplifying the total work equation to (2.10). It is important to notice that although F_x and M_0 do

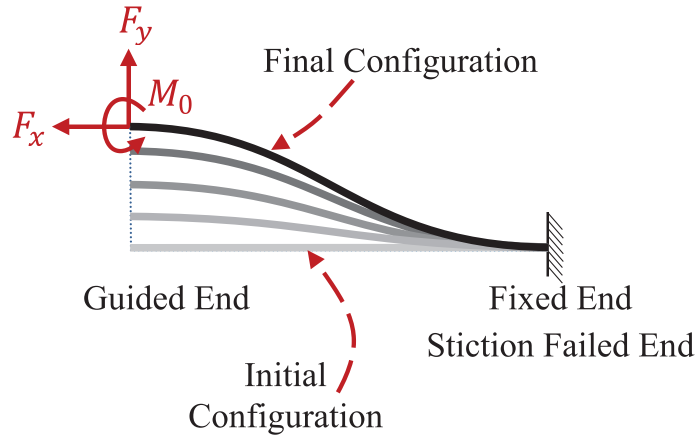

Figure 2.8: The total work done on the μcantilever can be obtained by integrating the infenitesimal work during its deformation from initial straight configuration to the final configuration.

not seem to directly do work, their presence dramatically affects the value of F_y and doing so, indirectly contributes to the total strain energy stored in the beam.

$$U = \int_0^h F_y \, dy \tag{2.10}$$

Although (2.10) does not explicitly contain F_x and M_0, F_y is actually a function of these quantities, see (2.2) - (2.6). The presence of F_x and M_0 dramatically affects the overall value of F_y. Figure 2.10 depicts the strain energy versus crack height by numerically integrating (2.10). Four cases are depicted in Fig. 2.10. First, the total strain energy is given using F_y that contains both F_x and M_0. The other three cases correspond to the individual contributions of F_y, F_x, and M_0 to the total strain energy. By segregating the effects of each load and moment it is clear that for increasing crack heights h, F_x is the major contributor to the strain energy stored in the μcantilevers. Furthermore, F_x leads to tensile stresses in the μcantilever, see Figure 2.12. Tensile stresses in these experiments reach a value of more than $100 MPa$, which is nearing the fracture strength of poly-Si from the SUMMiT V

process [122]. To wit, in some experiments μcantilevers actually fractured at their bases for large values of h.

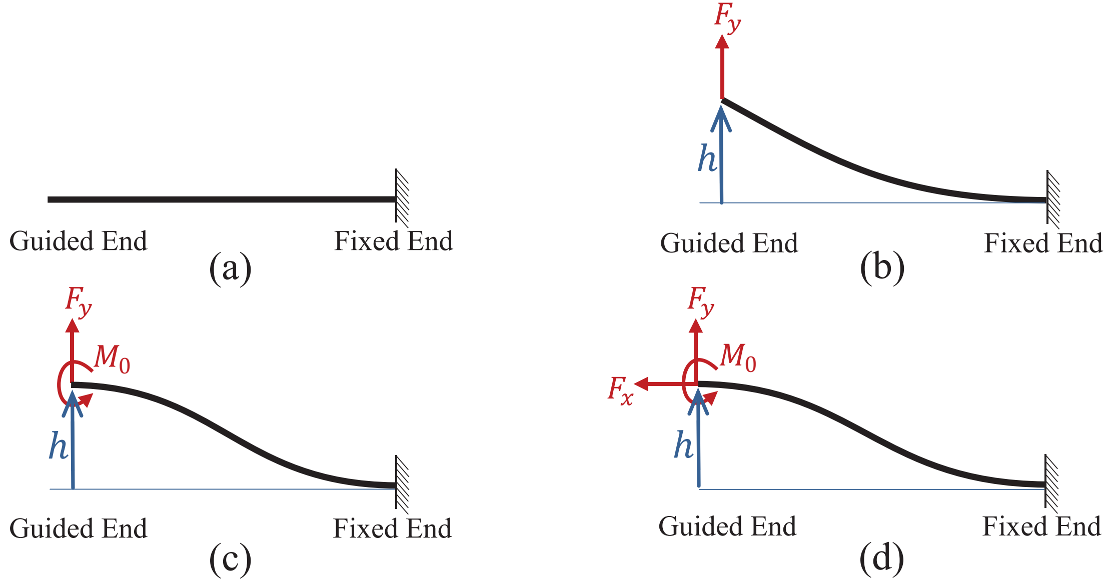

Figure 2.9: The deformation of the μcantilever from its free configuration can be considered as a result of three subsequent displacements. First lifting up to the final height, h, then imposing the zero slope condition by applying the bending moment, M_0 and then making sure that the net horizontal displacement is zero by applting F_x.

2.6.1 Results for the Strain Energy Release Rates

Applying the methods of the previous section and using (2.7), the strain energy release rates are determined for different crack heights as shown in Fig. 2.12. This figure displays one set of data analyzed in two different ways. The red $\Diamond$ represent the strain energy release rates calculated using linear modeling assumptions (2.8) and blue circles represent values obtained by using the nonlinear method developed here, Eqns. (2.2)-(2.6) and (2.10).

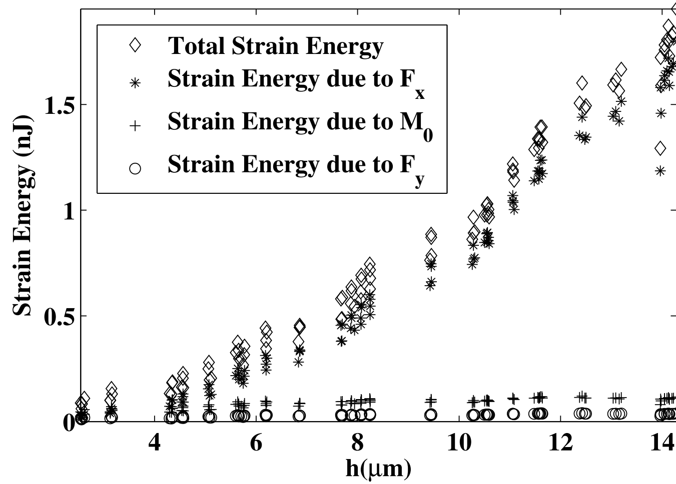

Figure 2.10: The contributions of different external forces and moments in the total work done on a μ cantilever under large deflections are compared. The plot shows the increasing effect of longitudinal stress is the crack height(deflection) gets larger.

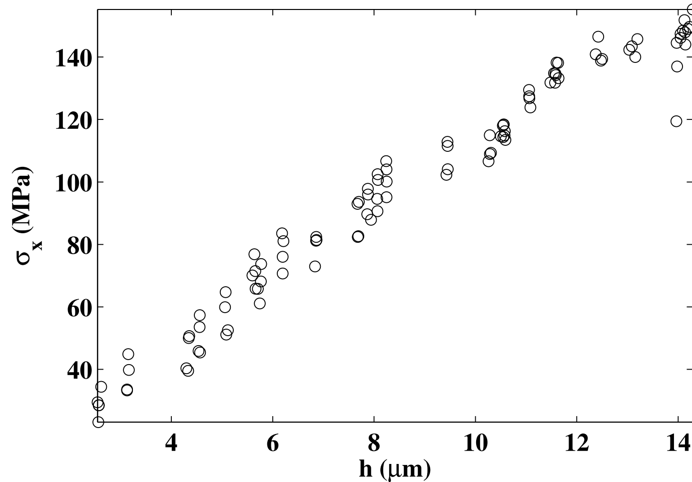

Figure 2.11: Longitudinal stresses that develop in the μcantilevers are plotted as a function of crack heights. The tensile stress develops because of the nature of the experiment which prevents any horizontal displacement of the anchor point.

2.7 Discussion

The discussion of the results are broken into two subsections. First a theoretical subsection discusses the results of the new nonlinear formulation and its applicability

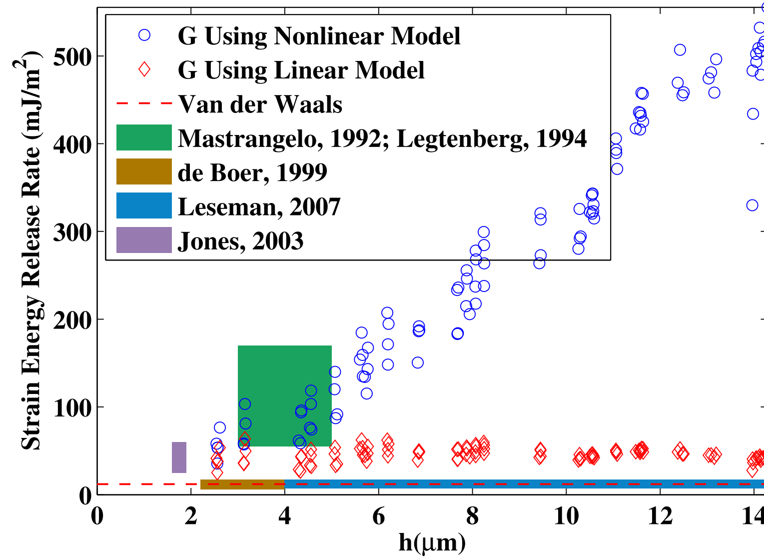

Figure 2.12: The strain energy release rates ar calculated using a single set of data analyzed in two different ways. "◊" and "O" represent the results of linear and nonilnear analysis respectively. The results of previous reports are also included for camparision.

to determination of G values in comparison to the previously used linear formulation. The second subsection discusses the experimental findings. Specifically, the model is applied to the experimental data and conclusions are drawn about how well the model works to match experimentally measured deflections and report the G values. Additionally, a discussion ensues about how G can vary as a function of surface conditions and loading. Results from this work show larger values for h compared to previous reports and it is concluded that the loading condition of the structure dramatically affects the value of G.

2.7.1 Modeling Discussion

The main results of the theoretical analysis are the nonlinear model of stiction-failed-μcantilevers (Section 2.4) and the determination of the strain energy release rates using an energy method (Section 2.5). Fig. 2.6 compares the linear (deflections/rotations small and no centerline stretching) and nonlinear (deflection/rotations small and centerline stretching) models of μcantilevers with fix-fix boundary conditions. This particular plot is for a beam whose thickness is 2.3 μm. It can be seen that the nonlinear model deviates from the linear model by more than 5%, for $h > 622\ nm$, which corresponds to $F_y = 323.6\ nN$. This result can be generalized to reflect that any beam with fix-fix end conditions can have its deflection modeled using a linear model only if $h \leq 0.27\,t$, where t represents the thickness of the beam. As h increases however, the nonlinear model must be used in order to avoid large errors in modeling the deflection profile of the beam. Of course the nonlinear model is applicable for $h \leq 0.27\,t$ as well.

Fig. 2.7 compares the theoretical and experimental shape for a μcantilever with a crack height of $h = 3.96\mu m$. The RMS error for the nonlinear model's fit to the experimental data is 1.23 nm. For the case of the linear model its RMS error is $23.31 nm$. The nonlinear beam model is more accurate than the linear model for the entire range of h. As h is increased, the RMS error for both the nonlinear model and linear model increase linearly. However the linear model's RMS error increases at a rate 2.2 times faster than the nonlinear model. Clearly, considering axial stretching (F_x development) of the beam leads to more accurate solutions for the deflection profile of the μcantilevers.

In order to determine G, the elastic strain energy stored in the beam must be determined. Prior to this work, strain energy stored in the beam due to bending (see (2.8)) was commonly considered as the main component of the strain energy,

ignoring the energy associated with elongation of the beam. At small values of h the longitudinal force is ignorable, see Fig. 2.11, and it plays very small role in the total work done on the beam. However, for large crack heights ($h \leq 0.27\,t$), the nonlinear model shows that contributions of forces F_x and F_y, are considerable. F_x dominates all other contributions for these relatively large values of h, see Fig. 2.10.

The nonlinear beam model is used to determine the deformed shape of the μcantilever as well as F_x, F_y, and M_0. The development of F_x implies that the μcantilever stiction failure must be considered as a Mixed Mode (I & II) fracture problem [74]. Previously it was only considered a Mode I problem. Using the F_x values obtained using (2.2) and (2.5), the longitudinal stress developed in the beam is easily determined. Fig. 2.11 demonstrates how the magnitude of axial stress, σ_x, changes in the peel test method as h increases. Due to these relatively large longitudinal stresses, a considerable shear component is imparted at the μcantilever-substrate interface. This shear stress imposes a Mode II type failure component whereas previously it was considered to be only Mode I. Note that the formulations for the strain energy release rate developed in Section 2.5 capture the total strain energy in the deformed beam, contributing to both Mode I and II types of fracture.

In order to better understand the advantages of the proposed method for determining G which incorporates the nonlinear beam model and the energy method, its results are compared with the prior method which utilized the linear beam model used in conjunction with (2.8). One finds that in the linear method $G \propto \frac{h^2}{s^4}$, (see (2.1)), while in the nonlinear method $G \propto \frac{h^6}{s^4}$. This was attained by using the Taylor's series expansion of (2.2) - (2.4) in order to find G. Note that both the linear and nonlinear models are dependent on s in similar manners, but the nonlinear model is h^4 times more dependent on h. This is a direct result of considering longitudinal extension of the μcantilever. The increased sensitivity of G to h in the nonlinear method results in larger values for the strain energy release rates compared to those

previously reported, see Fig. 2.12. In summary, the values for G reported previously are expected to be lower than their actual value, because all previous reports had $h > .27\,t$ and none of these reports considered the nonlinear deformation of the beam and all contributions to the strain energy.

2.7.2 Experimental Discussion

The results of the experiments after analysis with the new theory, yields two main conclusions. First, values found with the new procedure are higher than those previously reported. Secondly, G increases with increasing height of the base, h, above the substrate. The following discussion details insight on each of these conclusions.

The average value of G for the newly derived model is higher than previous reports. Figure 2.12 shows one set of data analyzed in two different ways. The data marked by "◊" represent the values attained using the linear formulation, (2.7). This method yields an almost constant value for G, a little bit larger than previous reports by de Boer [31] and Leseman [69] but similar to Jones [50], Legtenberg [66] and Masterangelo [80]. Note that the values are relatively low when compared to bulk Si [20], but larger than van der Waals[48], see red line in Fig.2.12. The data points marked by "o" on Figure 2.12 are found using the nonlinear model previously described, including the effects of M_0, F_x, F_y in calculating the strain energy, as discussed in Section 2.5. Both of the data sets show similar values for small h's. However, when all contributions to G are considered, values nearing $600\,mJ/m^2$ are found for h's of $\sim 14\mu m$.

Post processing the strain energy release rate data, it was observed that a hyperlinear relationship of the form $G = \alpha\, h^{\beta} + \gamma$ exists between strain energy release rate and crack height. For the results reported here, $\alpha = 18.085$, $\beta = 1.004$ and $\gamma = 0.121 * 10^3$. The offset factor γ is introduced since it is practically difficult to

make sure that $h = 0$ corresponds to zero crack length. It is preferred to have a small gap between the μcantilever and the substrate when introducing the liquid, to ease wetting and homogeneous failure. β is the degree of nonlinearity and α indicates the rate of change of strain energy release rate as a function of crack height. The observed increase for the value of G is somewhat surprising, but can be understood considering the surface conditions and loading conditions. Both α and β are variables depending on external factors such as humidity, loading conditions (specifically at the front of crack tip) and the surface roughnesses involved.

The bottom side of the beam has an average roughness of 24.94 nm and the substrate has an average roughness of 4.27 nm as received from Sandia National Labs. This has been independently verified by the authors using an AFM measurement and also corroborated by [24]. Due to existence of roughnesses, the entire area of the μcantilever beam does not come into intimate contact with the surface below it. Thus contact occurs at asperities which has been the study of others [30, 134, 135, 83]. The important consideration for the current work is the existence of the asperities. The actual contact area between the two surfaces is therefore controlled by the external forces applied on the μcantilever. For small values of h this value is relatively low. As h increases the value of F_y and M_0 both increase monotonically. Thus the two surfaces are pressed together more intimately. If the asperity contacts are considered to be Hertzian in nature then as F_y increases linearly the area, "A", of contact increases between the surfaces as $A^{\frac{3}{2}}$. Thus as the height of the base increases, the load and subsequently the contact area increase.

2.7.3 Practical Considerations

The poly-Si μcantilevers and substrates used for these sets of experiments were fabricated using SUMMiT V^{TM} process. Much of the previous reports also used this

process [70, 69, 68, 71, 31, 116, 30, 34, 50]. SUMMiT V^{TM} is one of the most common methods to produce surface micromachined MEMS devices. Using this process the height difference between a poly-Si layer and the substrate can be as high as $10.75\mu m$ or as small as 300 nm, see Fig. 2.2. In this paper, the strain energy release rate is studied up to a height of $h = 14.2\mu m$. And it is shown that the beams behave linearly only up to $h = 622$ nm. The measurements reported here cover the entire range of crack heights possible in SUMMiT V^{TM} and most of the other common processes.

An additional consideration is the use of this model for devices that fail during service. Typically, h is at a fixed height and does not vary as in the peel test. Usually a μcantilever will fail initially in an arc-shaped failure mode [31] and upon additional application of force, will fail in an s-shaped manner. This transition from an arc to an s-shaped failure mode will cause the μcantilever to begin to store tensile strain energy in both the failed length and the deflected length of the beam if there is no slip. The model developed in this paper is robust enough to capture all of the residual strains in the deflected length of the beam because it utilizes a fit to the experimental data in order to determine the actual F_y, M_0, and F_x.

The idea of considering nonlinear deflections for micro and nano mechanical devices is of great importance due to the slenderness ratios and deflections of most structures. The final practical comment that comes from this work is the applicability of the overall idea. Generally, for any deflection of a structure that contains more than one fixed point stretching should be considered. Devices more complex than a μcantilever can be modeled with finite elements to determine the stretching. Similar energy methods, such as those in Sec. 2.5, can be used in order to determine values for G in a given process.

2.8 Conclusion

In this article, a new method was developed for determining the total strain energy stored in μcantilevers, which both directly and indirectly includes the effects of all the forces as well as the moments present. The developed model is applicable for small deformations as well as large deformations. For small deformations, the developed model agrees well with common linear models but as the deformations increase, the two models deviate. Using the more sophisticated method developed here, the strain energy release rate was determined more accurately. Based on the experiments performed and using the models developed, the strain energy of poly-silicon / poly-silicon surfaces was found not to be a constant value but increased monotonically as the beams were peeled off of the surface. The strain energy release rate was found to be highly sensitive to parameters like the crack size and height, surface roughness and loading conditions at the crack tip. The maximum crack height studied was 14.2 μm. Since most MEMS devices do not experience such large deflections, one can consider 600 mJ/m^2 as an upper bound for the strain energy release rate for poly-silicon / poly-silicon MEMS surfaces. It was also found that due to the presence of noticeable longitudinal stresses, the crack propagation must be considered as a mixed mode(Mode I & II) crack propagation problem. As the height of the beam was increased, the effect of Mode II became more appreciable.

The existence of a relatively large Mode II component in the otherwise known as Mode I crack propagation experiments of this chapter demands a closer study of a pure mode II crack propagation and its effects in crack propagation and critical strain energy release rate. Next chapter will use a custom made MEMS apparatus to measure the force as well as displacement of a μcantilever purposefully stiction failed on a poly-Si substrate. It will be shown that the results obtained by post-processing the experimental data of Chapter 3, go hand in hand with the results obtained in the current chapter completing the left end of the critical strain energy release rate

curve shown in Fig. 2.12.

2.9 Acknowledgments

The authors acknowledge support from the National Science Foundation (CMMI-0826580). Portions of the work were carried out in UNM's Manufacturing Training and Technology Center and UNM's Nano Synthesis Facility. Thanks to M. P. de Boer for valuable discussions.

Chapter 3

Mode II Crack Propagation In Poly-Si μcantilevers

3.1 Overview

Though many types of MEMS have made it to market and are a part of daily life, but not explicitly noticed, to date there are still no MEMS, which contain moving parts that have rubbing surfaces. In article by Romig et al., a taxonomy for MEMS devices was developed [107]. In this taxonomy MEMS were broken into four classifications. Class I devices contain no moving parts. Examples of Class I devices are strain gauges and ink jet printheads [51]. Class II MEMS have moving parts but no (intentional) contact between surfaces. Examples of this class are gyros, comb drive actuators, and resonators [45]. Class III MEMS have moving parts and impacting surfaces. Examples of these are TI's DMD, micro-relays, valves, and pumps. Class IV MEMS devices have moving parts, impacting surfaces, and rubbing surfaces. Though the first three classes of MEMS all have examples that are currently commercially available Class IV devices currently do not.

Class IV MEMS are not commercially available due to issues they encounter with adhesion, friction and wear. Because of the length scale on which MEMS and their nano counterparts NEMS exist, surface forces dominate even over gravitational forces. These issues impair the reliability of the device and make their mass production less attractive to manufacturers.

In an effort to mitigate adhesion, friction and wear in MEMS researchers have reverted back to use of lubricants. Lubricants commonly used are OTS, DDMS and self-assembled monolayers [10, 9, 76, 58]. These lubricants are in the form of monolayers on the surfaces of the devices. Though chemically bonded to the substrate, these coatings can not completely avoid wear and eventually wear off. These choices of lubricants differ from common lubricants for macroscopic systems. This is due to the fact that MEMS are commonly made from Si; not a common structural material at the macroscale.

Herein a technique is developed where two Si surfaces are 'rubbed' on one another in a controlled manner. Controlled stick-slip events are induced. By instrumenting one of the surfaces with a force sensor, the static friction force, kinetic friction force, and adhesion energy between the surfaces can be determined. In this work, the surfaces are both 'dry' and no lubricant is used. Future efforts will include a study of lubricants and their effects.

3.2 Experimental setup and procedure

The experiential setup used here for the Mode II peel tests, is composed of three basic components: a μcantilever beam, a flexural MEMS force measurement device and an independent poly-Si substrate. The μcantilever beam is the actual specimen, which is to be purposefully stiction failed on the poly-Si substrate. The MEMS device on the other hand, is responsible to facilitate peeling the stiction-failed μcantilever off

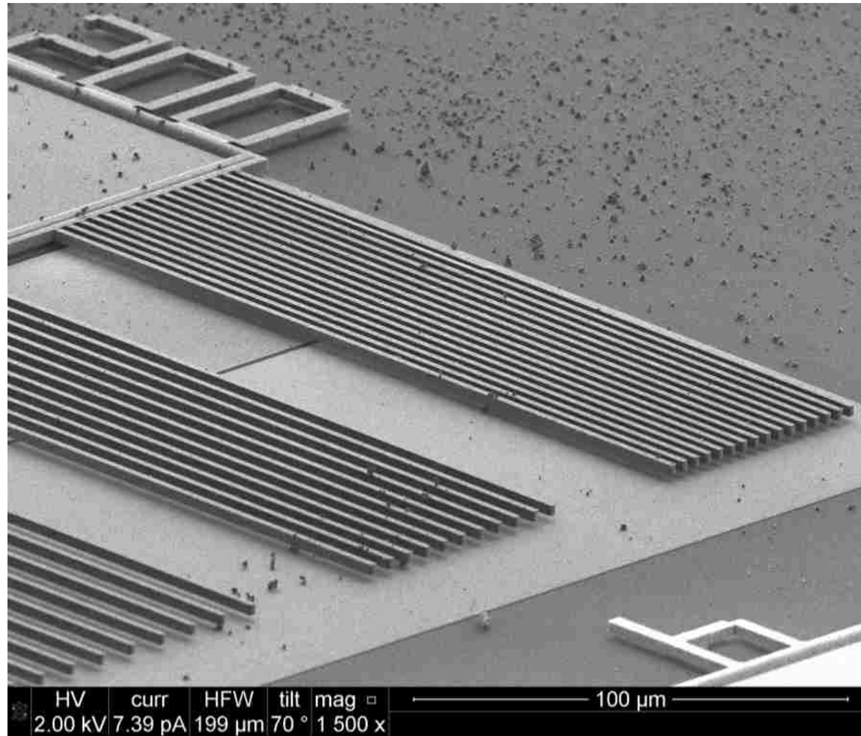

Figure 3.1: An example of μcantilever array. The μcantilevers here are $200\mu m$ long, $2\mu m$ wide and $2\mu m$ thick.

the substrate while providing means to accurately measure the force acting on it.

3.2.1 The μcantilever beam

The μcantilever beams utilized in these experiments were fabricated at Sandia National Laboratories using the SUMMiT V^{TM} process [116]. Sandia's poly-Si μcantilevers have been the major source of recent stiction failure and MEMS peel test experiments [86, 71, 68, 102, 29, 31]. Each SUMMiT V chip contains numerous arrays of μcantilever beams (see Figure 3.1) with different lengths and widths. In order to assemble our mode II experimental device a single μcantilever ($1500\mu m$ long and $30\mu m$ wide) is cut from the μcantilever array and welded to the MEMS force measurement

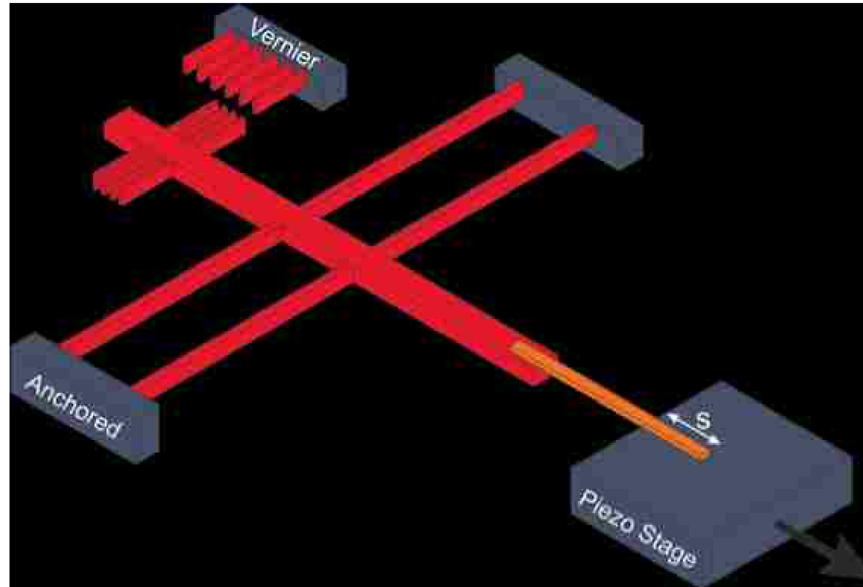

Figure 3.2: Schematic representation of Mode II experimental setup. The force measurement MEMS device is shown, in red, on the left representing the rigid shuttle, four flexural arms and the vernier. The μcantilever specimen is welded on the left end of the shuttle and is stiction failed on the substrate fixed on the piezo stage on the right.

apparatus.

3.2.2 The MEMS force measurement unit

The MEMS device used here is illustrated in Figure 3.2. The device is composed of a floating rigid shuttle connected to its native substrate through four compliant arms. It is also equipped with a vernier which can be used to measure the relative motion of the shuttle with respect to the substrate with 100nm resolution.

The flexural arms are more than 2000 times more compliant than the shuttleand can be considered as four fixed-guided (or equivalently as two fixed-fixed) flexural beam springs. The elastic energy stored in this parallel spring system restores the

device to its original configuration once external excitation is removed. Due to the parallel configuration, the deflection in each arm is equal to the displacement of the shuttle and its transverse force contributes to $\frac{1}{4}$ of the total reaction force acting on the shuttle. This force can be accurately determined once the shuttle deflection is measured using the vernier mechanism(see Figures 3.2 & 3.3).

The fabrication process followed to make the MEMS actuator is detailed in [67] and [1]. The following is a brief discussion of the process. A (100) Silicon on Insulator (SOI) wafer with $20\mu m$ thick device layer, $1\mu m$ buried oxide (BOX) and $600\mu m$ handle layer was utilized. The device and the handle layers are both p-type doped with boron. A single mask process was used to transfer the pattern onto the photoresist (PR). The Si device layer was then etched to the BOX layer by deep reactive ion etching (DRIE) using the Bosch Process [62]. This anisotropic process creates high aspect ratio structures by nearly vertically sidewalls. The PR layer is finally removed using acetone, isopropyl alcohol, and deionized (DI) water rinses. Oxygen plasma is then used to remove any small remaining amount of PR on the Si surface. Finally, the actuator is released by etching the BOX layer in HF bath and rinsed in DI water.

3.2.3 Independent substrate

In order to be consistent with the μcantilever beam sample a SUMMiT V^{TM} poly-Si substrates is used as the target for stiction failure. This makes sure that the poly-Si μcantilever sample is stiction failed on a substrate of similar material and consistency.

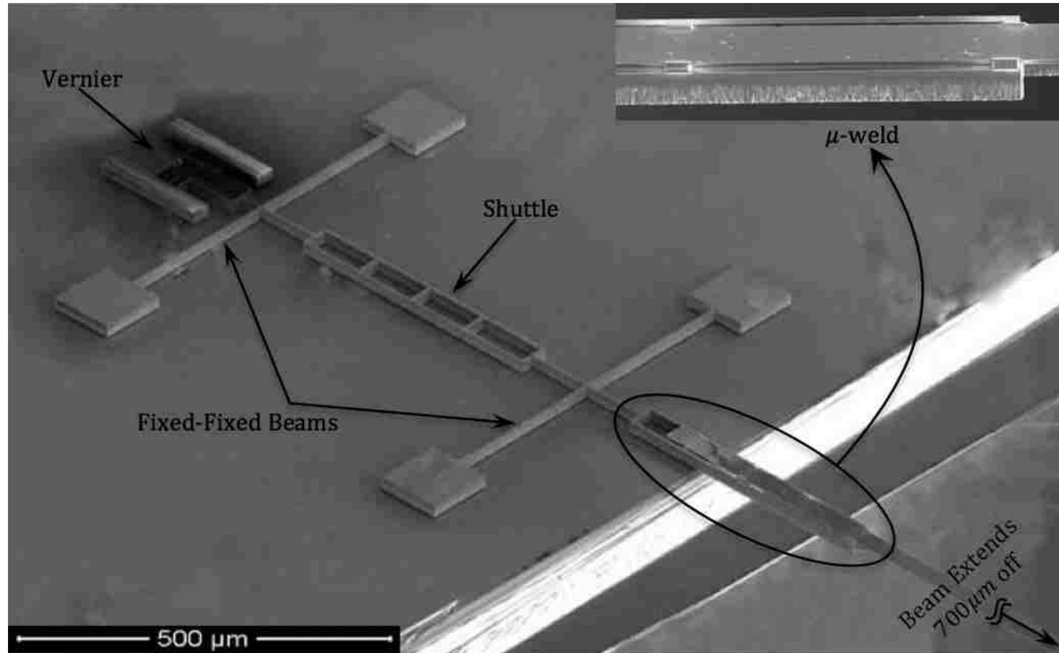

Figure 3.3: SEM image of a Mode II experimental device with a μcantilever beam welded to the shuttle of the MEMS Actuator. Note that the μcantilever extends beyond the edge of the image for almost another 700m. Inset: This close up shows how the μcantilever is welded to the shuttle using platinum spot welds.

3.2.4 Experimental setup assembly

In order to prepare the experimental assembly illustrated in Figure 3.2, a single μcantilever beam is separated from the μcantilevers array and welded to the shuttle of the MEMS force measurement device(see Figure 3.3). An Omniprobe mounted inside of DualBeam Quanta 3D FEG is used for this purpose. The Dual-Beam Quanta 3D FEG is an instrument wherein a Scanning Electron Microscope (SEM) and Focused Ion Beam (FIB) are integrated onto the same vacuum chamber. The SEM is used to capture realtime images while a single μcantilever is cut off a μcantilever array and welded to the MEMS actuator using the FIB. Omniprobe is a probe tip mounted inside the Quanta 3D FEG capable of manipulating micro and nano-devices. The Omniprobe is welded to a clean μcantilever before it is cut from its anchor and used

as a handle to move it around and align it to the MEMS device. The properly aligned μcantilever is then welded on to the tip of MEMS device shuttle. Once the μcantilever is fixed on the shuttle the OmniProbe is cut off using FIB again. Figure 3.3 shows the final setup with the independent substrate brought under the protruding μcantilever. This figure also shows a close up of the welds. The welding process uses a gas injection system (GIS) to provide the metallic particles. The GIS used, delivers a carbonaceous precursor in which Pt is contained. When the FIB is focused on a spot Pt (and some carbon) is deposited in that region. The deposited Pt is what is referred to as the 'weld'.

3.3 Experimental procedure

In these experiments the bottom surface of the protruding μcantilever beam is purposefully stiction failed on the independent substrate and then peeled off along its length in a stepwise fashion. The peeling force is generated by the piezo stage and transmitted to the μcantilever by the MEMS force measurement apparatus. From the perspective of fracture mechanics, a crack propagates when the strain energy release rate reaches its critical value also known as the adhesion energy of the surfaces engaged.

Before the actual stiction failure is induced, the independent substrate needs to be accurately aligned with the μcantilever and brought into close proximity of its lower surface. This is accomplished using the custom made setup schematically shown in Figure 3.4. The two goniometers and three micro-positioners assembly on the left provides all rotational and translational degrees of freedom needed to accurately align the substrate and bring it to the desired location under the μcantilever.

The MEMS load cell is rigidly attached to the x-y-z piezo stage, illustrated on the right, with $1nm$ resolution on each axis. This assembly provides the possibility

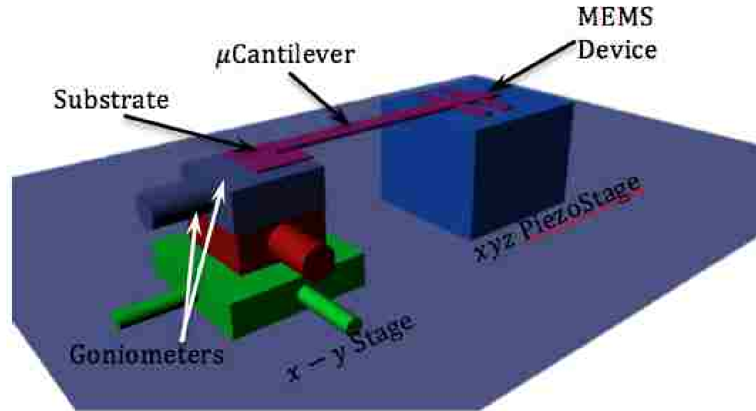

Figure 3.4: Schematic illustration of the custom made stage and the experimental setup. The MEMS device is fixed on the piezo stage with $1nm$ accuracy in $x, y\&z$ directions. The Poly-Si substrate is fixed on the stacked set of manual stages including $x\&y$ micro positioners with $1\mu m$ and two goniometers with 8^{sec} resolution

of fine adjustments before stiction failure is accomplished as well as highly controlled peeling of the μcantilever off the substrate. Peeling is done by slowly moving the MEMS device transversally away from the substrate, fixed on the goniometer, in the direction of its shuttle. To achieve higher quality stiction, the μcantilever should be the positioned $2 - 3\mu m$ above the substrate such that no more than $155\mu m$ of its length overlaps the substrate. A droplet of liquid DI water is then used to wet the substrate and the μcantilever. The hydrophilic Poly-Si immediately sucks the water into the gap between μcantilever and the substrate. Once the μcantilever is soaked in water it is lowered to zero height from the substrate using the piezo stage. As the water dries, capillary forces and the considerable negative pressure produced under the μcantilever, pull the overlapping part of the μcantilever beam, tightly, onto the substrate causing a high quality adhesion referred to as stiction failure.

It is important to remember that the critical strain energy release rate is independent of the adhered length of the μcantilever but the fore needed to initiate slippage is not. It was observed that the tensile stresses developed inside the μcantilever can

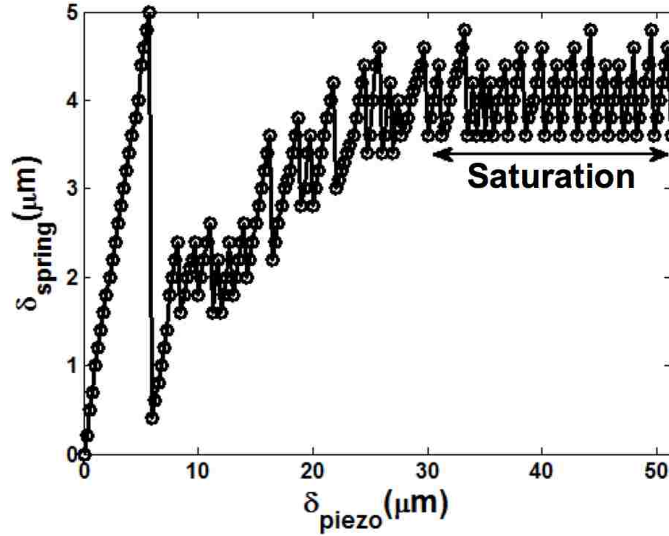

Figure 3.5: As long as the stiction failed μcantilever does not slip, the deflection of the flexural arms will be equal to the total displacement of the piezo stage. Once the μcantilever starts to slip the magnitude of slip will be equal to the difference of the piezo stage displacement and deflection of the flexural springs.

get large enough to actually break the experimental sample or damage the MEMS device if a much longer part of the μcantilever is stiction failed on the substrate.

After complete evaporation of the DI water, the piezo stage is used to horizontally pull the MEMS actuator away from the substrate in $250nm$ increments. Since a considerable portion of the μcantilever is stuck on the substrate the flexural elements of the MEMS device deform as the base of the device is pulled away.

3.4 Experimental results

The raw data obtained directly from the mode II peel test experiments performed are the different displacement information. The specific information needed are the flexural arm deflection data of the MEMS device and the slippage data of the stiction

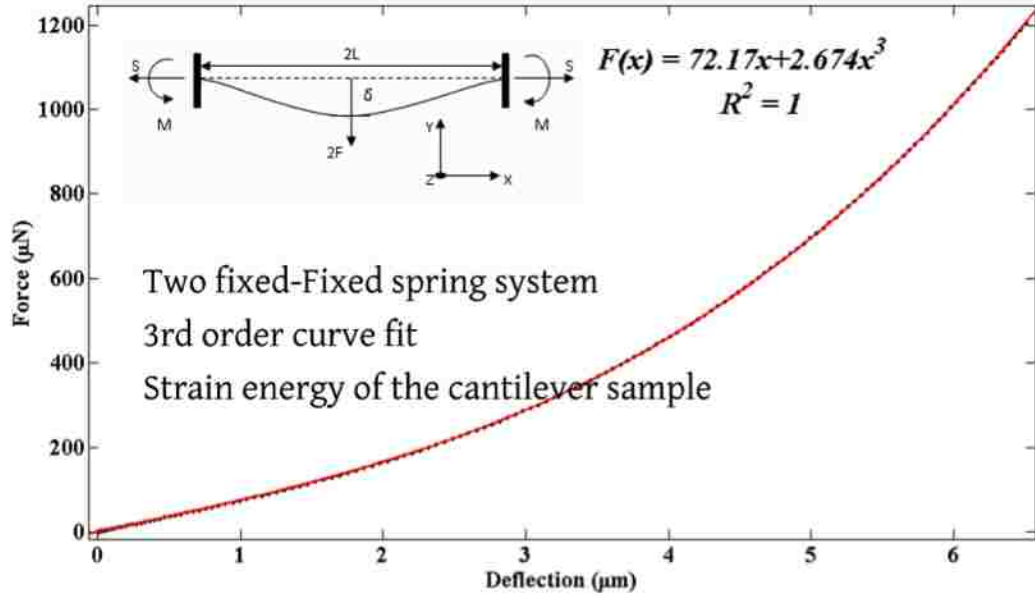

Figure 3.6: The force-diffiection relationship of a Si fixed-fixed beam with the specifications used here, obtained using Frisch-Fay model. A third order polynomial of the form $F = k_1x + k_3x^3$ can be used to estimate this specific relationship with considerable accuracy.

failed μcantilever. The deflection of the MEMS device arms can be directly read from the vernier structure at every loading step. The slippage of the μcantilever can be obtained by subtracting the vernier value from the total displacement of the piezo stage carrying MEMS device. Figure 3.5 shows how the deflection of flexural arms change as the piezo stage continues moving away horizontally. As will be seen soon the deflection data will be used to determine the pulling force transmitted to the stiction-failed μcantilever through the MEMS device.

3.5 Force

The legs of the MEMS load cell shown in Figures 3.2 & 3.3 are treated as two fixed-fixed beams each with a spring constant of $\frac{192EI}{L^3}$, where E, I and L represent the

Young modulus of elasticity for Si, the second moment of inertia and Length of the beams respectively. But the linear force-deflection relationship holds only in small deflection ranges, not grater than $\frac{1}{4}$ of the μcantilever's thickness, for the fixed-fixed beam configurations of Figure 3.3. This corresponds to only $575nm$ in our case. Since the experiments performed here far pass this limit a more sophisticated model is needed to describe the force-deflection behavior of the device used.

Frisch-Fay introduced the nonlinear force deflection relationship for a fixed-fixed beam but the solution of proposed relationship involves iterative simultaneous solution of two coupled nonlinear equations [40, 138]. In order to be able to calculate the Force in realtime a faster but as accurate method is highly preferable. For convenience after solving Frisch-Fay's model for the system used here and obtaining the force-deflection relationship, the authors realized that a third order polynomial can be used to estimate the force values of the fixed-fixed springs system used here, highly accurately. Figure 3.6 shows the results of Frisch-Fay model as well as the third order polynomial model.

The total force applied on the μcantilever is twice the force of a single fixed-fixed beam spring. Using the nonlinear Frisch-Fay model and the obtained third order polynomial fit of Figure 3.6 the total force on the stiction failed μcantilever sample is calculated for different locations of the piezo stage. These data are represented in Figure 3.7.

3.6 Elastic stored energy

Both the μcantilever beam and MEMS load cell are created from Si, a linear elastic material. Therefore, each of these constituents and their components can be treated as a combination of flexible elements. The specific configuration of Figure 3.2 means that all of these elastic elements are in series configuration. Unlike the fixed-fixed

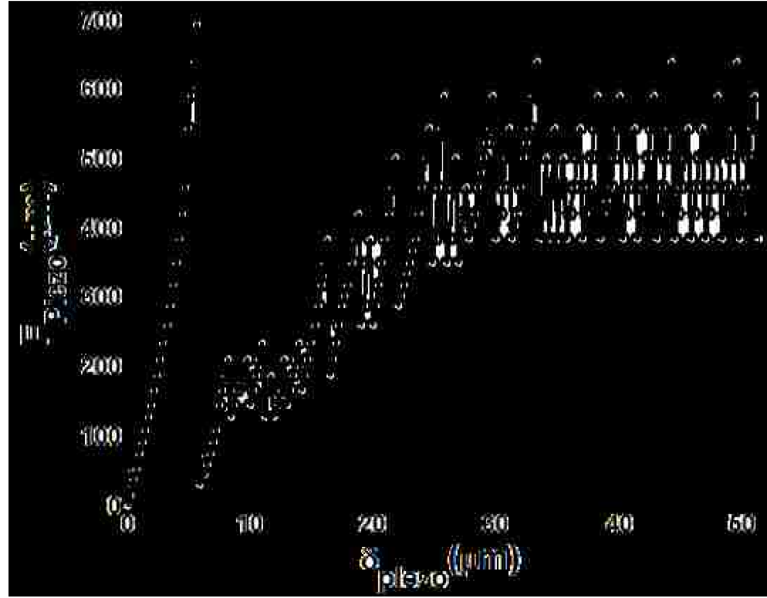

Figure 3.7: The total longitudinal force acting on the stiction failed μcantilever as a function of the piezo stage displacement.

beam springs which are under transverse loading, the shuttle and the unstuck portion of the μcantilever are under longitudinal tension. The later two elements have an overall elastic coefficient of $\frac{1}{k} = \frac{L_s}{A_s E_s} + \frac{L_c}{A_c E_c}$. In this relationship the index "s" components are for the shuttle and the index "c" components refer to the μcantilever. A,E, and L represent the cross-sectional area, modulus of elasticity and the length of the components respectively.

As the flexible components of the assembled system of Figure 3.3 deform, they store elastic energy. But considering the specifications of different components, it is seen that the shuttle and the unstuck portion of the μcantilever are more than 2,000 times less flexible than the fixed-fixed beam spring system and can be considered to behave rigid for the purposes of this chapter, without inducing noticeable error. This also means that the total elastic energy can be considered to be stored in the fixed-fixed beam systems only.

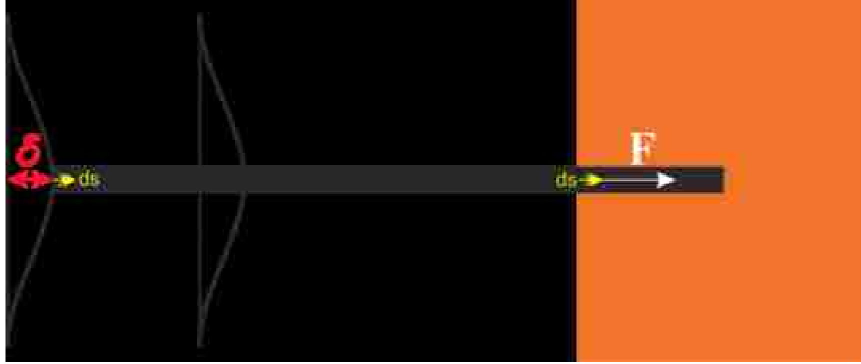

Figure 3.8: Schematic representation of the fixed-fixed spring system deflection

The work done by the external force on the MEMS system is stored elastically in the fixed-fixed spring system. Since the device is always in static equilibrium situation the external force is always in balance with and equal to the spring reaction force. In order to calculate the elastic energy stored in the system, one needs to integrate the infinitesimal work of external force, F_{ext}, over the shuttle displacement, δ, (see Figure 3.8). Using the third order polynomial fit of the fixed-fixed beam system's force, this can be accomplished as shown in (3.1).

$$U = 2 * \int_0^\delta (k_1 x + k_3 x^3) d\delta = k_1 x^2 + \frac{1}{2} k_3 x^4 \tag{3.1}$$

3.7 Adhesion energy and Mode II critical strain energy release rate

Strain energy release rate is conceptually defined as the energy associated with the creation of two new surface areas from a bulk material. This concept is widely used in fracture mechanics to define the critical situation that crack will propagate inside a material. The crack propagation is usually studied in either of two situations. Whether crack propagation under constant force or under constant crack tip

deflection. The case studied in this paper is the later one. The MEMS device is quasi-statically moved away from the substrate to allow a crack propagate between the μcantilever and the substrate. As the MEMS actuator device is pulled away from the substrate, which the μcantilever is failed on, the spring system starts to deflect and store energy.

Mathematically, strain energy release rate is defined as the differentiation of the stored elastic strain energy with respect to the new surface area created under constant crack tip height(deflection). For this report this means that if the μcantilever slides on the surface an infinitesimal amount δx creating two new surface areas equal to $A_{created} = w\delta x$, leading to a reduction on the strain energy stored in the system equal to $-\delta U$, the strain energy release rate would be $G = -\frac{\partial U}{\partial A}$, where δA represents the new surface area created. But as explained by Griffith [38, 63], for every material, there is a critical strain energy release rate that must by reached before two new surfaces can be created from the original piece of material, in our case being the creation of new surfaces due to slippage of the μcantilever on the substrate it has failed on. The strain energy release rate for the system used here can be obtained using (3.2). In this equation L_f is free length of the μcantilever.

$$G = -\frac{1}{w}\frac{\partial U}{\partial L_f} \tag{3.2}$$

Experimentally, controlled crack growth through the interface is accomplished by raising the MEMS device (and consequently the unstuck end of the μcantilever) slightly above the independent substrate (and the stuck end of the μcantilever) and then indexing the independent substrate away from the MEMS actuator. Inducing this slight deflection in the unstuck portion of the μcantilever ensures the formation of at least two light interference fringes on it. This is only an experimental measure though. The sudden motion of these fringes are used for signaling the crack arrests. For the experiments reported here, the unstuck length of the μcantilever is more than $1000\mu m$ while the induced deflection is only $525nm$, low enough to accurately

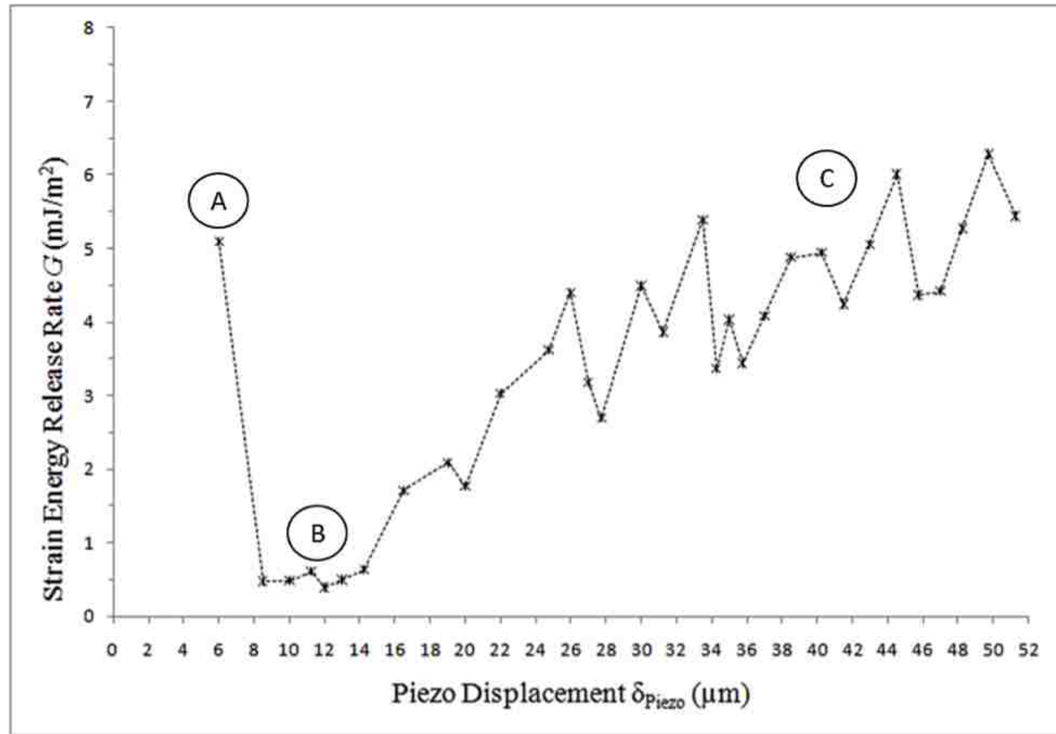

Figure 3.9: The critical strain energy release rate values for Mode II crack propagation in poly-Si - poly-Si interface.

consider the experiments of chapter 1 pure more II experiments. The critical strain energy release rate for the Mode II crack propagation of Poly-Si μcantilevers on Poly-Si substrate obtained from these experiments are shown in Figure 3.9

3.8 Discussions

3.8.1 Static friction force

As observed in Figure 3.5, the displacement of the MEMS actuator tracks the displacement of the piezo, indicating that the surfaces are stuck together. After displacing the MEMS actuator $\sim 5\mu m$, the μcantilever incurs a slippage and the MEMS

actuator's deflection decreases correspondingly, but does not return to zero. This constitutes, one "stick-slip" event. The maximum force(see Figure 3.7) during the sticking phase is the static friction force, F_s. Further increments of the piezo cause the MEMS actuator to track the piezo displacements again until another sliding occurs. This trend continues throughout the experiment. As seen in Figure 3.7, F_s drops considerably after the first slip but then continues to increase in the subsequent stick-slip cycles. It is also observed from Figure 3.5 that after the occurrence of a number of stick-slip cycles (∼13) the intermediate relative position, where the μcantilever re-sticks to the substrate is saturated and never falls below this saturation deflection of the fixed-fixed spring of the force measurement device.

Amonton's law states that the friction force is directly proportional to the applied normal load, through a constant of proportionality (i.e. the friction coefficient) which is independent of the contact area and the sliding velocity but a function of the surface roughness. The force required to initiate sliding is known as static friction force. This force can be written as $f_s = \mu_s N$, where μ_s is the coefficient of static friction and N is the normal force acting due to bonding of the two surfaces. By using a coefficient of friction value of 0.35 [33], the normal force acting due to bonding is found to be approximately $2mN$.The lateral force applied is equal to the static friction force when the cantilever beam starts sliding on the substrate.

3.8.2 Surface Roughness

In this section the surface roughness of the μcantilever sample and the independent substrate are measured. Two sets of measurements are performed for every surface. The first set is done on virgin surfaces before the stiction failure. The second set measures the roughness values of the surfaces after the stiction failure experiments. Figure 3.10 shows AFM results of the surface asperities of the μcantilever sample

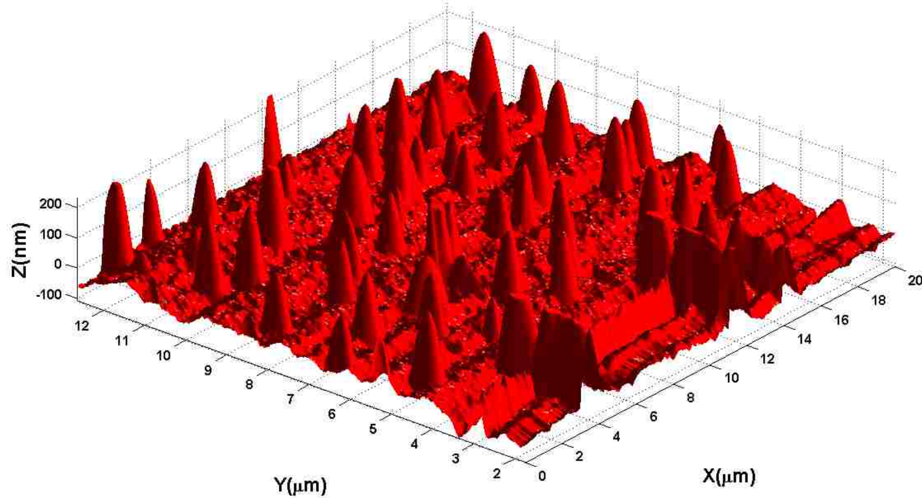

Figure 3.10: Schematic showing the various regions that are characterized

before the stiction failure experiment. Figure 3.11 shows AFM results of the same sample after stiction failure experiment. The RMS roughness of the undisturbed μcantilever surface is found to be 24.949nm but it increases to 63.992nm after the experiment. The μcantilever sample is made using the Poly1 mechanical layer of SUMMiT V. The independent substrate used here had an RMS roughness of 3.925nm before the experiment, which increased to a slightly higher value of 4.180nm after the experiment. This substrate is made from the Poly0 mechanical layer of SUMMiT V which in general is smoother than the other layers.

It was observed that in general the stiction failure test and multiple stick-slip cycles tend to increase the roughness of the surfaces involved. The higher increase in roughness observed in the μcantilever is because of its deposition and processing history. The AFM results of Figure 3.10 show slender stalagmite-like cones distributed on a relatively smoother base. After the experiment these get replaced by a more compact distribution of chunkier cones, which are chopped somewhere along their height. We believe that as the μcantilever is rubbed on the substrate during the

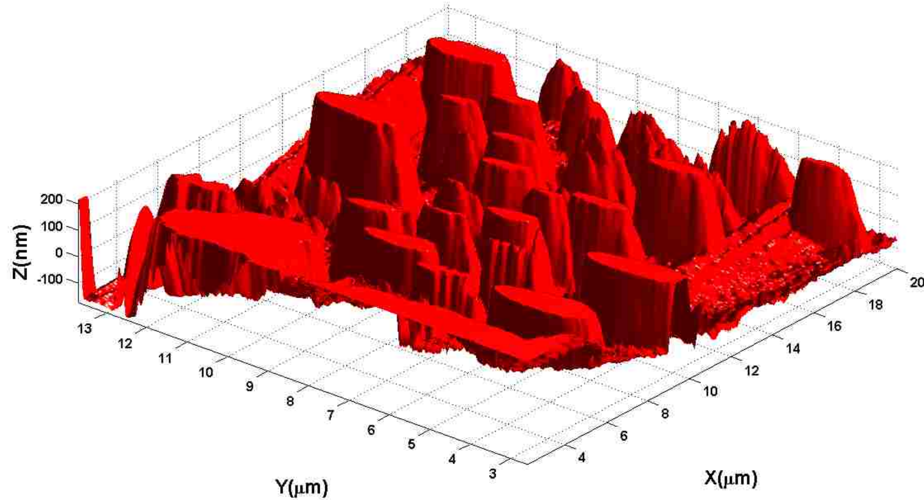

Figure 3.11: Schematic showing the various regions that are characterized

experiment, slender cones brake off and fall into the valleys, after absorbing some smaller debris and growing in diameter as they roll between the two surfaces. This process is schematically illustrated in Figure 3.12

3.8.3 Critical strain energy release rate

As in Figure 3.9 the critical strain energy release can be divided into stages. Although not even comparable to bulk silicon, G_{II} is considerably high at the first cycle. This is not limited to this experiment. This phenomenon was observed in the Mode I experiments as well. The reason lies in the method used to make the stiction failure happen to start with. The initial stiction is facilitated by a liquid, wether DI water or Isopropyl alcohol (IPA). The considerably large negative Laplace pressure inside the liquid pulls the surfaces together. The Laplace force increases considerably as the liquid drys and can reach a couple of MPa as we will see in the next chapter. This large negative pressure presses the surfaces together, locking their asperities in

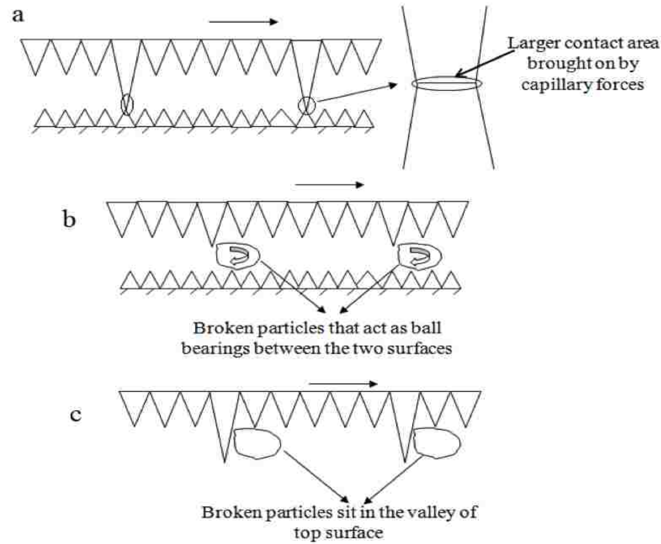

Figure 3.12: An example of two rough surfaces in contact, (a) Larger contact area brought on by capillary forces (b) An image where broken particles acting as ball bearings between the two rough surfaces (c) An image where the broken particles sit in the valley of top rough surface

each other. As the liquid dries an other interesting phenomenon happens too. The drying liquid sucks the debris in, cementing the surfaces together.

Not only all these bonds are broken off, after the first slip, but some of the asperities break off and fall into the gap between the μcantilever and the "independent substrate". These broken cone shaped asperities roll as bearings between the surfaces, reducing the critical strain energy considerably in the stick-slip cycles to come. These cycles and their G_{II} values are the group "B" of Figure 3.9.

As the experiment continues the broken pieces fall into the valleys between the surface roughnesses and the adhesion quality between the surfaces start to increase gradually as the "bearing" disappear and the surface roughnesses increase. We also believe since condensation happens at any temperature and is a function of gap radii, as the roughness increases, lots of tiny gaps between broken pieces and the surfaces

involved start to appear where water condenses. The combination of the condensed water and increased mechanical interlocking due to roughness increase leads to a gradual increase in G_{II} value as seen in part "C" of Figure 3.9.

3.9 Conclusions

This work presents a novel technique to determine the Mode II interfacial adhesion energies. It is important to note that for the first time we developed an experimental method with which we can measure the interfacial energies from Mode II type failures. Separate new theories and experiments are developed to measure the upper bounds of G_{II} and also to determine a G_{II} value accurately. We measured the upper bounds of G_{II} as an average of $G_{II} \leq 4.387mJ/m2$. And with the infinitesimal crack growth experiment, the accurate value of G_{II} is measured as $0.932mJ/m2$. This value for Mode II is in-line for the mixed mode measurements made in sections previous to the Mode II experiments. The contribution of Mode II cannot be ignored in what is seemingly a Mode I type failure. This is attributed to the type of bonding between surface and roughness. As the surface roughness plays an important role in the adhesion of MEMS structures, the surfaces that were involved in the experiments are characterized with Atomic Force Microscopy (AFM). It is observed that the surface roughness of an experimentally disturbed Poly1 rubbed surface of μcantilever beam has more RMS roughness compared to a virgin Poly1 lower surface of μcantilever beam. The high value is reported as $63.992nm$ and its counterpart as $24.949nm$. From the surface of μcantilever characterization, we conclude that the peaks broke off are sitting in the valley of the bottom surface of the μcantilever beam is the cause for a high RMS roughness value. At the same time, it is noticed that the surface roughness of an experimentally disturbed Poly0 surface of the substrate did not change when compared to the virgin Poly0 surface of the substrate. The RMS

roughness of the substrate is found to be around $4nm$.

The critical strain energy release rate is found to be highly sensitive to crack height and crack length values ($G_{cr} \propto \frac{h^4}{s^6}$). The highly sensitive experiments of Chapters 2 and 3 would not be possible with out a three dimensional microscopy system which would enable highly accurate measurements of the out of plane deformations imposed on the μcantilever samples as well as their in plane motions. The Michelson Interferometer described in the next chapter is designed and built as a part of this work to enable accurate measurements required. This microscope is also capable of determining the dynamic motion of MEMS and NEMS up to $1.25MHz$ as will be explained.

Chapter 4

Dynamic 3-D Microscopy Using A Michelson Interferometer

4.1 Introduction

Interferometry is a technique, which uses patterns(also knows as "fringes") obtained by interference of two beams of light (or any other types of waves) to measure out-of-plane shape / deformation of objects. Based on their relative phase, two waves can interfere constructively or destructively. Constructive interference causes an increase in the intensity of the light (white fringes) and destructive interference causes a decrease in the intensity (dark fringes). An interferogram is an image of these interference patterns and it looks as strips of dark and white regions that can span across the image.

Interferometry can also be viewed as a method of encoding that encrypts the three dimensional information on a two dimensional image. One commercial application of this is in holograms[47, 36]. The image seen when looking at a properly illuminated hologram changes as the position and orientation of the viewing system changes

making the image appear three dimensional. The holographic recording itself is not actually an image though. It is made as structures of either varying intensity, density or profile which have no resemblance to the actual image.

Different techniques have evolved from the basic idea of using interference of waves to measure the out-of-plane height. Based on the frequencies of interfering waves being similar or different these methods can be divided into two main classes, i.e homodyne or heterodyne. Some examples include Fabry Perot, Mach Zehnder, Fizeau and Michelson Interferometers. The method used in this dissertaion is the latter one.

The basics of operation of a Michelson interferometer are relatively simple. The light path in a Michelson interferometer is illustrated in Figure 4.1. A collimated beam of light is divided into two identical beams, which combine again after reflecting back from the sample and the reference mirror, creating an interferogram at the CCD camera. Figure 4.2 shows two interferograms with multiple the dark and bright fringes.

In interferometry and holography, the out-of-plane height information are coded as phase difference between the incident waves. Theoretically, there is no height range limit for this method as long as it is less than the coherence length of the light used and within the focal length of the imaging system but phase data obtained with this method are wrapped into $[-\pi, \pi]$ range. This means there is no one-to-one relationship between phase and height which makes decryption(unwrapping) of the phase and getting the height data mathematically challenging and sometimes impossible. It also means that unlike the height information, the phase information stored in the fringes is not continuous but rather in the form of discontinuous strips of information(see Figure 4.12).

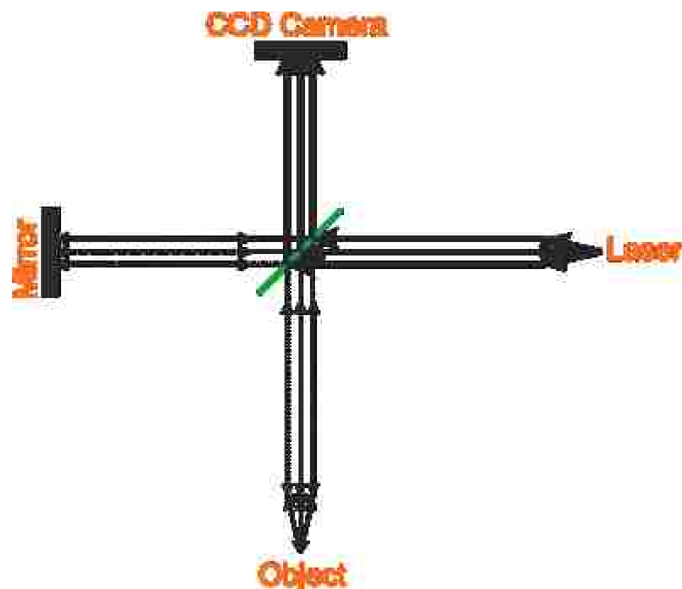

Figure 4.1: Basic light path diagram of a Michelson interferometer.

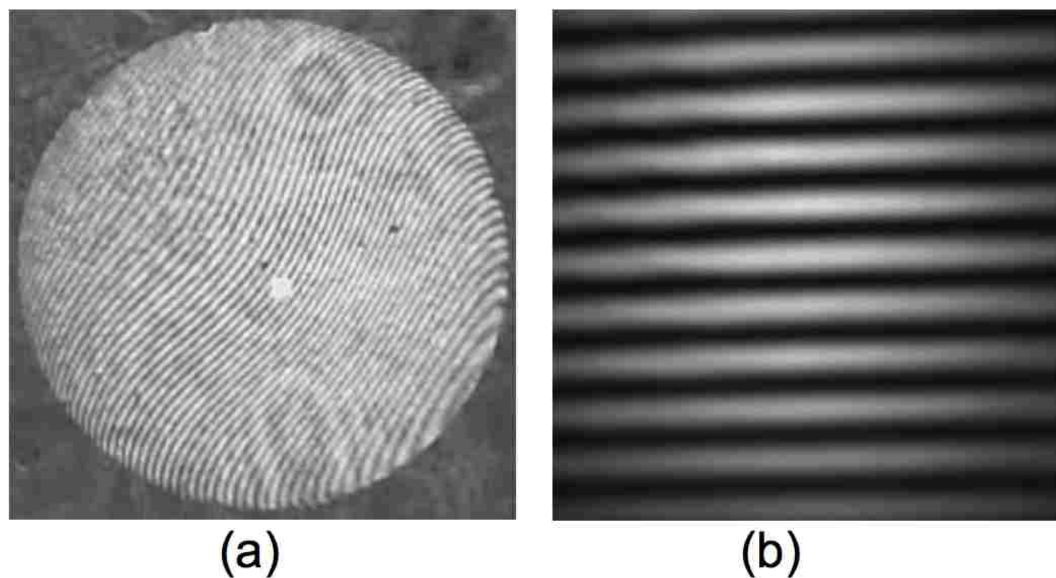

Figure 4.2: Comparison of two interferograms. (a) A more common quality picture obtained by interferometry [131] (b) The interferograms obtained by the fabricated microscope in this project. The image is before any enhancement.

4.2 Effect of Light Used in Interferometry

The light used for interferometry has deterministic effect in image quality, fringe formation, fringe contrast and height range covered per fringe. Michelson interferometry is highly sensitive to wave front quality and any patterns in the wave front can considerably reduce the image quality and add noise to the image. Other main factors decreasing the interferogram contrast are unwanted mechanical vibrations transmitted to the microscope and air density changes due to air flow.

4.2.1 Wavelength of Light

Considerable care should be taken when selecting the wavelength of the light to be used. The samples should not be transparent to the wavelength selected. The devices used in this dissertation were mainly Poly-Si MEMS with thickness values ranging from 10's of nanometers to a couple of micro meters. The reflectivity of silicon increases as the wave length decrease [44]. It was observed that the samples were actually partially transparent to red light (wave length of $637nm$) but not for green light.

4.2.2 Coherence Versus Natural Light

In order for the interference patterns to form, light should be coherent, meaning the phase difference between interfering waves should be a function of the path length difference between them. There are two types of coherence associated with light, i.e. temporal and spatial. temporal coherence is a measure of the longitudinal distance over which phase is conserved. Spatial coherence measures the coherence of light over the beam cross section. For engineering purposes, temporal coherence can be considered to control the formation of fringes while spatial coherence controls the

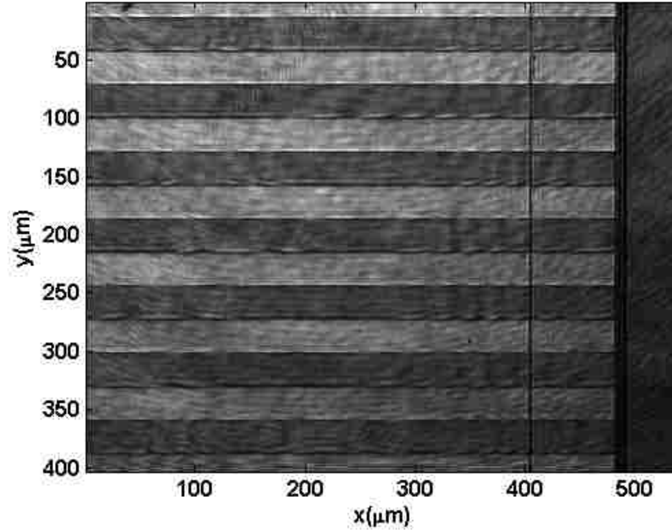

Figure 4.3: Image of a μcantilever array obtained with no fringes. In order to eliminate fringes the light from reference mirror is prevented to interfer with the light from sample.

contrast of in different areas of the image.

Natural light has an temporal coherence length of less than $\sim 5\mu m$ and low spatial coherence. This makes the formation of interference patterns considerably difficult and puts a barrier on their contrast. In order to produce interference patterns using natural light, the path length of the interfering beams should be matched with less than $\sim 5\mu m$ accuracy. This also considerably limits the measurable height range on a sample.

The usual temporal coherence lengths for lasers on the other hand, can range from a couple of meters to a couple of kilometers. This means it is easy to get interference fringes to start with and because lasers in general have higher spatial coherence, the fringes will also have considerably higher contrast compared to natural light. The large coherence lengths of lasers also mean that large out-of-plane deformations can be measured relatively easily.

It seems that the superior properties of lasers make them the optimal choice when it comes to interferometry. However, their longer temporal coherence length can also cause problems. A long coherence length means that the light has a longer 'memory' to itself carrying the diffraction effects due to the dust particles and debris on the optics, for a longer distance. This can considerably reduce the quality of the final image. Despite all the effort to keep optics as clean as possible it is not possible to have absolutely no dust at all. The diffraction of light from the small debris results in concentric circular rings clearly visible in the final image.

4.2.3 Polarization

Light polarization is another main characteristic of light to be considered when working with lasers. In order for the interference patterns to form, the two incident beams should have similar polarization. Not having the same polarization can reduce or even completely ruin the fringe contrast. In order to prevent any issues related with polarization it is highly recommended to use polarization nonsensitive optics.

4.2.4 Light Source Used

Because of safety concerns about shorter wave lengths, a coherent, non-polarized green light with a wave length of $520nm$ was selected as the light source. For proper operation, the diode is kept at 25^oC using the PID temperature controller, visible in the lower left corner of Figure 4.4. The current controller unit controls the diode current based on a voltage input signal generated by an Agilent function generator, which in turn is controlled by a software developed in LabVIEW. Modulation signals slower than $200kHz$ should be connected to the laser diode driver(the current controller) but signals of $200kHz - 500MHz$ can be connected to the diode mount directly.

The $20mW$, $LP520 - SF15$ pigtailed laser diode is purchased from Thorlabs Inc [123] and is modulatable up to $100MHz$. Being equipped with a single mode optical fiber not only has the advantage of providing flexibility in transferring the light produced by the diode to the main structure of the microscope and aligning it properly but it also removes extra modes present in the light coming off the diode. This eliminates any interference patterns that may exist as a result of interference of existing different modes of light.

Figure 4.3 shows a sample of the high quality images obtained. This image is obtained using the light reflecting from the sample only (the light from reference mirror was blocked to prevent interference).

4.3 Hardware Setup

The basic setup of a Michelson interferometer is pretty simple and it is not difficult to make one's own basic interferometer by using some simple optics. The basic setup is composed of a light source, a beam-splitter, a reference mirror, two microscope objectives and a CCD-camera. The input light is split into two identical perpendicular beams, (see Figure 4.1), which travel along the reference arm and sample arm and reflect back from the reference mirror and the MEMS μcantilever sample. The reflected beams are added together and interferer before reaching the camera. The two beams reflected from the mirror and the sample, have traveled different distances and have different phase angles. The difference in the phase angles can lead to constructive or destructive addition of the two waves at different points across the beam.

Making an interferometer capable of measuring the three dimensional vibrations of MEMS or phononic crystals whose critical dimensions can be comparable to the diffraction limit of light and their out of plane shape and vibrations amplitudes

range from a couple of nanometers to a couple of micrometers at most, however, is a difficult challenge. In theory, addition of two waves should result in an interferogram with a high contrast but in reality most interferograms lack the required resolution and contrast to begin with,(see Figure 4.2a). Different image processing techniques can be used to enhance the obtained image to some extent. But in order to a get a high resolution and trustable data the original interferogram is required to have considerable contrast and sharpness. Figure 4.2b shows an original interferogram obtained by the Michelson interferometer designed and erected here before any post processing or noise reduction. Figure 4.2 also compares this interferogram with some other interferograms found elsewhere.

In order to create an upright microscope which could be easily used for horizontal samples while providing enough free space underneath for a custom made stage and fixture, the cage system offered by Thorlabs Inc [123] was used. This cage system provides a means of creating complicated optical systems with considerable accuracy and mechanical stability. The cage compatible optical components, tip-tilt controls, micro-positioners and so on provide means of accurately and stability alining the optics. Figure 4.4 shows the interferometer microscope built as a part of this dissertation. The main components are:

1. A Laser diode equipped with appropriate temperature and current controllers.
2. Collimation unit
3. A pellicle beam-splitter
4. Reference arm
5. Object arm
6. A CCD camera with external triggering and shutter timing control capabilities

7. Function generators required to produce the three control signals

8. The software developed in LabVIEW for controlling the function generators and the National Instrument PCI board

9. The software developed in MATLAB for image acquisition and data post processing

10. Two workstations to run the LabVIEW and MATLAB codes

All optical components, whether specifically mentioned or not, are installed in the cage system using mounts that have all the necessary degrees of freedom required to align and position them with high resolution. The custom made stage visible in center-bottom of Figure 4.4, is equipped with coarse and fine x,y and z micro positioners as well as tip-tilt controls. This makes it possible to position the sample properly and align it with the focal plane of the microscope.

The novelty of the Interferometer of Figure 4.4 is that it can generate very high quality interferograms and obtain all the information required to accurately reconstruct the three dimensional shape of the sample from it, eliminate need for mechanical motion of its components. Extracting phase information is done using Fourier analysis of the interferogram. It takes considerable numerical analysis to unwrap the phase information and reconstruct the 3D shape of the sample but the software developed to run the microscope provides almost realtime $3-D$ image reconstruction.

The structure of the of the microscope built (see Figure 4.4) follows the illustration of Figure 4.1 closely. The four arms of the microscope are perpendicular to each other and are positioned around the central beam splitter. The different components and their applications are explained in more details below.

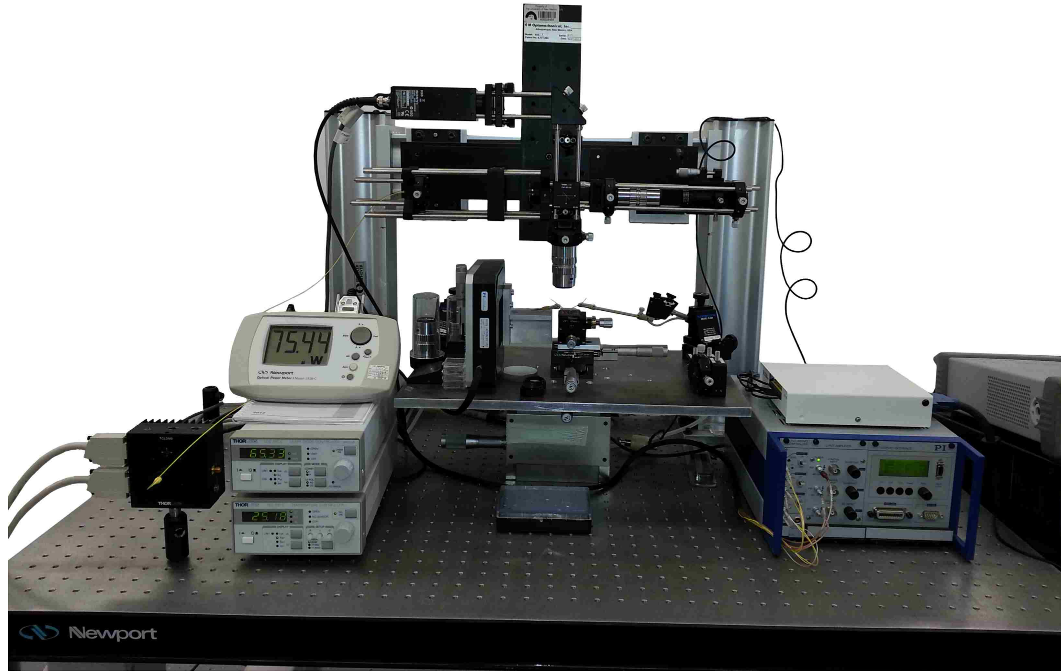

Figure 4.4: The finished interferometer microscope. Light generation unit is located in bottom left and is composed of laser source a temperature controller and a current controllers which feed the light into the yellow optical cable. The main body of the microscope is displayed in the center. The piezo controller in the lower left combined with the signal generation PCI board composes the actuation unit. The figure also shows the custom made stage made for proper positioning and aligning of samples.

4.3.1 Collimation Arm

The light diffracting from the pinhole is collimated to a diameter of ~ 2". The light intensity was verified to have a gaussian profile. A 2" achromatic plano-convex lens is used for collimation. Expanding the beam to ~ 2" and then using only the central 0.5" of it, resulted in an almost flat top beam. This led to almost constant brightness across the image.

4.3.2 Sample Arm

The sample arm uses a long distance microscope objective purchased from Edmond Optics to focus the light on the MEMS sample. The microscope objective is installed in the cage using an x, y micro-positioners stage. A separate custom made $x, y, z, \theta_x, \theta_y$ stage makes it possible to bring the sample in focus and move it in all three direction as well as controlling its tip/tilt angles.

4.3.3 Reference Arm

The reference arm has an objective similar to that of the sample arm, to focus the light on the reference mirror. The objective was installed in the cage using a x, y, z stage which not only allowed in plane adjustments but also focusing of the objective. The reference dielectric mirror with $\frac{\lambda}{4}$ roughness has tip/tilt as well as x, y control. The tip/tilt control is used to control the number of fringes in the image. Almost no separate fringes should be distinguishable if the mirror is completely perpendicular to the completely flat flat sample (only a mirror used as the sample).

4.3.4 Camera Arm

The reflected light beams are directed to a CCD camera after they interfere (using a 45° mirror). A lens is used to create focus the image at the CCD. The camera shutter is controllable with a resolution of than 10^{-5} seconds and it can capture up to 15 frames per second.

4.3.5 Ghost Image Elimination

Ghost images are are among the main sources of noise in most Michelson interferometers. They introduce unwanted patterns on top of the main fringes. The situation can get very serious when imaging with coherent light, since the ghost beams interfere with each other and with the main beams, causing secondary and tertiary fringes.

Ghost beams result from unwanted internal reflections off of different optical elements. Anti-reflection coatings considerably eliminate ghost beams in most of optical elements but not very successful in prismatic beam-splitters. Figure 4.5 illustrates the two ghost beams from a prismatic beam-splitter (despite the antireflection coating) and their relative measured intensities as well as the resulting secondary fringes. It also compares the light-path and fringe quality for a prismatic beam-splitter and a pellicle beam-splitter. The percentages shown on the illustrations of Figure 4.5 represent the measured relative power values.

The small spacing between prisms of prismatic beam splitters is caused by the adhesives and does not exceed a couple of micrometers. But even this is too big of a gap compared to the nanometer vibration amplitudes to be measured.

A pellicle beam-splitter is a thin membrane (a couple of micrometers in thickness), which is semi transparent to some wavelengths. These beam splitters are very fragile but currently the best solution. As shown in Figure 4.5 using a pellicle beam-splitter improves the quality of fringes considerably by eliminating the main ghost beams that were present when using the prismatic beam splitter.

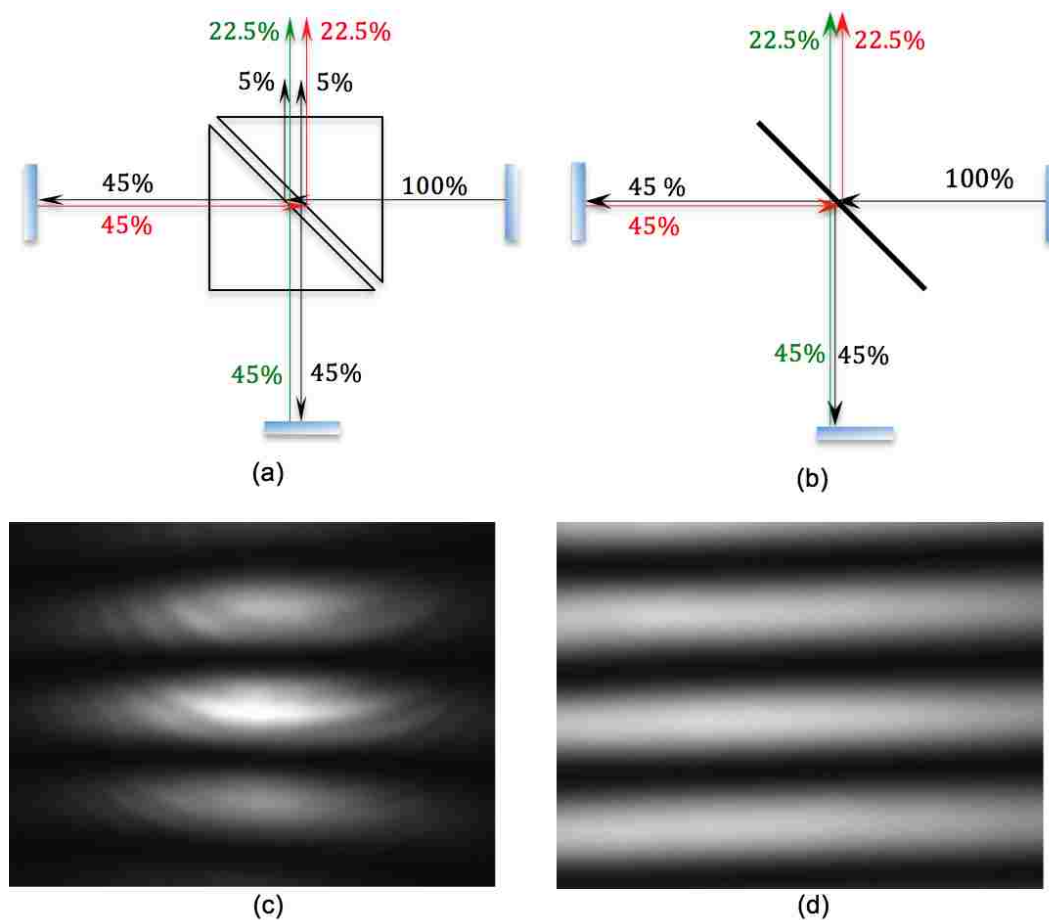

Figure 4.5: Comparison of the ghost images resulted from different beam-splitters. The percentage values are with respect to the source beam intensity. (a) Schematic of a prismatic beam-splitter composed of two aligned prisms with a short distance between them. (b) Schematic of the light path in a pellicle beam splitter. (c) The resultant fringe patterns from a prismatic beam splitter shows the secondary fringes superimposed on the original horizontal fringes. The secondary fringes are the interference result of the two ghost image beams. (d) The fringe pattern obtained by a pellicle beam splitter is very smooth and free of any secondary fringes.

4.3.6 Controllers

The laser diode is equipped with appropriate temperature and current controllers. The current controller used can modulate the diode up to $200kHz$. The mount used

for the diode can modulate the laser in the range of $200kHz - 500MHz$ using an RF input signal. The signals required to actuate the MEMS device, control the laser and trigger the camera are generated by Agilent function generators (Agilent 33250A & Agilent 33510B). Since the maximum voltage of the signal generated in the function generator is limited to $20V$ peak to peak, an amplifier is used to amplify this signal to be able to actuate the MEMS device. it was observed that in order to induce any noticeable vibrations at low frequencies a minimum of $50Vpp$ is required. Care must be taken since electrical arcing can happen at around $60Vpp$.

4.4 Modes of operation

To the best of our knowledge, all Michelson interferometers work in either Phase shifting or vertical scanning modes. Both of these operation modes require a highly accurately controlled mechanical motion of microscope elements, which results in motion of the fringes in the image plane. The series of the images which capture the motion of fringes, are then used to obtain the relative phase information of adjacent pixels. The need for accurately controlled mechanical motion of the reference mirror or the sample limits the applications of phase shifting and vertical scanning interferometers to static and quasi-static situations.

The Michelson interferometer microscope developed as a part of this dissertation is neither vertical scanning nor phase shifting. Using a coherent light source and benefiting the high spatial coherence of the laser helped overcome the low contrast issues of conventional interferometers and enabled us to get high quality phase information using only a single interferogram eliminating the need for multiple images required in PSI and VSI methods.

This microscope can operate both in Static mode and Dynamic modes. Static mode is designed for stationary samples, free of any vibrations. This mode can

be used to get high quality surface roughness data as well as to detect any initial deformations due to residual stresses. The dynamic mode is more complicated and a novelty in the field. It combines spectroscopy with interferometry and benefits the new design of the microscope to capture the shape of harmonic vibrations of MEMS, oscillating at high frequencies (up to $3MHz$ tested successfully). The operation mode is detected automatically based on the external trigger received by the camera. The dynamic operation capability is achieved by two methods:

- The first mode can capture transient vibrations of samples vibrating at low frequencies. The CCD Camera used can capture up to 15 frames per second but the camera shutter can be controlled as short as $10\mu sec$. Considering the limitations of the current hardware this mode of operation can currently capture transient vibrations up to $15Hz$ and harmonic vibrations up to $10kHz$. Replacing the current CCD with a high speed camera enables the microscope to record transient vibrations at very high frequencies. The software developed to run the microscope can automatically detect the new camera and use it.
- The second mode is based on spectroscopy combined with interferometry. This mode does not require a high speed camera but it requires the ability to modulate the light source at least 50 times faster than the maximum target frequency. The different signals used to trigger the camera, vibrate the MEMS device and modulate the light source intensity are illustrated in Figure 4.6. Since light illuminates the sample only for a fraction of its oscillation period, in spectroscopy, the shutter is open for longer periods of time to receive enough light for capturing every single frame. In the current setup, the laser diode used can be modulated up to $150MHz$ enabling the microscope to capture the 3-D harmonic vibrations of up to $3MHz$.

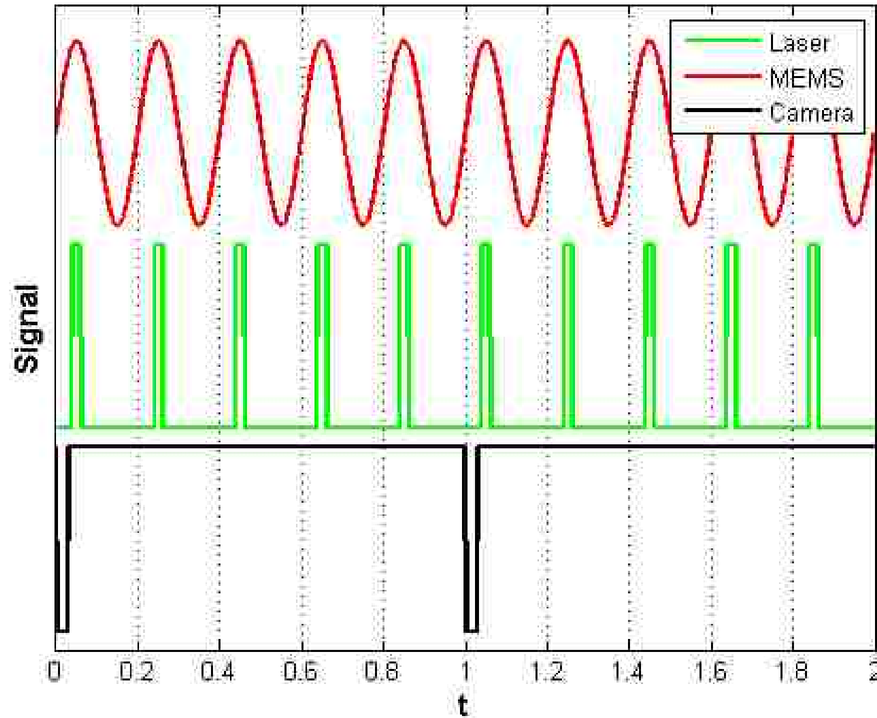

Figure 4.6: Different signals used in spectroscopy. In this example of spectrosopy camera is set to capture images at $1Hz$ and the MEMS sample is vibrating harmonically at $5Hz$. The laser illuminates the sample at the same frequency as its vibration but only for a very short time during every oscilation. This figure also shows that there is 90° phase difference between the laser and the MEMS.

4.5 Capturing Complete Vibration Profile and Mode Shapes

In order to not only see the deformed shape but to capture the complete vibration profile or mode shape of a harmonically vibrating sample, using the dynamic operation mode, one needs to change the phase of the light (see Figure 4.6) with respect to the MEMS device, in every new frame captured, to cover the complete $[0 - 2\pi]$ range. Most function generators commercially available are not capable of changing

phase of the signal, without stopping the wave-train momentarily (at the order of 10ms). A random phase lag happens between the laser intensity and its modulating signal every time that the modulation signal resets (or pauses momentarily), making phase control practically impossible.

In order to overcome this hardware limitation, we increase frequency of the light, from its original value being equal to the frequency of the MEMS device, with a fraction of the frequency of the camera. This increase should be considerably small or it can result in blurry fringes. It was found that increasing the frequency of the light with a value equal to $0.5\% - 5\%$ of the camera frequency is practical and does not result in blurry fringes. For example, in order to capture the complete vibration profile of MEMS device vibrating at $1MHz$, using spectroscopy and a camera that captures one frame per second, we can set the frequency of the laser to $1000000.001Hz$. This offsets the phase of every frame $\frac{2\pi}{1000}$ with respect to the precious frame, requiring a total of 1000 frames to capture the complete vibration profile. Figure 4.6 illustrates this concept at a much lower frequency and number of frames.

4.6 Developed Software Packages

Two highly sophisticated software packages are developed to run the microscope and the MEMS device under it, acquire interferograms and process them. One of these softwares is developed in LabVIEW and the other one in MATLAB. It is recommended that each of these softwares run on its own dedicated workstation for best performance.

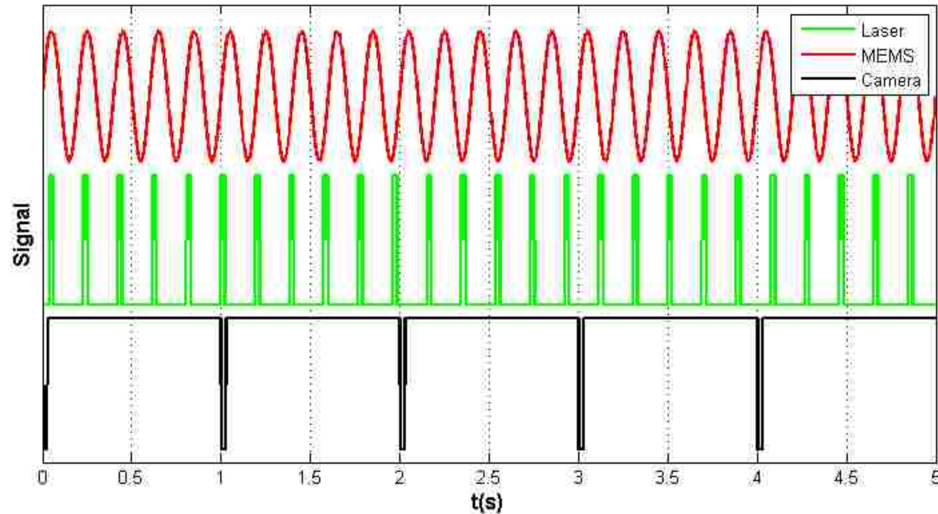

Figure 4.7: In case of hardware limititions when it comes to continuous phase control, relative frequency difference can be used to create phase difference in consequtive frames. This figure shows how to image the full vibration mode using only 5 frames. The accruacy of this method increases as the number of frames used to cover the full vibration mode increases. The low number of frames used here is for illustration purposes only.

4.6.1 LabVIEW Code

In order to control the actuation of MEMS or phononic crystals, modulate the laser source and trigger the camera as well as synchronizing the two workstations needed to operate the microscope, three electrical signals in form of voltage sources are required. These signals are generated using function generators obtained from Agilent Technologies, controlled by the software developed in LabVIEW. The interface of this program is shown in Figure 4.8.

The signal required to control the laser diode is a voltage source and it specifies the current passing through the laser diode. The camera-trigger-signal is used to trigger the camera and at the same time synchronize the MEMS actuation and the image acquisition controlled by two separate computers. This aspect will be described in

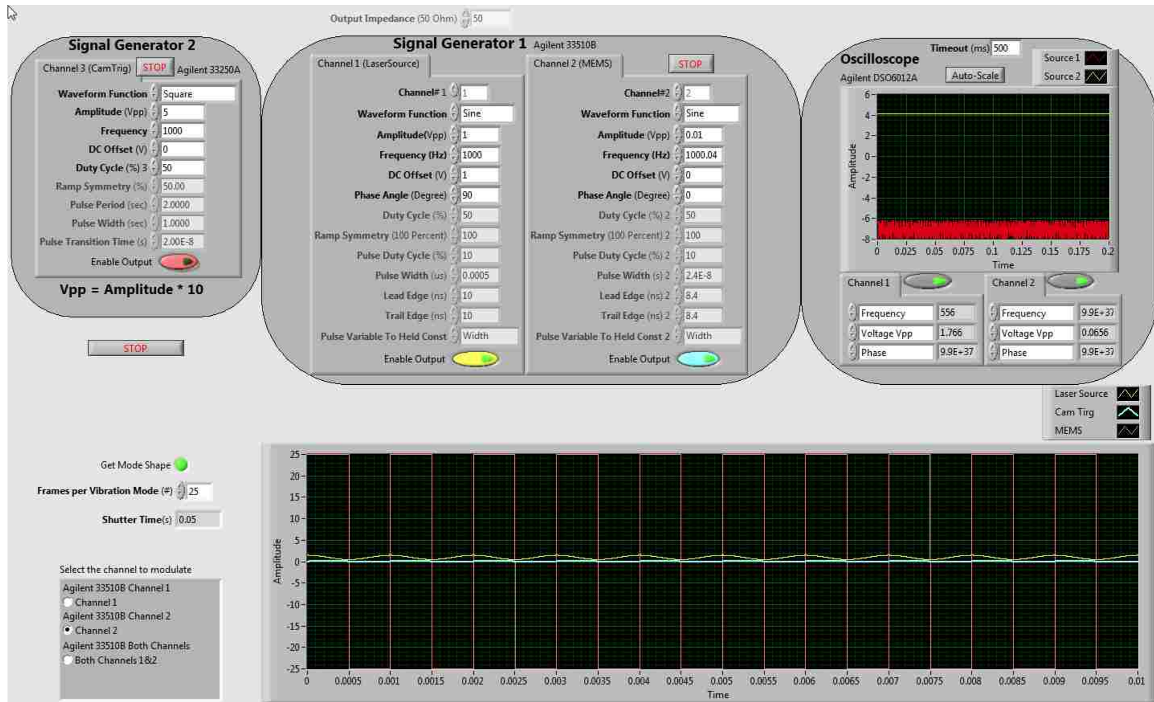

Figure 4.8: The user interface of LabVIEW code used to generate the actuation signal for the phononic crystal (MEMS Waveform Settings), Laser Source control (LED Waveform Settings) and triggering the camera (CamTrig Waveform Settings).

more details in Synchronization Section.

4.6.2 MATLAB Code

The image acquisition and post-processing is performed using MATLAB and the second workstation. The more than 15000 lines of code written in MATLAB, captures the micrographs using a SONY FireWire CCD camera(XCD 910UV) and does all the numerical analysis required to generate a live 3D image of the vibrational modes of the MEMS device and save it as a video file. The user interface of the software developed in MATLAB is shown in Figure 4.9. The software package developed gives user full control over all of the camera settings such as:

- Shutter mode
- Shutter timing
- Exposure
- Brightness
- Gain
- Image resolution
- Trigger source
- Trigger repeat
- Data Logging
- Noise reduction
- Tip-tilt correction
- 2D/3D imaging
- Preview mode
- Live data saving
- Live continuous mode

For every frame captured an automatic FFT analysis is used to remove the high frequency noise and diffraction effects. The 8bit image data are in intensity form, ranging from 0 to 255. Theoretically a constructive interference should yield in a white pixel with intensity of 255 and a destructive interference should yield in a black pixel of 0 intensity. In reality, peaks can vary in intensity anywhere from 230 to 255 and valleys can vary from 0 to 20. In order to prevent any saturation it is

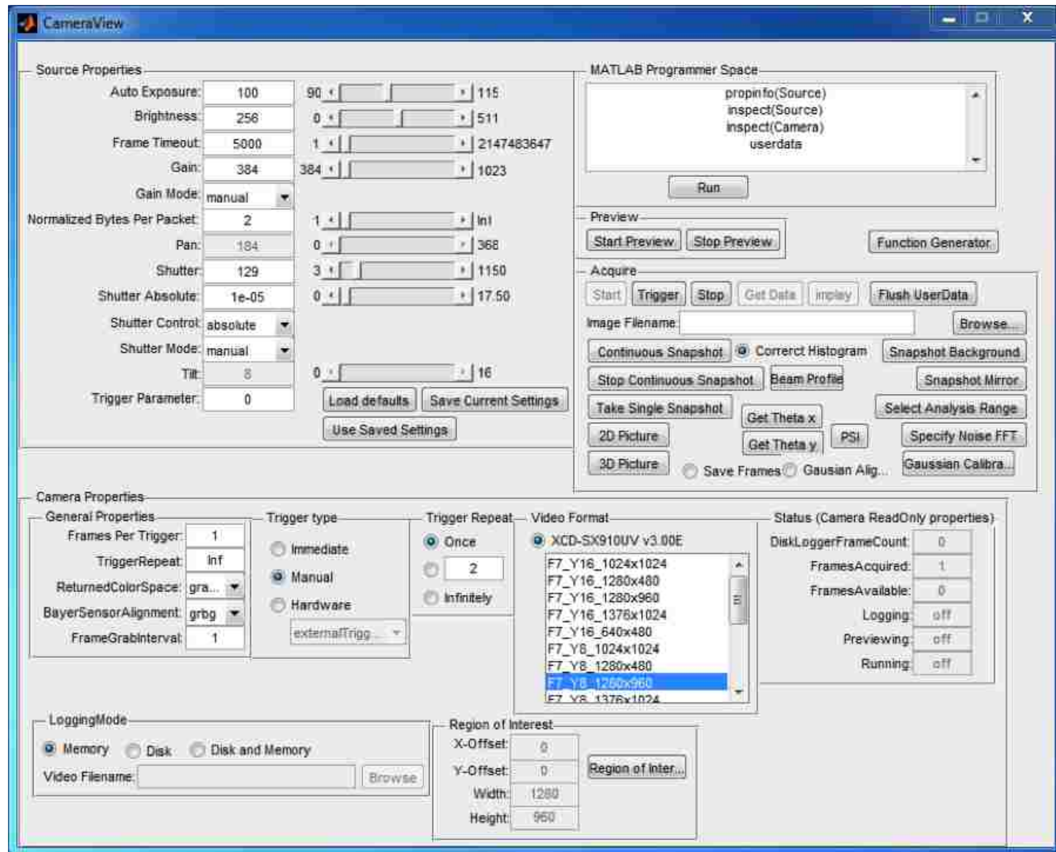

Figure 4.9: The user interface of the MATLAB code developed for image acquisition and post-processing of data.

highly recommended to adjust the shutter timing such that the minimum intensity is always higher than 0 and the maximum intensity is lower than 255. The maximum and minimum value of intensity is displayed in the live preview window to facilitate this. The MATLAB code developed here calculates the wrapped phase values for every interferogram, unwraps it, finds the 3D shape of the device and creates a movie of the complete vibration profile automatically.

4.7 Synchronization

The MATLAB and the LabVIEW codes are not only written to be very flexible and customizable to work with different function generators and cameras but they are made to work in a synchronized fashion on two separate computers that can even have different operating systems. The LabVIEW code does not require considerable computational power and can run on an average PC. The MATLAB code on the other hand requires considerable computational resources.

The camera trigger signal is the bridge between the two computers. MATLAB code detects the triggering signal sent by LabVIEW to the camera and acts accordingly. The transfer of data from camera to MATLAB is done on every frame to facilitate live image acquisition and image processing. If required it is also possible to average a couple of frames to require one super high quality image for static mode.

4.8 Theory of Fringe Formation in Michelson Interferometry

The coherent light beams used for interferometry are electromagnetic waves which can be represented as (4.1). It is the phase difference between the two waves, rather than the absolute phase values of each wave that is deterministic in fringe formation. This means that the phase of one of the beams can be considered to be zero and the phase difference be due to the second beam only. This is done only for simplification purpose and does not effect the nature of equations neither the final results.

$$\begin{aligned} E_1(x,y,t) &= E_1^0(x,y)e^{i\omega t} \\ E_2(x,y,t) &= E_2^0(x,y)e^{i[\omega t+\Phi(x,y)]} \end{aligned} \tag{4.1}$$

In this set of equations e_i shows the amplitudes of the electromagnetic waves, ω is equal to 2π multiplied by the frequency of the light, which is $564THz$ for the green light used here and $\Phi(x, y)$ is the total phase at different locations in the image. The interference wave equation is obtained by addition of the waves as in (4.2).

$$E(x, y, t) = E_1^0(x, y)e^{i\omega t} + E_2^0(x, y)e^{i[\omega t + \Phi(x,y)]} \tag{4.2}$$

The CCD camera doesn't record the wave equation thought. The information obtained from the camera are in the form of images which show the intensity(power multiplied by detector cross sectional area) at every point. Power of an electromagnetic wave is obtained as (4.3) where $E^*(x, y, t)$ is the complex conjugate of $E(x, y, t)$ and τ represents the duration of one period.

$$P(x, y, t) = \int_0^\tau \frac{E(x, y, t)E^*(x, y, t)}{\tau} dt \tag{4.3}$$

4.9 Fringe Analysis

Every interferogram can be considered as a superposition of the background image of the sample (2-D image of a sample under microscope) and the fringe patterns which adds the of the third dimension to the image. There are multiple methods to analyze the fringe patterns of interferograms. The most natural method is fringe tracking which is basically finding the constructive and destructive interference extremes and taking into account that every two consecutive constructive interferences correspond to an out of plane height difference of $\frac{\lambda}{2}$, but this method is very vulnerable to noise and other effects such as inconsistencies in reflectivity of the samples at different points. Fourier method [120, 93, 94] is a more robust method for fringe analysis. This method is computationally more expensive but yields in useful phase information even in relatively low fringe contrast situations or considerably noisy images.

4.10 Phase Analysis Using Fourier Transforms

Fourier Transform Analysis provides a much more robust method to find the phase compared to the fringe tracing method [120, 93]. The Fourier method is robust to noise caused by unwanted vibrations or diffractions from debris, reduced contrast due to unwanted vibrations and reflectivity inconsistencies along sample. It also enables one to separate the background image from the superimposed fringe patterns. But it is much more demanding when it comes to computational cost and needs the fringes to have certain characteristics to be effective.

Fourier methods are used to analyze the image in phase space rather than length space. Usually the fringes correspond to higher frequencies, in the phase space, compared to the background image and can be separated from the background information which correspond to the 2D image f the sample. The higher the number of fringes the higher the frequency they correspond to. Since there is no clear boundary between the frequencies corresponding to the fringes and the frequencies corresponding to the background data, it is a good practice to increase the number of fringes on the sample by tilting the reference mirror. Increasing the number of fringes further separates the poles in the frequency domain, making it easier to distinguish the fringe information from the background and reducing the error associated with removing the low frequency background data.

Using (4.1) - (4.3) the intensity of the light at every pixel of the CCD can be written as a function of the intensity of the light reflected from the MEMS sample, $g_1(x, y)$, and the reference mirror, $g_2(x, y)$, as (4.4)

$$g(x, y) = g_1(x, y) + g_2(x, y) + \sqrt{2g_1(x, y)g_2(x, y)}cos(\Phi(x, y)) \tag{4.4}$$

The phase difference between the two incident beams, $\Phi(x, y)$, is equal to:

$$\Phi(x, y) = \phi_0(x, y) + 2 * \pi\mathbf{F} \cdot \mathbf{R} \tag{4.5}$$

where $\phi_0(x, y)$ is the initial phase difference between the sample and the mirror beams, $\mathbf{F}$ is the frequency vector and $\mathbf{R}$ is the coordinate vector in the plane of image.

Equation (4.4) can be rewritten in the mode compact form of (4.6):

$$g(x, y) = a(x, y) + b(x, y)cos(\Phi(x, y)) \tag{4.6}$$

Substituting for $\Phi(x, y)$ from (4.5) and using trigonometric to exponential expansion, the intensity of the light received by the camera (4.4) can be written in the general form of (4.7):

$$g(x, y) = a(x, y) + c(x, y)e^{2\pi i\mathbf{F}\cdot\mathbf{R}} + c(x, y)^{*}e^{-2\pi i\mathbf{F}\cdot\mathbf{R}} \tag{4.7}$$

in which

$$c(x, y) = \frac{1}{2}b(x, y)e^{i\phi_0(x,y)} \tag{4.8}$$

Figure 4.10 shows a sample interferogram of a μcantilever array. The Fast Fourier Transform(FFT) of this interferogram is shown in Figure 4.11 . It worth mentioning that when plotting the FFT of an image it is common to plot the logarithm of the power of the FFT which in turn is equal to the FFT value at every pixel multiplied by its conjugate value divided by the number of pixels.

The three distinct poles seen in Figure 4.11 is not a coincidence but rather a consequence of creating considerable number of fringes. If the tip-tilt angle of the reference mirror is increase enough to produce considerable number of fringes there will be at least three distinct poles in the FFT of the interferogram. In order to have these poles separated from each other, one needs to have a considerable number of fringes to start with. The central pole located at point $F = (0, 0)$ in frequency domain and the region around it corresponds to the background information. The other two poles are complex conjugates and are the result of fringes. Each of the

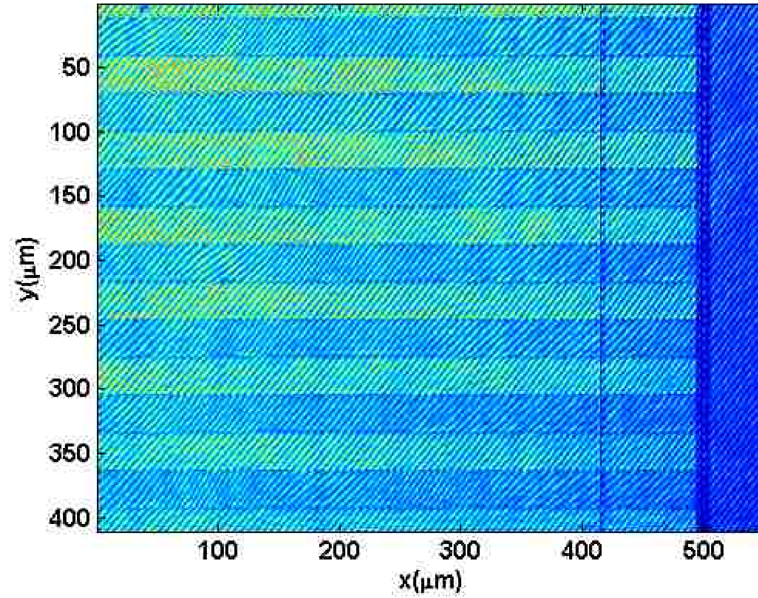

Figure 4.10: A sample interferogram with considerable number of fringes.

offset poles carry enough information to reconstruct the fringes [120], making the other one redundant.

Equation (4.7) shows the Fourier transform of (4.7). In this equation $A(F_x, F_y)$, $C(F_x, F_y)$ and $C^*(F_x, F_y)$ are the Fourier transforms of $a(x, y)$, $c(x, y)$ and $c(x, y)^*$.

$$G(F_x, F_y) = A(F_x, F_y) + C(F_x - F_{0x}, F_y - F_{0y}) + C^*(F_x + F_{0x}, F_y + F_{0y}) \quad (4.9)$$

As explained, $A(F_x, F_y)$ includes the information about the background image (with no fringes) and the two complex conjugate poles of $C(F_x - F_{0x}, F_y - F_{0y})$ and $C^*(F_x + F_{0x}, F_y + F_{0y})$ have the information about the fringes superimposed on the background image. The goal in phase analysis using the Fourier transform method is to remove the effects of the light coming from the sample and the mirror and find the phase difference between the two beams of light at every pixel of the image. This is accomplished by filtering the central pole in the FFT and transferring one of the conjugate poles, $C(F_x - F_{0x}, F_y - F_{0y})$ for example, to the center in order to

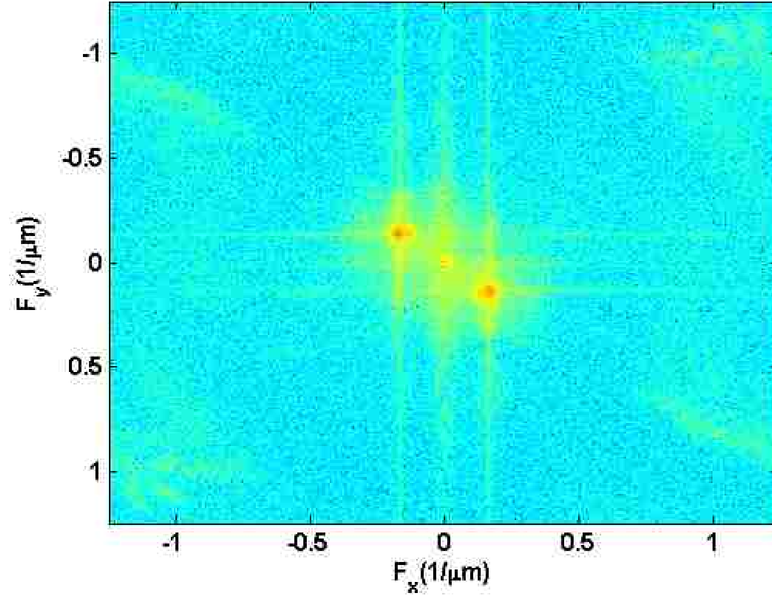

Figure 4.11: Fast Fourier transform of an interferogram

eliminate the offset and get $C(F_x, F_y)$ (see [120, 93]). Once $C(F_x, F_y)$ is found an inverse Fourier transform is used to get $c(x, y)$, which based on (4.8) can be used to calculate the phase, as the imaginary component of (4.10).

$$log[c(x, y)] = log[1/2b(x, y)] + i\Phi(x, y) \tag{4.10}$$

The MATLAB software developed here, uses this Fourier method to filter background information and the obtain phase. In addition to all the previous advantages mentioned, this method also removes the tilt of the sample as well. Figure 4.12 shows the phase data for the interferogram of Figure 4.10. Pay attention that the phase information obtained using Fourier method is sliced into $[-\pi, \pi]$ range so it jumps to $-\pi$ after reaching π and vise versa. This is the reason why the phase information obtained by this method are called wrapped phase information.

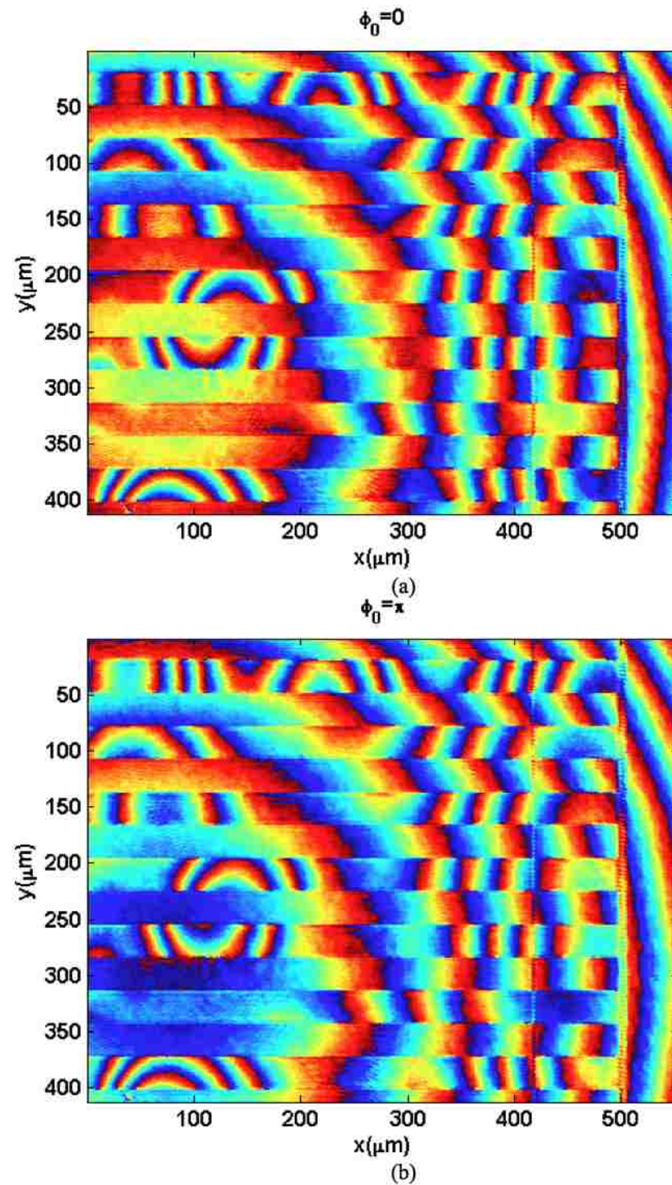

Figure 4.12: Phase data for the interferogram of Figure 4.10 using the Fourier method. (a) shows the phase when the initial phase is considering to be equal to zero. (b) shows the phase when the initial phase is considering to be equal to π. The two phase plots belong to the same interfrogram but using different initial phases two different looking wrapped phases can be obtained. At places when part (a) reaches π or π, (b) has a value around zero and is continuous. Obtaining two phase plots for the same interferogram in this fashion makes phase unwrapping possible.

4.11 Phase Unwrapping

Whether one uses fringe tracing or Fourier method for phase analysis, the final result is limited to $[-\pi, \pi]$. Every 2π phase difference corresponds to $\frac{\lambda}{2}$ height difference on the sample. This means that if the out of plane deformation/dimension of the sample is grater than $\frac{\lambda}{2}$, its phase will be modulated into this range by breaking it into slices of $\frac{\lambda}{2}$ and consequently 2π. A process known as phase unwrapping is required to stick the modulated phase information after Fourier analysis. 3-D phase unwrapping is one of the problems that is still not solved completely. The most successful method so far, uses iterative Fourier transforms to unwrap the phase information [19, 128, 127, 129, 111] but it is computationally too expensive to be applicable to real experiments.

The method developed here provides a robust and efficient method for three dimensional phase unwrapping. It is however limited to continuous samples only. For noncontinuous surface, there is no unique way of unwrapping the phase since interference of waves is not sensitive to $2n\pi$ phase differences. If the surface does have teas and discontinuities larger than $\frac{\lambda}{2}$ (which correspond to phase differences larger than 2π), a unique phase unwrapping will be mathematically impossible. Using different methods to unwrap the phase in such a cases, yields in different results all of which have tears somewhere in the final phase surface but the locations, shapes and sizes of the tears does not necessarily correspond to their true locations, shapes and sizes on the sample.

It worth mentioning that changing the initial phase, before the inverse Fourier transform of $C(F_x, F_y)$ to get $c(x, y)$ values required for (4.10), we can actually simulate the motion of fringe on the sample as happens when the reference mirror or the sample are moved, in PSI and VSI methods respectively.

The phase unwrapping method developed here, starts with two sets of wrapped

phase matrixes, one with an initial phase of zero ($\phi_0(x, y) = 0$) and the other one with $\phi_0(x, y) = \pi$. Each of the two phase sets are in the form of strips in $[-\pi, \pi]$ range with discontinuities at both extremes. Using the two sets of phase matrixes corresponding to the same interferogram means where one strip reaches the π or π extremes the other one is continuous with its value is near the median value of zero. This enables full unwrapping of the phase by using the other set when one set is not continuous. Switching between the two sets the phase can be unwrapped as a continuous stream of data.

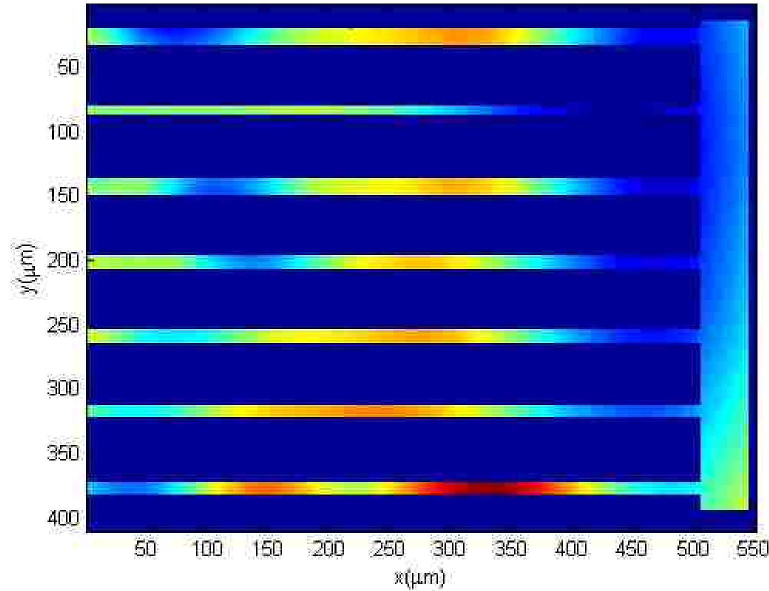

Figure 4.13: Unwrapped phase of Figure 4.10.

Figure 4.13 shows the results of unwrapping the phase of Figure 4.12 using the method developed here. The most important thing to consider when performing interferometry is that this interferometry might fail to correctly specify the height difference between two points if they can not be connected by a continuous 3-D curve (or polygon with some limitations). This is because interferometry can not tell apart between phase differences of θ and $2n\pi + \theta$ between two points, unless there

is a continuous 3-D path, with jumps smaller than $\frac{\lambda}{2}$, connecting them. There is a one to one correlation between the wrapped and unwrapped phase if the surface is continuous with out any tears and jump in out of plane direction and the problem is mathematically solvable as done in here. But any teas larger than $\frac{\lambda}{2}$ makes the unwrapping mathematically impossible to solve.

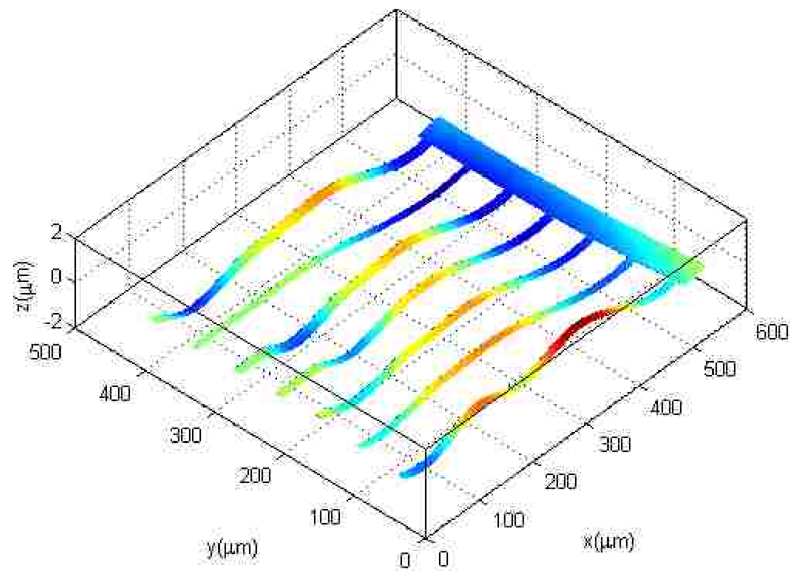

Figure 4.14: 3-D shape of the μcantilever array of Figure 4.10.

After selecting a continuous region or the sample and unwrapping the phase in the region, all that is required to find the out of plane height value for each pixel is to consider that every 2π phase difference corresponds to $\lambda/2$ height difference in out of plane direction. Figure 4.14 shows the final 3D shape of the μcantilever array of Figure 4.3

4.12 Conclusion

This chapter introduces a new operation mode to the Michelson interferometry which has considerable advantages over PSI and VSI. The microscope developed here, not only increases the accuracy considerable but broadens the operation of interferometry to highly dynamic experiments. The long distance optics make it possible to observe experiments done under vacuum as well.

Using Fourier phase analysis provided a stable and robust method for phase analysis of interferograms. The 3-D phase unwrapping method developed here proved to be a highly effective and efficient for unwrapping the wrapped phase information obtained using interferometry to get the 3-D heigh information and sample shape reconstruction in 3-D.

The next two chapters will be focusing on the mechanical and electrical properties of entangled networks of carbon nano fibers. The samples are studied both under tension and compression. The experiments performed are designed to study the behavior of the samples both under small and large forces.The effects of relatively small forcer are studied in Chapter 5 and the effects of larger forces are studied in Chapter 6.

Chapter 5

Synthesis & Characterization of A Nonwoven Carbon Nanofiber Structure

5.1 Overview

A unique type of nonwoven carbon material has been developed which is flexible, resilient, and produced at modest temperature and near ambient pressure using catalytic deposition. This material is comprised entirely of nanoscale carbon fibers, which are extensively interlaced to create a coherent, bulk material. The structure and basic mechanical and electrical properties of this material were investigated through cyclic compression and in situ resistance measurement. The material was highly elastic and capable of being repeatedly compressed without disintegration. The mechanical response varied with density, and the density was controlled by the amount of catalyst used. The material exhibited a high electrical resistivity, which varied nonlinearly with compression.

5.2 Introduction

Macroscale carbon materials composed of nanoscale features are of interest for lightweight thermal management [41], catalyst support [85], and electrical applications such as supercapacitor electrodes [72]. Currently, advanced carbon materials come in a variety of configurations such as nanotube nonwovens [117], aerogels [78], and nanoporous foams [64].

Herein, we report on a new, low cost, reliable process for creating macroscale (bulk) carbons comprised of intertwined nanoscale carbon fibers. This process includes some unique aspects: (i) the ability to grow the nonwoven material to a specific shape, (ii) the ability to control the morphology of the constituent fibers, and (iii) the ability to grow the fibers at a relatively low temperature (550 C in the present study).

The process for creating these nanoscale nonwoven carbon materials is a direct extension of earlier work [13] where Pd was found to rapidly catalyze carbon deposition in an ethylene and oxygen environment. This technique is broadly based on the Graphitic Structure by Design (GSD) method [96] as applied to carbon nanofiber production [13, 11]. Fiber production based on this process of partial hydrocarbon oxidation generally proceeds by exposing metal catalyst particles (e.g. Ni or Pd) to a fuel-rich mixture of ethylene and oxygen (or alternatively ethylene and hydrogen) at ambient pressure and a temperature between 500 and 750 C. The primary modification employed in the present case was to use a mold to constrain the fiber growth, thereby creating a macroscale carbon structure, comprised entirely of nanoscale fibers, of well-defined external dimensions.

The effects of process variables on the morphology of the nanofibers and the morphology's impact on macroscale properties were also determined. Among the most important process variables are catalyst location, catalyst density in the mold, pro-

cessing time and temperature program. This multi-scale property control capability results in a highly adaptable process and product.

These macroscale carbon structures were characterized for their mechanical and electric properties. The bulk material has a low density ($0.120.40g/cc$) and has been found to be stable under moderate compressive cycling. In compression, the material was found to be elastic over multiple strain cycles and have a modest modulus of elasticity of $1 - 5MPa$. The electrical conductivity increased with compressive strain, presumably due to increased fiber contact. Modeling of both the mechanical and electrical behavior indicates that the material behaves as a nonwoven material.

5.3 Experimental

Nanoscale nonwoven carbon structures were generated using sub-micron Pd powder (99.9%, Sigma Aldrich) as the catalyst. This powder was placed preferentially at the edges and center of a rectangular mold ($50 \times 25 \times 5mm$ with $6mm$ corner radii). The mold was heated to 550^oC while flowing nitrogen ($99.999\%, 100ml/min$) at atmospheric pressure. Once at temperature, a $1 : 1$ mix of ethylene (chemically pure) and oxygen (99.99%) flowing at $15ml/min$ each was added to the continuing nitrogen flow. Depending on the initial palladium loading, the reaction lasted $619h$ before the pressure in the mold increased to that of the pressure relief valve ($7kPa$ above ambient). Pd loadings between approximately 2 and $20mg$ were tested, and the time required to fill the mold was inversely proportional to the amount of catalyst when considered over the whole range of loadings (i.e., $220mg$). The total process time for similar catalyst loadings varied by $23h$ between runs. On average it took $6h$ for the mold to fill when using $20mg$ of catalyst and $17h$ for $2mg$. At completion, the carbon fills the mold and the pressure increases to that of the pressure relief valve. Herein, this technique will be referred to as the Constrained Formation of Fibrous

Nano-structures (CoFFiN) process.

Densities of the carbon structures were determined geometrically by measuring the volume and mass of the sample. Morphologies were inspected using an FEI Quanta 3D FEG Dual Beam system. The electron gun was used for imaging and the focused ion beam was used to cross-section the samples. The mechanical and electrical properties were determined simultaneously using a custom setup on an Instron Model 1011. A $45N$ load cell was used to characterize the material in compression between two parallel, aluminum plates, electrically isolated from the load frame. A current of $250mA$ was applied to the sample, and the voltage drop across the sample was measured in order to determine the instantaneous resistance with displacement.

5.4 Results

Two samples with densities of 0.12 and 0.40 g/cc were characterized. The only process variation was the amount of Pd catalyst used (3 and $1.6mg$, respectively). The times it took for the samples to reach the pressure limit were 17 and $16h$, respectively. An example of a carbon sample is shown in Figure 5.1a. Scanning electron microscopy (SEM) (Figure 5.1b) shows the structure to be entirely fibrous. A focused ion beam was used to mill sections of carbon away to allow evaluation of the sample's immediate interior. An example of the resulting section is shown in Figure 5.1c and d. This reveals that the interior is consistent with the exterior, and the fiber density is uniform on the length scale examined.

Qualitatively, the nonwoven material was found to be flexible and resilient which allowed for repeated bending past 90° (Figure 5.2a). After a small amount of elastic recovery, the bulk material maintains the deformed shape. The material could be flattened once again by bending in the opposite direction without noticeable cracking or disintegrating. The flexibility seems to be inversely proportional to density.

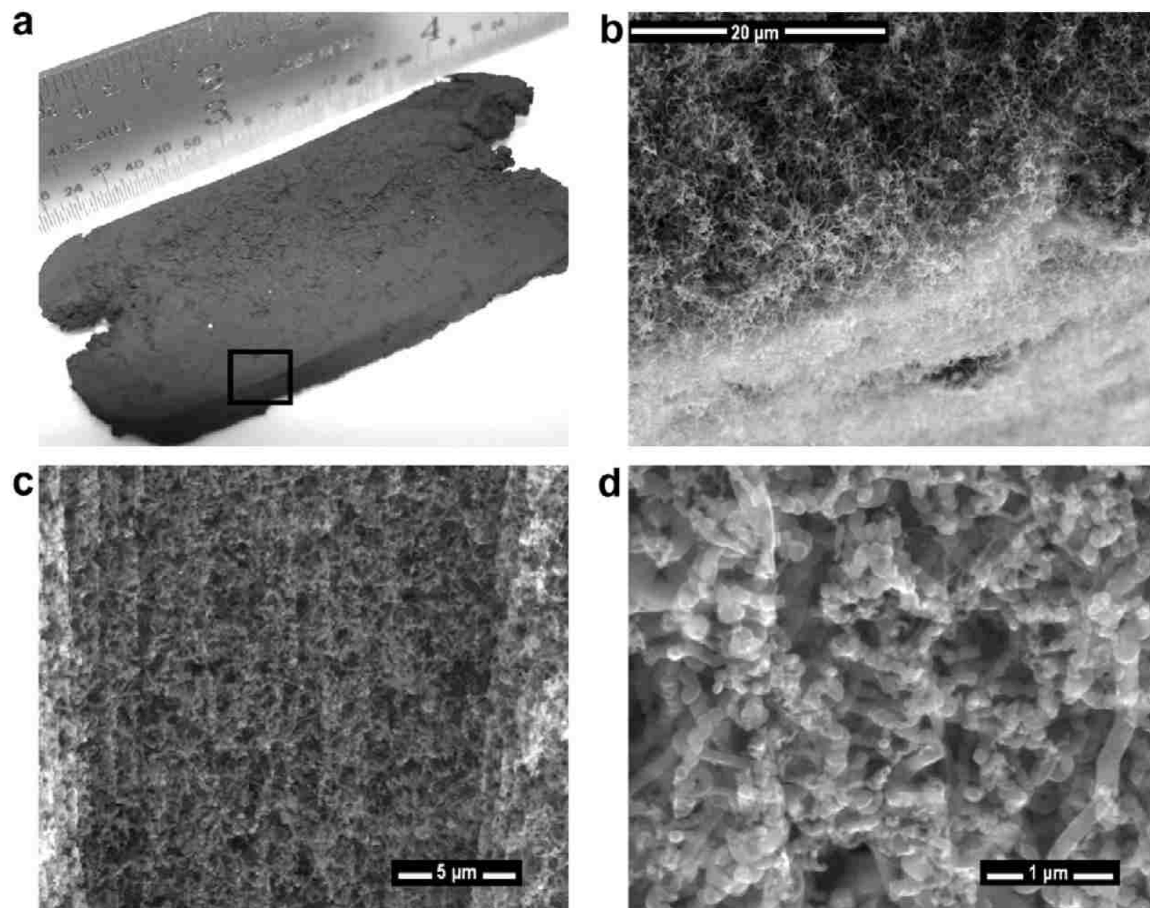

Figure 5.1: Fibrous carbon foam structure viewed (a) optically (scale in inches), (b) SEM micrograph of exterior edge boxed in (a), (c) secondary electron image after FIB sectioning, and (d) magnified view of sectioned fibers in (c).

A more quantitative measurement of the mechanical properties was sought by compression testing. Samples were prepared by sectioning with a razor blade to create in-plane dimensions of $10 \times 10mm$ and thickness of $5mm$. The samples were loaded and unloaded at a constant rate of $2.5mm/min$ between a zero stress level and 450kPa. The samples were electrically isolated and the resistance measured by maintaining a 250 mA current and measuring the voltage drop across the material. This setup is depicted schematically in Figure 5.2b. By this method, the samples could be electrically characterized in parallel with the mechanical testing.

Under compression, the behavior of the 0.12 and the $0.40g/cc$ material were qualitatively similar in mechanical and electrical response, but the difference in density separated them quantitatively (see Figure 5.2c and d). The main characteristics that differentiate between the densities are the elastic moduli and the resistance change in the material during compression. Note, in the compression cycling, only cycles 1, 3, 5, 7, and 10 are plotted for ease of viewing. The data shown in Figure 5.2c and d are representative of several experiments performed on each density of material. Results were repeatable across samples of the same density.

The lower density sample ($0.12g/cc$) required several cycles before reaching a stable loading response, but the higher density sample ($0.40g/cc$) performed uniformly throughout the compression cycling. If a greater load could be applied (requiring a load cell with a higher capacity), it is thought the sample of greater density would show a similar response to the lower density sample in regard to stabilization of the response and hysteresis during unloading, This will be a future area of study.

Figure 5.3a displays the elastic moduli of the samples over 10 cycles. The elastic moduli were calculated using a linear regression in the loading and unloading portions of the curves using the full range of strain when loading and the first 15% of the strain when unloading. Error for the linear fits was less than 1.5% in all cases. The difference in the elastic moduli for loading and unloading is significantly larger for the lower density material, but the elastic moduli were nearly constant for both materials. The higher density material has a lower strain at the maximum load, and this is thought to contribute to its relative stability in regard to its mechanical response.

The resistance changes of the samples were recorded contemporaneously with the loaddisplacement data (see Figure 5.2c and d). The resistance shows an inverse relation to strain. During loading, the resistance decreases monotonically until its slope approaches zero. The resistance is highly linear in the first 10% of the strain

during loading and last 10% during unloading for each cycle and exhibits strain sensitivities of more than $500\Omega/\epsilon$ for $0.40g/cc$. During unloading, the resistance, R, increases until it approaches a rate similar to that of loading and an absolute value close to that of the unloaded sample. Because the material shows a nonlinear resistance response with strain, the bulk resistivity also varies. From the uncompressed condition (at R_{max}) to maximum strain (at R_{min}), the $0.12g/cc$ material exhibited a resistivity range of $0.071 - 0.014\Omega m$. Likewise, the resistivity range for the $0.40g/cc$ material was $0.049 - 0.020\Omega m$. This electrical behavior is depicted schematically in Figure 5.2b where the FCF is labeled as a variable resistor.

5.5 Discussion

The carbon materials generated for this study can be classified with nonwoven materials, which have many applications such as insulation and filtration [22]. A variety of processing techniques are available, but in general, the major steps involve web formation, web bonding, and finishing [108]. Currently, many nonwovens (mainly for the textile industry) can be produced in high-volumes economically, but there exists the potential for improving the properties and extending the applications by developing advanced nonwovens. The future of advanced nonwovens is commonly anticipated to come in the reduction of fiber size. Nanoscale nonwovens are expected to benefit filtration [57, 137] and insulation [42] applications. Carbonaceous materials may be of additional interest in insulation [136] and fire barrier [61] applications where environmentally friendly, flame-retardant materials are desirable.

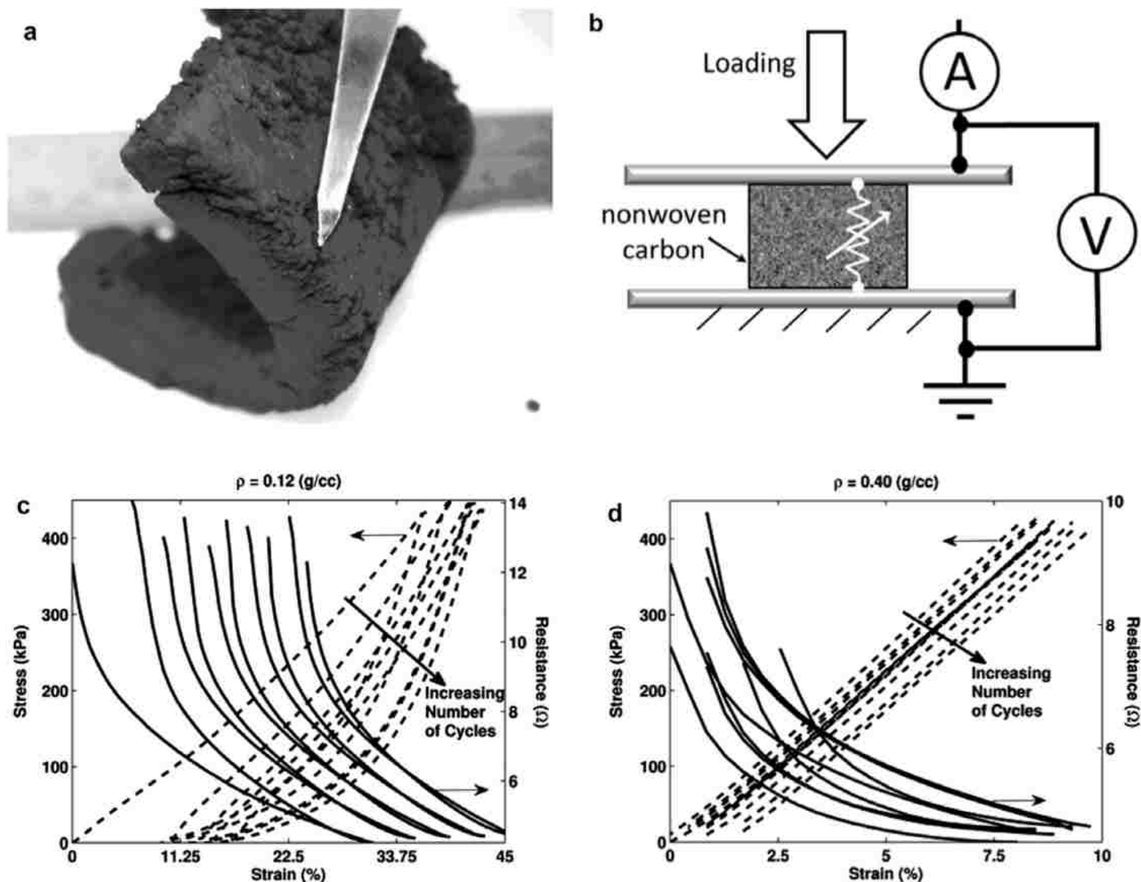

Figure 5.2: (a) FCF under flexing. (b) Schematic of experimental setup for measuring mechanical (dashed lines) and electrical (solid lines) properties. Cyclic compression results are shown for (c) $0.12g/cc$ and (d) $0.40g/cc$ foams.

5.5.1 Processing

Carbon nonwovens are used in applications such as electrodes [26], tissue scaffolding [100, 84], and air filtration [28]. These carbon materials can be generated by a variety of techniques, but comparison will be limited to those used in producing materials with nanoscale (¡1 lm) fibers. For example, carbon nanotubes (CNTs) have been used to form bulk structure through dense alignment using a liquid-phase deposition process [4], and also by binding with an organic precursor in a solgel pro-

cess [133]. Catalytically, CNTs have also been directly synthesized into bulk (cm dimension) structures by subliming ferrocene and sulfur at low temperature in one furnace ($85 - 95^oC$) then transferring the gaseous products with a flow of argon and methane to a second, high-temperature furnace (1100^oC) where catalytic reaction lead to the formation of the CNTs [117] via thermal decomposition. The carbonaceous products were then peeled from the wall of the quarts tube after a $6 - 9h$ reaction. These nanoscale carbon nonwovens require high temperature to catalytically form the CNTs. This high temperature requirement also applies to nonwoven structures comprised of electropsun polymer nanofibers that must be carbonized at high temperature (e.g., [26, 27]). High temperature ($> 1000^oC$) increases process complexity and limits the incorporation of secondary materials to form composites.

The CoFFiN process not only directly synthesizes bulk structure, but it goes further in creating a tailored bulk structure as determined by the mold dimensions. Basic laboratory equipment is used, and the material is formed under modest temperature ($< 700^oC$) and near ambient pressure ($7kPamax$). Furthermore, the nonwoven material needs no carbonization. Most carbon formation processes rely on high temperature thermal decomposition (¿1000 oC), whereas the CoFFiN process relies on the creation of radical species via a low temperature (ca. 550^oC) combustion process. Since the fabrication takes place at low temperature, other materials with relatively low melting temperatures can be incorporated to form composite structures. This aspect has been successful in preliminary work and is an ongoing area of research. The process is highly adaptable and amenable to assimilation with other technologies (e.g. polymer reinforcement).

Another advantage is that the operating parameters employed in processing can be readily varied to control the fiber properties. By choosing different gases, gas ratios, temperatures, catalysts, etc. the fiber properties can be tailored, and by this, the bulk network can also be made to possess specific properties. In the present

work, the emphasis was on controlling the bulk density. This was done by modifying the catalyst charge, but it is clear from earlier work that changes in fiber diameter [15]], basic fiber morphology [11] and other properties [16, 14] can be controlled as well.

The direct synthesis procedure also provides a vehicle for utilizing the constituent carbon nanofibers (CNFs). No additional steps are needed to introduce them onto a support or otherwise aggregate or distribute them, and this allows direct use in applications such as catalyst support, gas storage, and composite reinforcement [32, 105]. The ability to form these materials in any arbitrary shape only adds potential applications.

5.6 Mechanical properties

Nonwoven materials are most commonly tested under compressive conditions. Though it was of interest to test the mechanical response of the carbon material produced by the CoFFin process, the task was intended to be preliminary and not exhaustive. The compressive behavior of nonwoven materials is commonly described by the model of nonwoven materials van Wyk [126] where fiber bending is the sole contributor to mechanical resistance. As noted by van Wyk in [126], fiber properties such as diameter, length, crimp frequency, etc. will influence the behavior of the collective material and cause deviations from the proposed ideal behavior that considers only bending. In van Wyk's model stress, σ, can be modeled as:

$$\sigma = k(\mu^3 - \mu_0^3) \tag{5.1}$$

where k is a fitting parameter that is representative of the fibers' properties as mentioned previously, l is the instantaneous volume fraction of fibers and lo is the initial volume fraction of an assembly of fibers. This model was applied to a loading curve

for the data in Figure 5.2c and d, yielding Figure 5.4a and b, respectively. The agreement for in the fit reinforces that this is a nonwoven material.

Through deliberate selection of processing parameters, fiber characteristics can be customized during growth. The morphological properties of nonwoven materials are determined by fiber orientation [101] and compressive stresses [49], which influence characteristics such as pore size (critical for filtration applications). Typically, nonwovens can be considered two-dimensional [95] since there is often limited orientation of fibers in the z-direction [101]. Fibrous materials produced by the CoFFiN process have no significant propensity for two-dimensional growth and therefore are expected to behave more isotropically.

In the compression tests used for this study, the nonwoven carbon showed no ultimate compression strength (failure) up to the maximum stress applied ($0.4MPa$) and the stiffness ($15MPa$) could be modified by changing the density. Even though modest, the loads applied here reveal that the material behaves as a random network of fibers, though higher loads would be necessary to determine full range of mechanical response. Hysteresis in the low-density sample can be attributed to fiber friction [37]. The lack of hysteresis in the high-density sample does not necessarily imply that it does not exist, but may not arise due to the lower strain achieved at maximum load. Further mechanical analysis is planned for future work. As a comparison, in [133] where CNTs were used to form a nonwoven structure, a slightly higher stiffness ($510MPa$) was found by nanoindentation at a density of $0.07g/cc$. Higher CNT contents (in relation to the polymer binder) increased the stiffness at a given density. Elastic recovery after compression was found up to 76% strain with a $55wt.\%$ CNT concentration ($q = 0.30g/cc$), but no mechanical data is presented for this higher concentration.

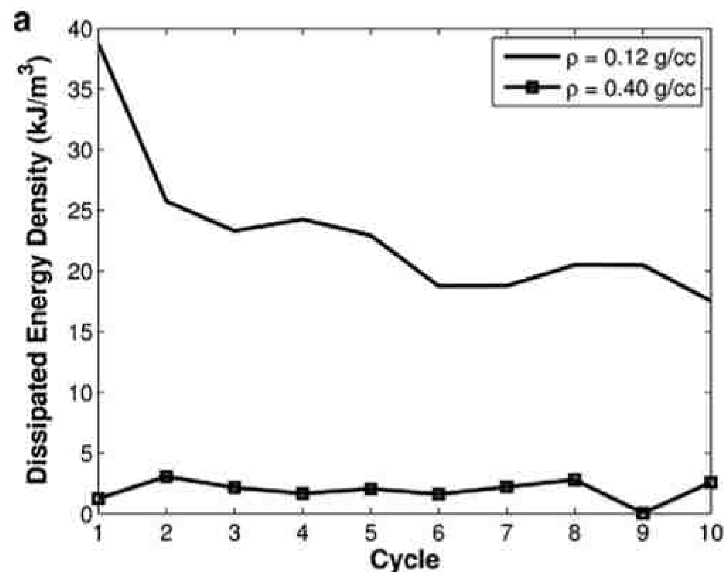

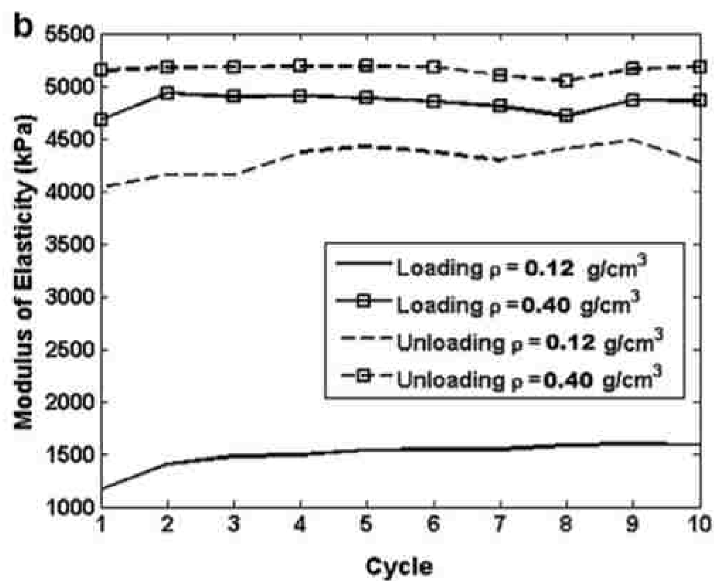

c

Density (g/cc)	Elastic Modulus (MPa)		Average Cyclic Energy Dissipation (kJ/m³)	Resistivity (Ω·m)	
	Loading	Unloading		Minimum	Maximum
0.40	4.8	5.2	1.95	0.020	0.049
0.12	1.5	4.3	23.1	0.014	0.071

Figure 5.3: Variation in (a) energy dissipation and (b) elastic moduli with cyclic loading and (c) tabulated properties of the carbon foams.

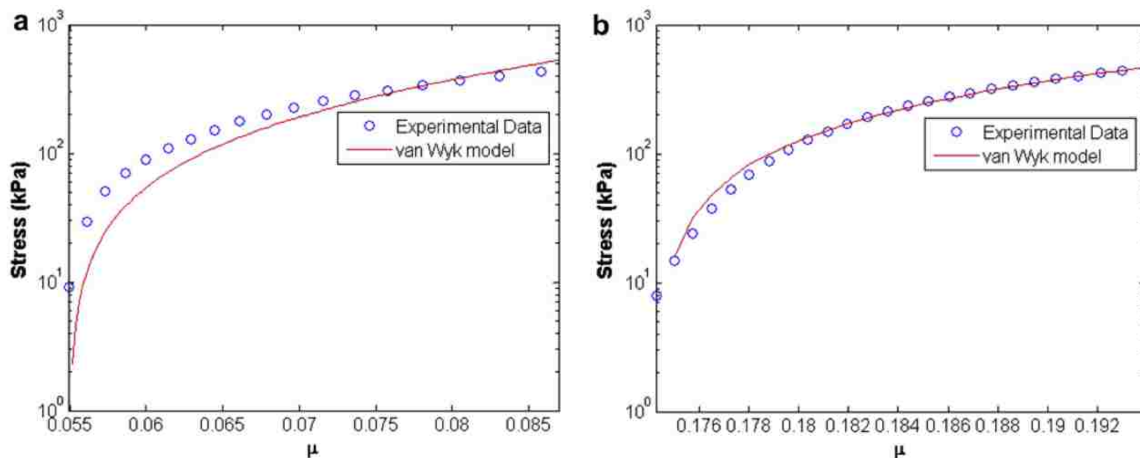

Figure 5.4: Plot of the resistance versus strain for the loading (a) and unloading (b) cycle 2 of the $0.12g/cc$ sample FCF (data points) and the model from Eq. (5.1) (line). The model shows qualitative agreement and demonstrates the validity of modeling the resistance change as a network of resistors.

5.7 Electrical properties

The electrical properties of the nonwoven material can be directly related to the crystallinity of the carbon itself and the randomly entangled nature of the nonwoven fiber network. From previous work under these growth conditions [13], the material is highly amorphous, and a high resistivity is expected. Examining Figure 5.2c and d, it can be surmised that as the nonwoven carbon fibers are compressed, an increasing number of fibers come into contact and thereby lower the overall resistance. Typically, colligated carbon nanofibers/ nanotubes used as strain sensors are embedded in a polymer matrix and tested under small strain conditions [52, 130]. The small strain condition yields fairly linear results. As such, linear fits with gage factors are used to model their behavior.

Other researchers have used more complex models for the ac-electrical behavior of nonwoven carbon nanotubes bundles as networks of resistor, capacitors, and inductors [53, 97]. Presently, experiments are conducted under dc conditions. Accordingly,

the nonwoven carbon fibers are considered to be resistors.

From the present discussion the nonwoven carbon nanofibers are clearly a network of intertwined fibers. This network will behave analogously to a random network of electrical elements, which have an increasing number of contacts as they are compressed. Using the concepts of van Wyk, the number of contacts between fibers in a nonwoven material can be described and applied to model for the resistance change of nonwoven carbon fibers. The number of contacts, n, has been previously found to increase linearly with an increase in volume fraction, $n(\mu)$ [104]. Under these conditions, the resistance of the nonwoven carbon fibers, R_{NWCF}, is found to be:

$$R_{NWCF}(\mu) = \frac{R_{CFS}}{n(\mu)} \tag{5.2}$$

where R_{CFS} is the resistance of a single carbon fiber system dependent on geometry and the resistivity of graphite, $n(\mu)$ is a linear function of the volume fraction. This model was applied to a loading curve for the data in Figure 5.2c and d, yielding Figure 5.5a and b, respectively. Again, the agreement for the fit reinforces that this is a nonwoven material. Deviations from this simple model are attributed to distributions of: the diameter of the fibers, their lengths, and crimp frequencies as the material is compressed [126]. Additionally, the crystallinity of the fibers has been found to vary [13] and thus the carbon fibers' resistivities will vary due to this distribution of crystallinity. A similar quality of fit was attained for other cycles of the nonwoven carbon fibers.

The overall shape of the resistance versus strain curves for the nonwoven carbon fibers in Figure 5.2c and d is amenable for sensing applications. The initial portion of all resistance-strain curves is highly linear, exhibiting strain sensitivities of more than $500\Omega/\epsilon$ (for the $0.40g/cc$ sample), which corresponds to $1\Omega/10\mu m$ of displacement in this study. Here, e is strain defined using the engineering definition of $(h - h_0)/h_0$, where h is the instantaneous height and ho is the initial height of the nonwoven carbon fiber assembly. Higher density nonwovens have a more repeatable response

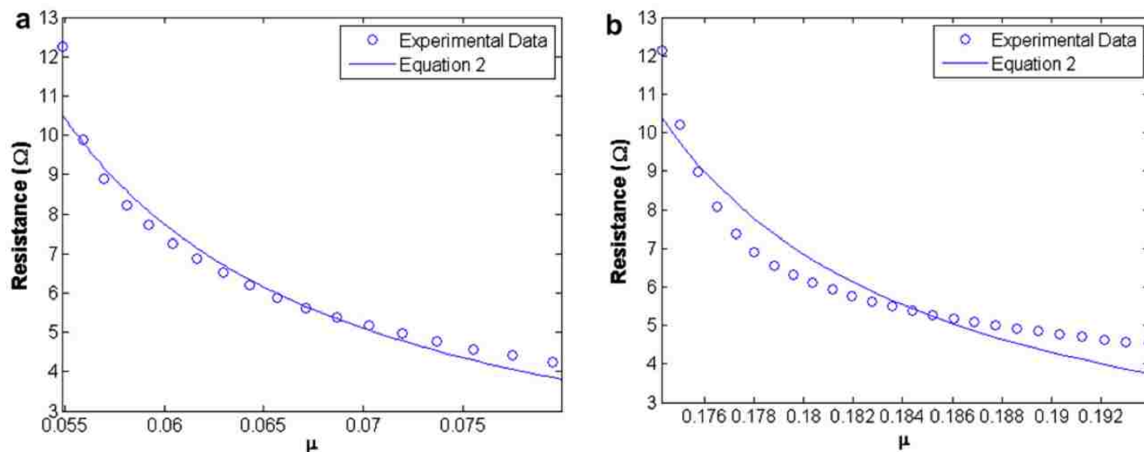

Figure 5.5: Resistance (Ω) versus volume fraction of fibers (unitless) for (a) $0.12g/cc$ (initial) density sample and (b) $0.40g/cc$ (initial) density samples. Circles represent actual data points and the lines are a fit from Eq. (5.2).

and are therefore more desirable as sensors. Presumably the nonwoven carbon fibers would not lose their resistance when impregnated with another material to make a composite, thus opening the possibility for a myriad of other potential applications that rely on strain sensing as demonstrated by other researchers [52, 53].

5.8 Conclusions

The Constrained Formation of Fibrous Nanostructures (CoFFiN) process is a very simple and adaptable method for creating uniquely structured carbon materials. The process is accomplished via the catalytic decomposition of a gaseous carbon feedstock at atmospheric pressure, and temperatures which are typically below 700 C. The process yields carbon comprised entirely of tightly entangled fibers. These nonwoven materials were tested in compression and the resistance was measured in situ. The low-density material ($0.12g/cc$) could be repeatedly compressed in excess of 35% without disintegrating or degradation of material properties. The mechanical

properties were found to depend on the density, which was controlled by catalyst loading. The stiffness ranged from $1-5MPa$ and the uncompressed resistivity of the bulk material was $0.049 - 0.071\Omega m$. Stress versus volume fraction of the nonwoven carbon nanofibers follows van Wyk's model for a network of random fibers. The resistance behavior of the samples also indicates that the nonwoven carbon behaves as a network of fibers whose number of contacts increases linearly with volume fraction; the resistance of the sample decreases as the compressive strain (volume fraction) increases. This carbon material has many unique properties yet to be explored, but it is expected that the adaptability of the process is likely to enable use in current nonwoven carbon applications (e.g. filtration) as well as new areas.

Chapter 6

Characterization of A Nonwoven Carbon Nanofiber Structure (Large Loads)

6.1 Overview

Entangled networks of carbon nanofibers are characterized both mechanically and electrically. Results for both tensile and compressive loadings of the entangled networks are presented for various densities. Mechanically, the nanofiber ensembles follow the micromechanical model originally proposed by van Wyk nearly 70 years ago. Interpretations are given on the mechanisms occurring during loading and unloading of the carbon nanofiber components.

6.2 Keywords

carbon; entangled; nanofibers

6.3 Introduction

One-dimensional carbon materials are available in many high-end commercial products [17, 23] and continue to be a source of ongoing research [7, 124, 99]. This is due to their remarkable material properties. The two main instances of this type of material are carbon nanotubes and carbon nanofibers. Carbon micro and nanofibers are a common component in high-strength, lightweight fiber-reinforced composites [6, 25, 73]. Less studied are the properties of an interwoven assemblage of the nanofibers, which behaves as a coherent, nonwoven component.

Synthesis methods for creating carbon nanotubes [12] and nanofibers [12, 13, 11] commonly produce random networks of tangled fibers. These entangled fibers do not have fixed connections with adjoining fibers (i.e., they are not cross-linked). Thus, the entangled fibers comprise a random network similar in nature to a nonwoven mass of fibers found in common textile processes. Random networks of textile fibers are commonly modeled using a micromechanical model originally developed by van Wyk in 1946. In 2009 an effort was undertaken to mechanically test a "tangle" of carbon nanotubes [7]. This effort demonstrated that the van Wyk model [125] matched the stress vs. change in fiber volume fraction for the loading portion of the curve. It also showed that the van Wyk model did not match the unloading portion of the curve. Allaoui et al. [7] surmise that this is due to the dissipation of adhesive energy as contacts break.

The van Wyk model was proposed in 1946 [125] and incorporates fiber bending at contact points in the random network and the creation of new fiber-to-fiber contacts,

but ignores other effects such as friction and fiber sliding. Functionally, van Wyk's model proportionally relates the stress applied to the random fiber network, , to the fiber volume fraction, , to the third power:

$$\sigma = k_p \left(\mu^3 - \mu_0^3\right) \tag{6.1}$$

where k_p is a constant that contains information on fiber characteristics and 0 is the initial fiber volume fraction before compression. This model describes the behavior of a large entangled network of randomly oriented fibers. This amazingly simplistic model has been found to be applicable to many different types of random fiber networks such as short hollow pulp fiber networks [75] and textile reinforcements for composites manufacturing [103].

The electrical response of a random fiber network to an applied stress is not commonly studied, because most types of fibers in the textile industry are not conductive. Thus, there is a lack of studies and modeling addressing this topic. In this paper, the electrical properties are measured in both tension and compression. Sudden changes in electrical resistance seen in tension tests can be used as a method of evaluating the mechanical situation and integrity of the material. For compression tests, the electrical resistance is shown to approach the conductance of amorphous carbon when the carbon nanofibers are under their highest compressive loads. Additionally, the mechanical response of the entangled networks of carbon nanofibers is studied in tension and compression. A discussion of the tensile response is qualitative while the compressive response is modeled using the van Wyk Model. The compression tests reported here are performed in an open die configuration under high stresses (10 MPa). During loading, it was verified that the sample kept its integrity even at the highest loads. Furthermore, it is shown that the van Wyk Model Equation (1) for a random entanglement of fibers is capable of describing the response of the material with considerable accuracy.

6.4 Experimental Section

6.4.1 Carbon Nanofiber Synthesis

Bulk, nonwoven components comprised of carbon nanofibers were synthesized using a method previously developed by Atwater et al. [12]. Briefly, Pd nanoparticles are dispersed in a rectangular steel mold and then heated in a furnace in an inert environment. Once heated to $550^{o}C$, a mixture of ethylene and oxygen is flown over the catalyst. By varying the Pd particle loading in the mold and the time of gas flow differing densities of carbon nanofiber entanglements were synthesized. Sample densities were determined geometrically by weighing samples of a known volume.

An example of the as-grown samples is shown in Figure 6.1. Here it can be seen that a relatively large (many centimeters) component can be easily attained with this process. When examined using SEM, it can be seen that the larger structure is actually comprised of much smaller (ca. $100nm$ diameter), carbon nanofibers, e.g., Figure 1d. Additional characterization of the fibers' properties is contained in References [13, 11]. The process, then, creates a multi-scale material with the ability to control both nanoscale and macroscale features.

6.4.2 Mechanical and Electrical Characterization Setups

Mechanical and electrical characterization was conducted simultaneously for samples of differing densities. In order to accomplish this, a custom setup was required for both the tensile and compressive tests. Tensile samples were tested under relatively low loads, $< 45N$, while compression tests were to a load as high as $200N$.

Tensile tests were conducted on an Instron 1101 with a $45N$ load cell using a constant displacement of $1.27mm/min$. Sample densities tested were 0.125 and

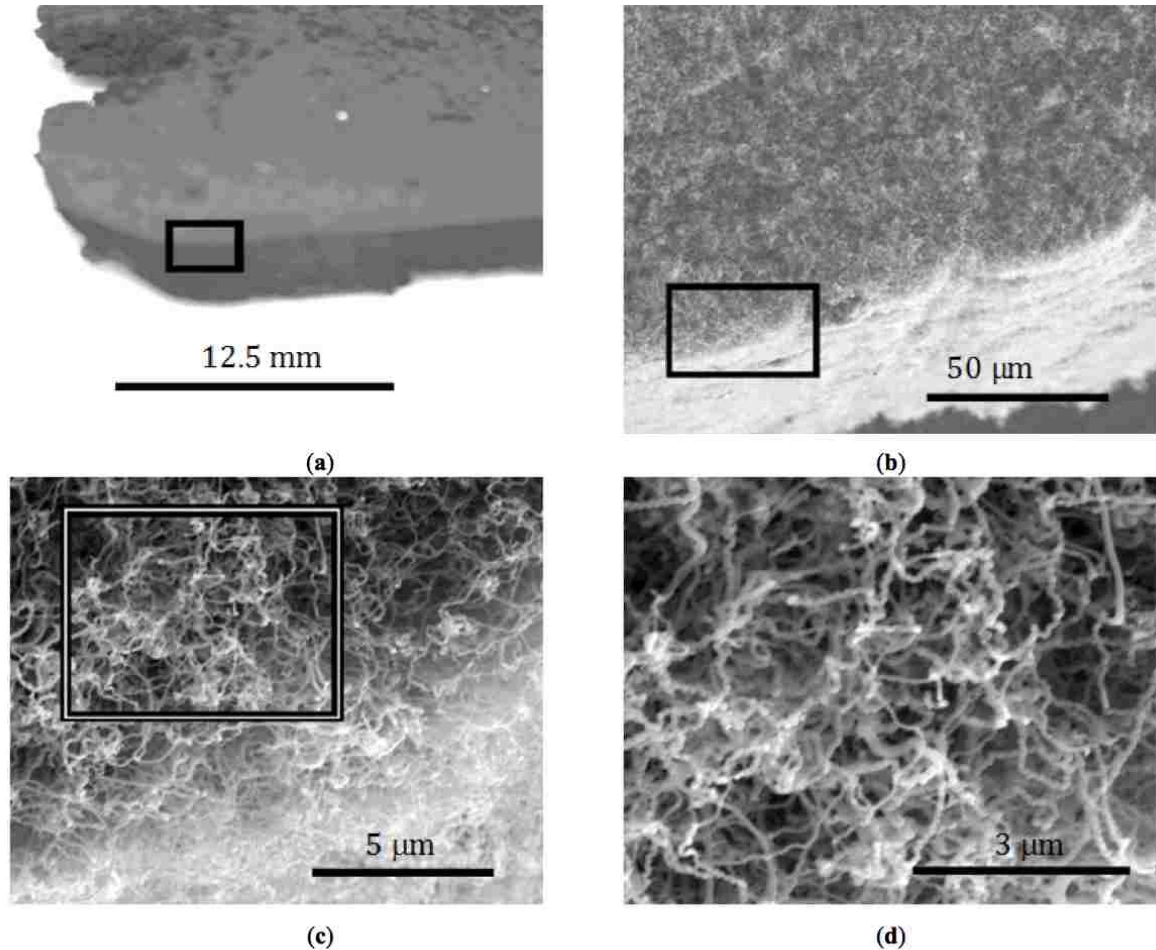

Figure 6.1: Carbon Nanofiber Network at increasing magnification, boxes indicate section in next image (a) 1×; (b) 1000×; (c) 10,000×; (d) 20,000×.

$0.131 g/cc$. Carbon nanofiber samples with a cross sectional area of $5mm \times 25mm$ were clamped between two electrically isolated grips at a distance of 20 mm apart. A constant current of $250mA$ was applied to the samples and the voltage was recorded in order to determine the resistance of the sample as a function of load.

Compression tests were performed on a larger capacity Instron with a $44.5kN$ load cell with a constant crosshead displacement of $0.252mm/min$. The $0.40g/cc$ cylindrical sample was tested in an open die configuration with a diameter of $4.7mm$

and thickness of $5mm$. Electrical measurements were made in the same manner as for the tensile experiments.

6.5 Mechanical Properties

6.5.1 Tensile Tests

Tensile loading curves for two different densities of nanofibrous nonwoven carbon are shown in Figure 6.2. The stress-strain curves are accompanied by their corresponding resistance measurements. Judging from SEM characterization (e.g., see Figure 6.1), no fiber is expected to span the gage length of the sample, and therefore no fibers are considered rigidly held by both grips. On that assumption, loading of the samples must be a result of friction between the fibers and mechanical interlocking.

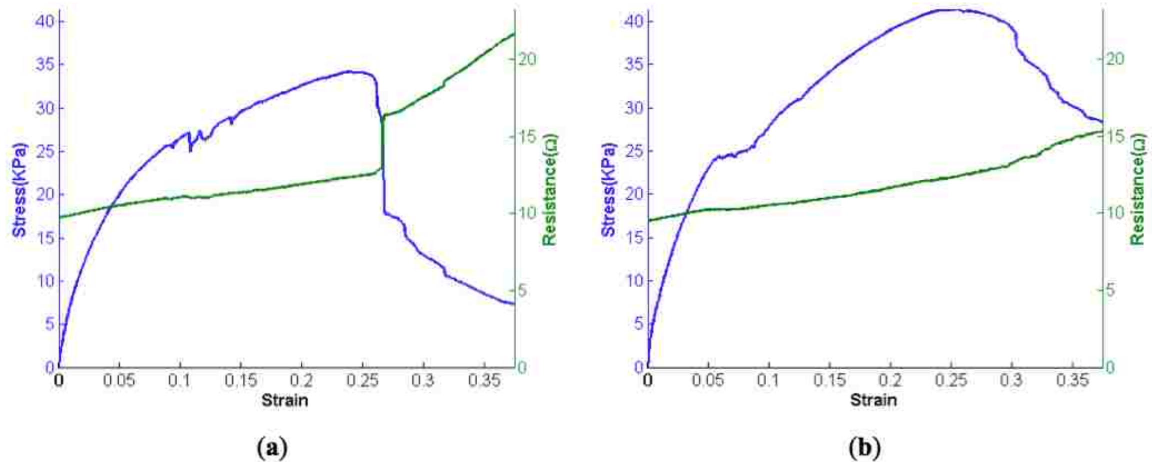

Figure 6.2: Tensile behavior of carbon nanofiber network under tension, accompanied by resistance measurements as a function of strain (mm/mm). (a) Low density network; (b) High density network.

Tensile loading of the samples displays several interesting behaviors. For both

samples, a smooth monotonic increase is seen during loading initially. This smooth portion of the loading curves is then followed by data that is generally increasing, but contains several discontinuities. These discontinuities are attributed to avalanches of fiber pullouts. After a critical number of fibers have pulled out, a maximum load is reached, and any increase in displacement results in nothing but decreases in load.

In order to more succinctly compare the behavior of these two samples five material properties are examined: (1) tangent modulus; (2) maximum stress; (3) maximum strain; (4) failure stress and (5) failure strain. Failure is defined as a decrease in the load sustained by the sample. Table 1 compares the compressive moduli and tangent moduli attained from tensile tests. Though the two samples have nearly identical densities and remarkably similar material properties, as listed in Table 1, there is a marked difference in the failure of the two samples. The $0.125g/cc$ sample has a massive avalanche of pulled out fibers as is evidenced by a sudden drop in load after reaching u; this is also accompanied by a large jump in resistance of the sample. The $0.131g/cc$ sample appears to have a fairly gradual pullout of fibers as it continues to fail after having reached its σ_u.

Table 6.1: Mechanical Properties of entangled network of carbon nanofibers.

$\rho(g/cm^3)$	$E(kPa)$	$\sigma_y(kPa)$	$\sigma_u(kPa)$	Linear Range Percentage($\% of \sigma_u$)
0.125	600	13.4	34.2	39.2%
0.131	627	16.9	41.3	40.8%

The resistance of the entangled network of the carbon nanofibers increases almost linearly with increasing tensile load until there is a sudden drop in the load (stress). This is a clear indication that fibers are pulling out from one another. This reduces the number of fibers in contact as well as the number of contacts per fiber. Once a threshold limit is met, then many fibers separate from one another simultaneously - an avalanche of fiber pullouts. Again, this is most noticeable for the $0.125g/cc$

sample near its σ_u.

6.6 Compression Tests

Five compressive loading cycles are shown for a sample with a of density $0.40g/cc$ in Figure 6.3. Cycle 6 and subsequent cycles display the similar hysteresis between the loading and unloading portion of each cycle, but nearly fall on top of one another. The stress versus percent fiber volume fraction ($mu\%$) are accompanied by their corresponding resistance measurements. The resistance vs. $mu\%$ curves follow similar trends, as seen by Atwater et al. [13]. Additionally, the loading portions of the curves in Figure 6.3 are fit with the van Wyk model, Equation (5.1). The agreement between the experimental data and model demonstrate the utility of the model and also show that the mechanisms modeled in the van Wyk interpretation are responsible for the deformation behavior of the entanglement of the carbon nanofibers.

van Wyk's model describes the bending and creation of new contacts in a random network of fibers. This is appropriate for the compressive loading of the fibers as evidenced by the fit of van Wyk's model to the data in Figure 6.4. Unloading of the fiber shows a considerable amount of hysteresis and is not modeled well by van Wyk's model (and is not displayed). For unloading, it is likely that adhesion and friction are the main contributors to this hysteresis, as is the case with carbon nanotubes [7].

Even within the loading event, it appears that bending and the creation of contacts contribute different amounts to the loading history of the sample as the fiber volume fraction increases. For lower values of μ (and load) the samples are more porous, i.e., there are more air gaps between the carbon nanofibers. Thus, as the sample is compressed, the fibers bend into the empty spaces more readilybending is more dominant at lower values of load and . Thus, the model does not work as well for lower values of load and . As the compression continues, new contacts are made

at an increasing rate. In fact, it has been recently shown that the rate of increase of the number of contacts is linearly proportional to μ [104]. Thus for higher values of load and the van Wyk model is more applicable and therefore more accurate. A considerable amount of hysteresis exists between the loading and unloading cycles in Figure 3. Adhesion (friction) is attributed to this hysteresis. Adhesive forces are commonly known to cause sticking between individual micro and nanodevices, commonly referred to as 'stiction failure' in the literature [86, 69, 31]. Because of the small scale of the fibers (i.e., ca. 100 nm diameter), van der Waals forces, hydrogen bonding, etc. may have an appreciable adhesive effect. Allaoui et al. [7] also consider this to be the source of adhesion between fibers and the culprit for hysteresis in carbon nanotube tangles.

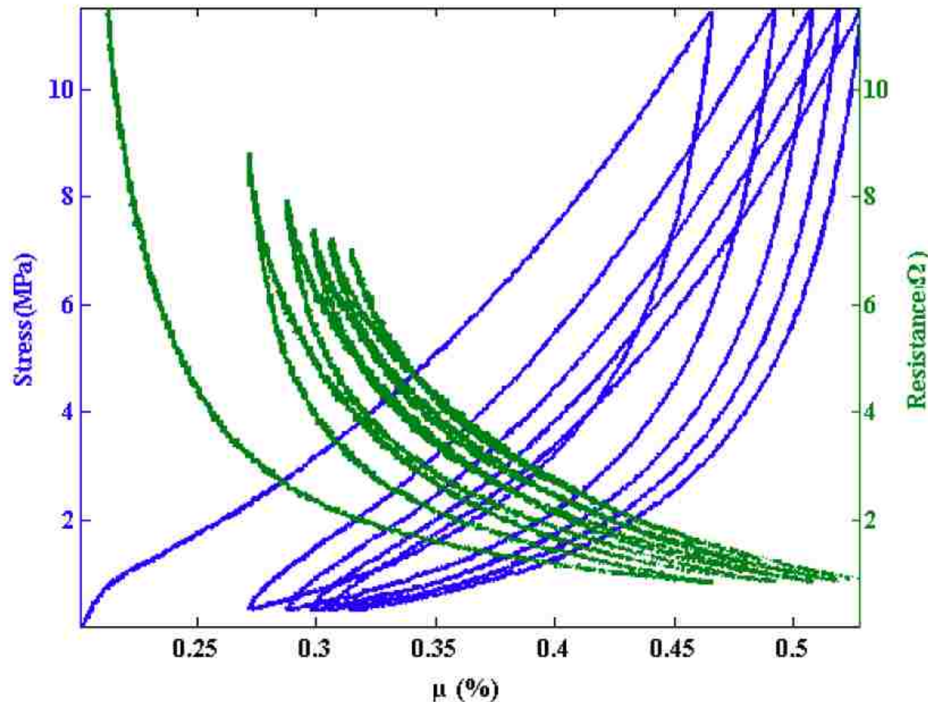

Figure 6.3: Five compression cycles (continuous loading and unloading) of a $0.40 g/cc$ carbon nanofiber tangle sample. Data is displayed as pressure vs. percent fiber volume fraction (μ).

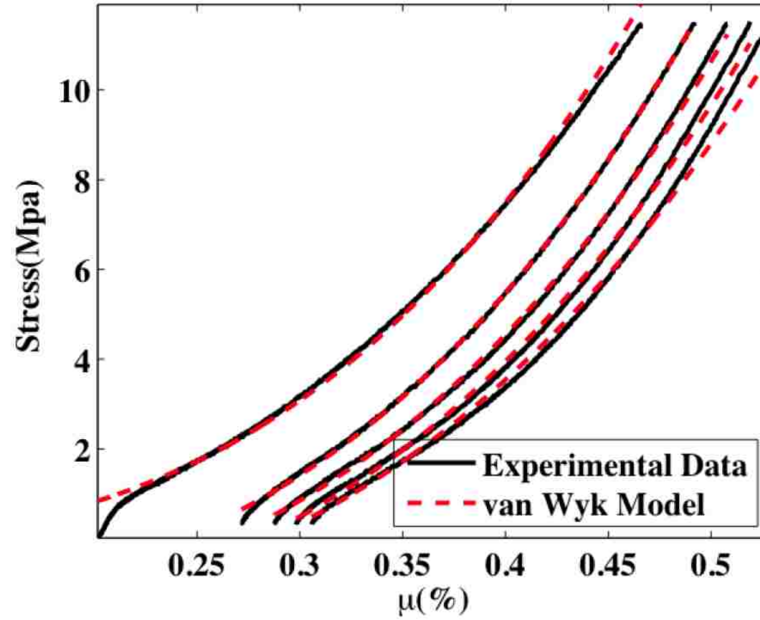

Figure 6.4: Loading portions of the curves in Figure 3 with fits to the van Wyk model.

Adhesion between fibers leads to hysteresis while the bending of individual fibers is the main source of elastic energy storage. As the load increases more fibers are being influenced to move, but their motion is impeded due to restrictions from adjacent fibers. For the highest loads, energy is dissipated by irreversible friction and sliding [118]. However, when unloading occurs, only the elastically stored energy can be recovered. Thus a small reverse movement in the compression platen results in a large drop in load as seen in all unloading curves. For lower values of μ (strain) the elastic energy in the fibers becomes considerable and pushes back on the compression platen and a large movement of the platen results in a smaller change in load.

The resistance of the entangled network decreases nonlinearly as the compressive load is applied in Figure 3. An asymptotic value is approached for the highest loads. Considering the sample size, the resistivity of the sample approaches $2.7 \times 10^{-3}\Omega m$, which is approximately three to five times that of amorphous carbon $(5 \times 10^{-4} - 8 \times$

$10^{-4}\Omega m$) [113, 92]. Physically, the sample is being compressed and the sizes of the pores filled with air are beginning to decrease while, simultaneously, more physical connections are being made between fibers. Had all pores been eliminated, it would be expected that the value for the resistivity of the material should approach that of amorphous carbon. However, it can never truly reach this value because the pores never fully disappear and also the surfaces of the carbon nanofibers have adsorbed gases that never allow the entangled network of carbon nanofibers to turn into a continuous piece of amorphous carbon. These interfaces cause additional scattering of electrons over what would be expected in amorphous carbon.

6.7 Conclusions

The results of this work indicate that bulk collections of carbon nanofibers can behave as traditional nonwoven materials. This understanding was reached through simultaneous mechanical and electrical analyses. Under tensile load, these nanofibrous nonwovens tend to fail by fiber pullout. During elongation there is no significant enhancement of fiber-to-fiber contact (i.e., reduction of cross-sectional area) which would be indicated through a reduction in electrical resistance. Under compression, the material behaves elastically, but with significant hysteresis during unloading. Electrical resistance decreases substantially as the material is compressed. The mechanical properties and the reduction in electrical resistance are consistent with the van Wyk model of fiber interaction. The hysteresis during unloading is attributable to small-scale friction and adhesive affects found in fibrous materials. Based on these data, the material is expected to be suitable for applications where cyclic compressive forces are encountered or in applications where an electrical response to deformation may be valuable.

References

[1] Khawar Abbas, *Design fabrication and calibration of MEMS actuators for in-situ materials testing*, Ph.D. thesis, University of New Mexico, December 2008.

[2] Khawar Abbas, Zayd C Leseman, and Thomas J Mackin, *A traceable calibration procedure for MEMS-based load cells*, International Journal of Mechanics and Materials in Design **4** (2008), no. 4, 383–389.

[3] T. Abe, W.C. Messner, and M.L. Reed, *Effective methods to prevent stiction during post-release-etch processing*, Proceedings IEEE Micro Electro Mechanical Systems. 1995, IEEE, 1995, p. 94.

[4] Pulickel Ajayan, Alvaro Carrillo, Nirupama Chakrapani, Ravindra S. Kane, and Bingqing Wei, *Carbon nanotube foam and method of making and using thereof*, May 2009.

[5] Teronobu Akiyama, Dominique Collard, and Hiroyuki Fujita, *Scratch drive actuator with mechanical links for self-assembly of three-dimensional MEMS*, Microelectromechanical Systems, Journal of **6** (1997), no. 1, 10–17.

[6] A. Alipour Skandani, N. Masghouni, S. W. Case, D. J. Leo, and M. Al-Haik, *Enhanced vibration damping of carbon fibers-ZnO nanorods hybrid composites*, Applied Physics Letters **101** (2012), no. 7, 073111.

[7] Aïssa Allaoui, Staffan Toll, Pierre Evesque, and JB Bai, *On the compressive response of carbon nanotube tangles*, Physics Letters A **373** (2009), no. 35, 3169–3173.

[8] W.R. Ashurst, C. Carraro, and R. Maboudian, *Vapor phase anti-stiction coatings for MEMS*, IEEE Transactions on Device and Materials Reliability **3** (2003), no. 4, 173–178 (English).

[9] W.R. R Ashurst, C. Yau, C. Carraro, R. Maboudian, and M.T. T Dugger, *Dichlorodimethylsilane as an anti-stiction monolayer for MEMS: a comparison to the octadecyltrichlorosilane self-assembled monolayer*, Journal of Microelectromechanical Systems **10** (2001), no. 1, 41–49.

[10] W.Robert Ashurst, Christina Yau, Carlo Carraro, Christina Lee, G.Jonathan Kluth, Roger T Howe, and Roya Maboudian, *Alkene based monolayer films as anti-stiction coatings for polysilicon MEMS*, Sensors and Actuators A: Physical **91** (2001), no. 3, 239–248.

[11] Mark Atwater, Zayd C. ZC Leseman, and Jonathan Phillips, *Controlling carbon nanofibre morphology for improved composite reinforcement*, International Journal of Materials and Structural Integrity **3** (2009), no. 2/3, 179–186.

[12] Mark A. Atwater, Arash K. Mousavi, Zayd C. Leseman, and Jonathan Phillips, *Direct synthesis and characterization of a nonwoven structure comprised of carbon nanofibers*, Carbon **57** (2013), 363–370.

[13] Mark A. Atwater, Jonathan Phillips, Stephen K. Doorn, Claudia C. Luhrs, Y. Fernández, J.a. Menéndez, and Zayd C. Leseman, *The production of carbon nanofibers and thin films on palladium catalysts from ethyleneoxygen mixtures*, Carbon **47** (2009), no. 9, 2269–2280.

[14] Mark A. Atwater, Jonathan Phillips, and Zayd C. Leseman, *Formation of Carbon Nanofibers and Thin Films Catalyzed by Palladium in EthyleneHydrogen Mixtures*, The Journal of Physical Chemistry C **114** (2010), no. 13, 5804–5810.

[15] ———, *The effect of powder sintering on the palladium-catalyzed formation of carbon nanofibers from ethyleneoxygen mixtures*, Carbon **48** (2010), no. 7, 1932–1938.

[16] ———, *Accelerated growth of carbon nanofibers using physical mixtures and alloys of Pd and Co in an ethylenehydrogen environment*, Carbon **49** (2011), no. 4, 1058–1066.

[17] A Bachtold, P Hadley, T Nakanishi, and C Dekker, *Logic circuits with carbon nanotube transistors.*, Science (New York, N.Y.) **294** (2001), no. 5545, 1317–20.

[18] K. Baghbani Parizi, N. Peyvast, B. Kheyraddini Mousavi, S. Mohajerzadeh, and M. Fathipour, *Schottky barrier nano-MOSFET with an asymmetrically oxidized source/drain structure*, Solid-State Electronics **54** (2010), no. 1, 48–51.

[19] Hassan Bagher-Ebadian, Quan Jiang, and James R Ewing, *A modified Fourier-based phase unwrapping algorithm with an application to MRI venography.*, Journal of magnetic resonance imaging : JMRI **27** (2008), no. 3, 649–52.

[20] R. Ballarini, R. L. Mullen, Y. Yin, H. Kahn, S. Stemmer, and A. H. Heuer, *The Fracture Toughness of Polysilicon Microdevices: A First Report*, Journal of Materials Research **12** (2011), no. 04, 915–922 (English).

[21] Rajneeta R Basantkumar, B J Hills Stadler, William P Robbins, and Eric M Summers, *Integration of thin-film galfenol with MEMS cantilevers for magnetic actuation*, Magnetics, IEEE Transactions on **42** (2006), no. 10, 3102–3104.

[22] Subhash Kumar Batra and Behnam Pourdeyhimi, *Introduction to Nonwovens Technology*, DEStech Publications, Inc, 2012.

[23] Ray H Baughman, Anvar a Zakhidov, and Walt a de Heer, *Carbon nanotubes–the route toward applications.*, Science (New York, N.Y.) **297** (2002), no. 5582, 787–92.

[24] C.K. Bora, E.E. Flater, M.D. Street, J.M. Redmond, M.J. Starr, R.W. Carpick, and M.E. Plesha, *Multiscale roughness and modeling of MEMS interfaces*, Tribology Letters **19** (2005), no. 1, 37–48.

[25] M. B. Bryning, M. F. Islam, J. M. Kikkawa, and a. G. Yodh, *Very Low Conductivity Threshold in Bulk Isotropic Single-Walled Carbon Nanotube-Epoxy Composites*, Advanced Materials **17** (2005), no. 9, 1186–1191.

[26] Shuiliang Chen, Haoqing Hou, Falk Harnisch, Sunil A. Patil, Alessandro A. Carmona-Martinez, Seema Agarwal, Yiyun Zhang, Suman Sinha-Ray, Alexander L. Yarin, Andreas Greiner, and Uwe Schröder, *Electrospun and solution blown three-dimensional carbon fiber nonwovens for application as electrodes in microbial fuel cells*, Energy & Environmental Science **4** (2011), no. 4, 1417 (en).

[27] G. S. Chung, S. M. Jo, and B. C. Kim, *Properties of carbon nanofibers prepared from electrospun polyimide*, Journal of Applied Polymer Science **97** (2005), no. 1, 165–170.

[28] W. T. Davis, G. D. Kim, and T. C. Perry, *STUDY OF THE ADSORPTION/REMOVAL EFFICIENCY OF WOVEN AND NONWOVEN ACTIVATED CARBON FABRICS FOR MEK*, Separation Science and Technology **36** (2001), no. 5-6, 931–940.

[29] M P de Boer, P J Clews, B K Smith, and T A Michalske, *Adhesion of Polysilicon Microbeams in Controlled Humidity Ambients*, Symposium N Microelectromechanical Structures for Materials Research, MRS Proceedings, vol. 518, 1998.

[30] M P de Boer and P C T de Boer, *Thermodynamics of capillary adhesion between rough surfaces.*, Journal of colloid and interface science **311** (2007), no. 1, 171–85.

[31] M. P. de Boer and T. A. Michalske, *Accurate method for determining adhesion of cantilever beams*, Journal of Applied Physics **86** (1999), no. 2, 817.

[32] KRIJN P. DE JONG and JOHN W. GEUS, *Carbon Nanofibers: Catalytic Synthesis and Applications*, Catalysis Reviews **42** (2000), no. 4, 481–510.

[33] M.P. DeBoer, D.L. Luck, W.R. Ashurst, R. Maboudian, A.D. Corwin, J.A. Walraven, and J.M. Redmond, *High-Performance Surface-Micromachined Inchworm Actuator*, Journal of Microelectromechanical Systems **13** (2004), no. 1, 63–74.

[34] Frank W Delrio, Maarten P de Boer, James A Knapp, E David Reedy, Peggy J Clews, and Martin L Dunn, *The role of van der Waals forces in adhesion of micromachined surfaces.*, Nature materials **4** (2005), no. 8, 629–34.

[35] Frank W. DelRio, Martin L. Dunn, Brad L. Boyce, Alex D. Corwin, and Maarten P. de Boer, *The effect of nanoparticles on rough surface adhesion*, Journal of Applied Physics **99** (2006), no. 10, 104304.

[36] Jana Dittmann, Lucilla Croce Ferri, and Claus Vielhauer, *Hologram watermarks for document authentications*, Information Technology: Coding and Computing, International Conference on, IEEE Computer Society, 2001, p. 60.

[37] J. I. Dunlop, *CHARACTERIZING THE COMPRESSION PROPERTIES OF FIBRE MASSES*, Journal of the Textile Institute **65** (1974), no. 10, 532–536.

[38] H L Ewalds and R J H Wanhill, *Fracture Mechanics (Edward Arnold, London, 1984)*.

[39] Richard P Feynman, *There's plenty of room at the bottom*, Engineering and science **23** (1960), no. 5, 22–36.

[40] R Frisch-Fay and R. Frisch-Fay, *Flexible Bars*, Butterworths, 1962.

[41] Nidia C Gallego and James W Klett, *Carbon foams for thermal management*, Carbon **41** (2003), no. 7, 1461–1466.

[42] Phil Gibson and Calvin Lee, *Application of nanofiber technology to nonwoven thermal insulation*, Tech. report, DTIC Document, 2006.

[43] John J Gill, Ken Ho, and Greg P Carman, *Three-dimensional thin-film shape memory alloy microactuator with two-way effect*, Microelectromechanical Systems, Journal of **11** (2002), no. 1, 68–77.

[44] Martin A Green and Mark J Keevers, *Optical properties of intrinsic silicon at 300 K*, Progress in Photovoltaics: Research and Applications **3** (1995), no. 3, 189–192.

[45] H Guckel, J J Sniegowski, T R Christenson, and F Raissi, *The application of fine-grained, tensile polysilicon to mechanicaly resonant transducers*, 1990, pp. 346–351.

[46] V. Gupta, R. Snow, M.C. Wu, A. Jain, and J.-C. Tsai, *Recovery of Stiction-Failed MEMS Structures Using Laser-Induced Stress Waves*, Journal of Microelectromechanical Systems **13** (2004), no. 4, 696–700.

[47] Parameswaran Hariharan, *Basics of holography*, Cambridge University Press, 2002.

[48] Jacob Israelachvili, *Intermolecular & Surface Forces*, Academic Press, 2006.

[49] S. Jaganathan, H. Vahedi Tafreshi, E. Shim, and B. Pourdeyhimi, *A study on compression-induced morphological changes of nonwoven fibrous materials*, Colloids and Surfaces A: Physicochemical and Engineering Aspects **337** (2009), no. 1-3, 173–179.

[50] Edward E Jones, Matthew R Begley, and Kevin D Murphy, *Adhesion of micro-cantilevers subjected to mechanical point loading: modeling and experiments*, Journal of the Mechanics and Physics of Solids **51** (2003), no. 8, 1601–1622.

[51] S. Kamisuki, M. Fujii, T. Takekoshi, C. Tezuka, and M. Atobe, *A High Resolution, Electronically-Driven Commercial Inkjet Head*, IEEE (2000).

[52] Inpil Kang, Yun Yeo Heung, Jay H. Kim, Jong Won Lee, Ramanand Gollapudi, Srinivas Subramaniam, Suhasini Narasimhadevara, Douglas Hurd, Goutham R. Kirikera, Vesselin Shanov, Mark J. Schulz, Donglu Shi, Jim Boerio, Shankar Mall, and Marina Ruggles-Wren, *Introduction to carbon nanotube and nanofiber smart materials*, Composites Part B: Engineering **37** (2006), no. 6, 382–394.

[53] Inpil Kang, Mark J Schulz, Jay H Kim, Vesselin Shanov, and Donglu Shi, *A carbon nanotube strain sensor for structural health monitoring*, Smart Materials and Structures **15** (2006), no. 3, 737–748.

[54] F. Karbassian, B. Kheyraddini Mousavi, S. Rajabali, R. Talei, S. Mohajerzadeh, and E. Asl-Soleimani, *Formation of Luminescent Silicon Nanowires and Porous Silicon by Metal-Assisted Electroless Etching*, Journal of Electronic Materials **43** (2014), no. 4, 1271–1279.

[55] Maheshwar R. Kashamolla, Drew F. Goettler, Arash K. Mousavi, and Zayd C. Leseman, *Mode II Measurements for Stiction Failed MEMS Devices*, Volume 10: Micro and Nano Systems, ASME, January 2010, pp. 63–69.

[56] Maheshwar R. Kashamolla, Arash K. Mousavi, and Zayd C. Leseman, *Mode I and Mixed Mode I and II Measurements for Stiction Failed MEMS Devices*, Volume 12: Micro and Nano Systems, Parts A and B, ASME, January 2009, pp. 25–31.

[57] Satinderpal Kaur, Renuga Gopal, Wun Jern Ng, Seeram Ramakrishna, and Takeshi Matsuura, *Next-Generation Fibrous Media for Water Treatment*, MRS Bulletin **33** (2011), no. 01, 21–26 (English).

[58] B J Kim, M Liebau, J Huskens, D N Reinhoudt, and J Brugger, *A self-assembled monolayer-assisted surface microfabrication and release technique*, Microelectronic Engineering **57-58** (2001), 755–760.

[59] Hareesh K R Kommepalli, Han G Yu, Christopher L Muhlstein, Susan Trolier-McKinstry, Christopher D Rahn, and Srinivas A Tadigadapa, *Design, fabrication, and performance of a piezoelectric uniflex microactuator*, Microelectromechanical Systems, Journal of **18** (2009), no. 3, 616–625.

[60] Sai B. Koppaka and Leslie M. Phinney, *Laser Repair Process Yields for MEMS Devices Adhered During Release or Operation*, Microelectromechanical Systems, vol. 2003, ASME, January 2003, pp. 141–147.

[61] R. Kozlowski, B. Mieleniak, M. Muzyczek, and A. Kubacki, *Flexible fire barriers based on natural nonwoven textiles*, Fire and Materials **26** (2002), no. 4-5, 243–246.

[62] F Larmer and A Schilp, *Method for anisotropically etching silicon*, 1992.

[63] Brian R Lawn, *Fracture of brittle solids*, Cambridge university press, 1993.

[64] Jinwoo Lee, Sangjin Han, and Taeghwan Hyeon, *Synthesis of new nanoporous carbon materials using nanostructured silica materials as templates*, Journal of Materials Chemistry **14** (2004), no. 4, 478 (en).

[65] Rob Legtenberg, A W Groeneveld, and M Elwenspoek, *Comb-drive actuators for large displacements*, Journal of Micromechanics and microengineering **6** (1996), no. 3, 320.

[66] Rob Legtenberg, Harrie A.C. Tilmans, Job Elders, and Miko Elwenspoek, *Stiction of surface micromachined structures after rinsing and drying: model and investigation of adhesion mechanisms*, Sensors and Actuators A: Physical **43** (1994), no. 1-3, 230–238.

[67] Z C Leseman, *A Novel method for testing freestanding nanofilms using a custom MEMS load cell*, Ph.D. thesis, University of Illinois at Urbana-Champaign, 2006.

[68] Zayd C. Leseman, Steven Carlson, Xiaojie Xue, and Thomas J. Mackin, *A Standard Approach for Measuring Adhesion Energies in Stiction-Failed Microdevices*, Microelectromechanical Systems, vol. 2006, ASME, January 2006, pp. 5–13.

[69] Zayd C. Leseman, Steven P. Carlson, and Thomas J. Mackin, *Experimental Measurements of the Strain Energy Release Rate for Stiction-Failed Microcantilevers Using a Single-Cantilever Beam Peel Test*, Journal of Microelectromechanical Systems **16** (2007), no. 1, 38–43 (English).

[70] Zayd C. Leseman, Sai Koppaka, and Thomas J. Mackin, *A Fracture Mechanics Model for the Repair of Microcantilevers by Laser Induced Stress Waves*, Microelectromechanical Systems, vol. 2005, ASME, January 2005, pp. 353–357.

[71] Zayd C. Leseman, Sai B. Koppaka, and Thomas J. Mackin, *A Fracture Mechanics Description of Stress-Wave Repair in Stiction-Failed Microcantilevers: Theory and Experiments*, Journal of Microelectromechanical Systems **16** (2007), no. 4, 904–911 (eng).

[72] Sizhong Li, Yongzhong Song, Yan Song, Jingli Shi, Lang Liu, Xinghai Wei, and Quangui Guo, *Carbon foams with high compressive strength derived from mixtures of mesocarbon microbeads and mesophase pitch*, Carbon **45** (2007), no. 10, 2092–2097.

[73] WQ Li, HB Zhang, and Xiang Xiong, *Properties of multi-walled carbon nanotube reinforced carbon foam composites*, Journal of Materials Science **46** (2011), no. 4, 1143–1146.

[74] K. M. Liechti and W. G. Knauss, *Crack propagation at material interfaces: II experiments on mode interaction*, Experimental Mechanics **22** (1982), no. 10, 383–391.

[75] L Lundquist and F Willi, *Compression behavior of pulp fiber networks*, Polymer Engineering & . . . **44** (2004), no. 1, 45–55.

[76] Roya Maboudian, W.Robert Ashurst, and Carlo Carraro, *Self-assembled monolayers as anti-stiction coatings for MEMS: characteristics and recent developments*, Sensors and Actuators A: Physical **82** (2000), no. 1-3, 219–223.

[77] Marc J Madou, *Fundamentals of microfabrication: the science of miniaturization*, CRC press, 2002.

[78] F.J. Maldonado-Hódar, M.A. Ferro-Garca, J. Rivera-Utrilla, and C. Moreno-Castilla, *Synthesis and textural characteristics of organic aerogels, transition-metal-containing organic aerogels and their carbonized derivatives*, Carbon **37** (1999), no. 8, 1199–1205.

[79] P.F. Man, B.P. Gogoi, and C.H. Mastrangelo, *Elimination of post-release adhesion in microstructures using conformal fluorocarbon coatings*, Journal of Microelectromechanical Systems **6** (1997), no. 1, 25–34.

[80] C.H. Mastrangelo and C.H. Hsu, *A simple experimental technique for the measurement of the work of adhesion of microstructures*, Technical Digest IEEE Solid-State Sensor and Actuator Workshop, IEEE, 1992, pp. 208–212.

[81] ———, *Mechanical stability and adhesion of microstructures under capillary forces. I. Basic theory*, Journal of Microelectromechanical Systems **2** (1993), no. 1, 33–43 (English).

[82] ———, *Mechanical stability and adhesion of microstructures under capillary forces. II. Experiments*, Journal of Microelectromechanical Systems **2** (1993), no. 1, 33–43.

[83] D. Maugis, *On the contact and adhesion of rough surfaces*, Journal of Adhesion Science and Technology **10** (1996), no. 2, 161–175.

[84] Jie Meng, Li Song, Hua Kong, Guangjin Zhu, Chaoying Wang, Lianghua Xu, Sishen Xie, and Haiyan Xu, *Using single-walled carbon nanotubes nonwoven films as scaffolds to enhance long-term cell proliferation in vitro.*, Journal of biomedical materials research. Part A **79** (2006), no. 2, 298–306.

[85] C. Moreno-Castilla and F.J. Maldonado-Hódar, *Carbon aerogels for catalysis applications: An overview*, Carbon **43** (2005), no. 3, 455–465.

[86] a K Mousavi, M R Kashamolla, and Z C Leseman, *Improved model for the adhesion of μcantilevers: theory and experiments*, Journal of Micromechanics and Microengineering **23** (2013), no. 11, 115011.

[87] Arash Mousavi, Mark Atwater, Behnam Mousavi, Mohammad Jalalpour, Mahmoud Taha, and Zayd Leseman, *Mechanical and Electrical Characterization of Entangled Networks of Carbon Nanofibers*, Materials **7** (2014), no. 6, 4845–4853.

[88] Arash Kheyraddini Mousavi, Khawar Abbas, Mirza Mohammad Mahbube Elahi, Edidson Lima, Stephen Moya, Joseph Daniel Butner, Denise Piñon, Adeeko Benga, Behnam Kheyraddini Mousavi, and Zayd Chad Leseman, *Pulsed vacuum and etching systems: Theoretical design considerations for a pulsed vacuum system and its application to XeF2 etching of Si*, Vacuum **109** (2014), 216–222.

[89] Arash Kheyraddini Mousavi, Seyedhamidreza Alaie, Maheshwar R. Kashamolla, and Zayd Chad Leseman, *Nonlinear Approach for Strain Energy Release Rate in Micro Cantilevers*, Volume 10: Micro and Nano Systems, ASME, January 2010, pp. 51–56.

[90] Arash Kheyraddini Mousavi and Zayd Chad Leseman, *Basic MEMS Actuators*, Encyclopedia of Nanotechnology, Springer, 2012, pp. 173–185.

[91] G. T. Mulhern, D. S. Soane, and R. T. Howe, *Supercritical carbon dioxide drying of microstructures*, In Proc. 7th Int. Conf. Solid-State Sensors and Actuators (Transducers 93), 1993, pp. 7–10.

[92] Y Pauleau and PB Barna, *Protective Coatings and Thin Films: Synthesis, Characterization, and Applications*, Springer Science & Business Media, 1996.

[93] Michael Peck, *Interferometry mathematics, algorithms, and data*, (2010).

[94] ———, *Some comments on Vargas et al.s Phase-shifting interferometry based on principal components analysis*, (2012).

[95] D. R. Petterson, *Mechanics of Nonwoven Fabrics*, Industrial & Engineering Chemistry **51** (1959), no. 8, 902–903.

[96] Jonathan Phillips, Toshi Shiina, Martin Nemer, and Kelvin Lester, *Graphitic structures by design.*, Langmuir : the ACS journal of surfaces and colloids **22** (2006), no. 23, 9694–703.

[97] N. A. Prokudina, E. R. Shishchenko, O.-S. Joo, D. Y. Kim, and S. H. Han, *Carbon Nanotube RLC Circuits*, Advanced Materials **12** (2000), no. 19, 1444–1447.

[98] Long Que, Jae-Sung Park, and Yogesh B Gianchandani, *Bent-beam electrothermal actuators-Part I: Single beam and cascaded devices*, Microelectromechanical Systems, Journal of **10** (2001), no. 2, 247–254.

[99] Sameer S. Rahatekar, Krzysztof K. Koziol, Steven R. Kline, Erik K. Hobbie, Jeffrey W. Gilman, and Alan H. Windle, *Length-Dependent Mechanics of Carbon-Nanotube Networks*, Advanced Materials **21** (2009), no. 8, 874–878.

[100] I. Rajzer, J. Grzybowska-Pietras, and J. Janicki, *Fabrication of Bioactive Carbon Nonwovens for Bone Tissue Regeneration*, Fibres & Textiles in Eastern Europe **Nr 1(84)** (2011), 66–72.

[101] Amit Rawal, P. V. Kameswara Rao, Stephen Russell, and Arjun Jeganathan, *Effect of fiber orientation on pore size characteristics of nonwoven structures*, Journal of Applied Polymer Science **118** (2010), no. 5, 2668–2673.

[102] W Robert Ashurst, M P de Boer, C Carraro, and R Maboudian, *An investigation of sidewall adhesion in MEMS*, Applied Surface Science **212-213** (2003), 735–741.

[103] Francois Robitaille and Raymond Gauvin, *Compaction of textile reinforcements for composites manufacturing. III: Reorganization of the fiber network*, Polymer Composites **20** (1999), no. 1, 48–61.

[104] David Rodney, Marc Fivel, and Rémy Dendievel, *Discrete Modeling of the Mechanics of Entangled Materials*, Physical Review Letters **95** (2005), no. 10, 108004.

[105] N.M. Rodriguez, *A review of catalytically grown carbon nanofibers*, Journal of Materials Research **8** (2011), no. 12, 3233–3250 (English).

[106] J.W. Rogers, T.J. Mackin, and L.M. Phinney, *A thermomechanical model for adhesion reduction of MEMS cantilevers*, Journal of Microelectromechanical Systems **11** (2002), no. 5, 512–520.

[107] A.D Romig, Michael T Dugger, and Paul J McWhorter, *Materials issues in microelectromechanical devices: science, engineering, manufacturability and reliability*, Acta Materialia **51** (2003), no. 19, 5837–5866.

[108] J Rupp, *Drylaid nonwovens*, Textile World (2008), 32–34.

[109] E Sarajlic, J W Berenschot, H Fujita, G J M Krijnen, and M C Elwenspoek, *Bidirectional electrostatic linear shuffle motor with two degrees of freedom*, (2005), 391–394.

[110] Amit A. Savkar, Kevin D. Murphy, Zayd C. Leseman, Thomas J. Mackin, and Matthew R. Begley, *On the Use of Structural Vibrations to Release Stiction Failed MEMS*, Journal of Microelectromechanical Systems **16** (2007), no. 1, 163–173.

[111] Marvin a. Schofield and Yimei Zhu, *Fast phase unwrapping algorithm for interferometric applications*, Optics Letters **28** (2003), no. 14, 1194.

[112] Volker Seidemann, Sebastian Bütefisch, and Stephanus Büttgenbach, *Fabrication and investigation of in-plane compliant SU8 structures for MEMS and their application to micro valves and micro grippers*, Sensors and Actuators A: Physical **97** (2002), 457–461.

[113] R.A. Serway and J.W. Jewett, *Principles of Physics*, 2nd ed., Saunders College Pub: Philadelphia, USA, 1998.

[114] Kevin A Shaw, Z Lisa Zhang, and Noel C MacDonald, *SCREAM I: a single mask, single-crystal silicon, reactive ion etching process for microelectromechanical structures*, Sensors and Actuators A: Physical **40** (1994), no. 1, 63–70.

[115] A Alipour Skandani, N Masghouni, and M Al-Haik, *Superior Damping of Hybrid Carbon Fiber Composites Grafted by ZnO Nanorods*, Topics in Modal Analysis, Volume 7, Springer, 2014, pp. 187–193.

[116] J. J. Sniegowski and M. P. de Boer, *IC-COMPATIBLE P OLYSILICON S URFACE M ICROMACHINING*, Annual Review of Materials Science **30** (2000), no. 1, 299–333 (en).

[117] L. Song, L. Ci, L. Lv, Z. Zhou, X. Yan, D. Liu, H. Yuan, Y. Gao, J. Wang, L. Liu, X. Zhao, Z. Zhang, X. Dou, W. Zhou, G. Wang, C. Wang, and S. Xie, *Direct Synthesis of a Macroscale Single-Walled Carbon Nanotube Non-Woven Material*, Advanced Materials **16** (2004), no. 17, 1529–1534.

[118] Gopinath Subramanian and Catalin R. Picu, *Mechanics of three-dimensional, nonbonded random fiber networks*, Physical Review E **83** (2011), no. 5, 056120.

[119] Marc Sulfridge, Taher Saif, Norman Miller, and Keith O'Hara, *Optical actuation of a bistable MEMS*, Microelectromechanical Systems, Journal of **11** (2002), no. 5, 574–583.

[120] Mitsuo Takeda, Hideki Ina, and Seiji Kobayashi, *Fourier-transform method of fringe-pattern analysis for computer-based topography and interferometry*, JosA **72** (1982), no. 1, 156.

[121] William C Tang, T-CH Nguyen, and Roger T Howe, *Laterally driven polysilicon resonant microstructures*, Micro Electro Mechanical Systems, 1989, Proceedings, An Investigation of Micro Structures, Sensors, Actuators, Machines and Robots. IEEE, IEEE, 1989, pp. 53–59.

[122] D.M. Tanner, T.B. Parson, A.D. Corwin, J.A. Walraven, J.W. Wittwer, B.L. Boyce, and S.R. Winzer, *Science-based MEMS reliability methodology*, Microelectronics Reliability **47** (2007), no. 9-11, 1806–1811.

[123] Thorlabs, *Thorlabs Inc.*

[124] E.T. Thostenson and T.-W. Chou, *Carbon Nanotube Networks: Sensing of Distributed Strain and Damage for Life Prediction and Self Healing*, Advanced Materials **18** (2006), no. 21, 2837–2841.

[125] C M Van Wyk, *A study of the compressibility of wool, with special reference to South African merino wool.*, March 1946, pp. 99–226.

[126] C. M. van Wyk, *NOTE ON THE COMPRESSIBILITY OF WOOL*, Journal of the Textile Institute Transactions **37** (1946), no. 12, T285–T292.

[127] V. Volkov and Y. Zhu, *Phase Imaging and Nanoscale Currents in Phase Objects Imaged with Fast Electrons*, Physical Review Letters **91** (2003), no. 4, 043904.

[128] V.V. Volkov, Y. Zhu, and M. De Graef, *A new symmetrized solution for phase retrieval using the transport of intensity equation*, Micron **33** (2002), no. 5, 411–416.

[129] Vyacheslav V. Volkov and Yimei Zhu, *Deterministic phase unwrapping in the presence of noise*, Optics Letters **28** (2003), no. 22, 2156.

[130] Xiaojun Wang, Xuli Fu, and D. D. L. Chung, *Strain sensing using carbon fiber*, Journal of Materials Research **14** (2011), no. 03, 790–802 (English).

[131] Wikipedia.Com, *Interferometry*, p. http://en.wikipedia.org/wiki/Interferometry.

[132] J. Wood, *Personal communication*, 2011.

[133] Marcus A. Worsley, Sergei O. Kucheyev, Joe H. Satcher, Alex V. Hamza, and Theodore F. Baumann, *Mechanically robust and electrically conductive carbon nanotube foams*, Applied Physics Letters **94** (2009), no. 7, 073115.

[134] Xiaojie Xue and Andreas A Polycarpou, *An improved meniscus surface model for contacting rough surfaces.*, Journal of colloid and interface science **311** (2007), no. 1, 203–11.

[135] Xiaojie Xue and Andreas A. Polycarpou, *Meniscus model for noncontacting and contacting sphere-on-flat surfaces including elastic-plastic deformation*, Journal of Applied Physics **103** (2008), no. 2, 023502.

[136] V. G. Yachmenev, D. V. Parikh, and T. A. Calamari, *Thermal Insulation Properties of Biodegradable, Cellulosic-Based Nonwoven Composites for Automotive Application*, Journal of Industrial Textiles **31** (2002), no. 4, 283–296.

[137] Kyunghwan Yoon, Benjamin S. Hsiao, and Benjamin Chu, *Functional nanofibers for environmental applications*, Journal of Materials Chemistry **18** (2008), no. 44, 5326 (en).

[138] W C Young, *Roark's Formulas for Stress and Strain*, 6th ed., McGraw Hill,, 1989.